X-RAY AND OPTICAL STUDIES OF INTERMEDIATE POLARS

MARK ANTONY GARLICK

Mullard Space Science Laboratory
Department of Physics and Astronomy
University College London

A thesis submitted to the University of London
for the degree of Doctor of Philosophy
September 1993

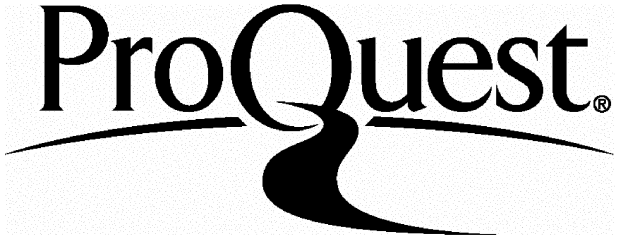

2

To Margaret Kate Harrop-Allin,
for her strength, her friendship and her love,
for her faith, her understanding and her trust,
for the pain and the suffering,
for the laughter and the smiles,
for the sentiments and for the memories,
I gladly dedicate this thesis.

Even though she laughed at my hat.

When you part from your friend, you grieve not;
For that which you love most in him may be clearer in his absence, as the mountain to the climber is clearer from the plain.

Kahlil Gibran
The Prophet (1923)

We are all in the gutter, but some of us are looking at the stars.

Oscar Wilde
Lady Windermere's Fan (1891)

ABSTRACT

Intermediate polars form a small (~ 12 members) subclass of the cataclysmic variables. The latter comprise a red dwarf secondary and a more massive accreting white dwarf, but in intermediate polars the white dwarf is deduced to have a magnetic field of strength $\gtrsim 1$ MG, from the pulsed emission which these stars exhibit. These systems are a relatively new discovery (less than two decades old), and therefore provide an active domain for current research.

The present work concerns the accretion geometry in intermediate polars, an area of considerable debate. After an introduction to the field (chapter 1), I present, in chapter 2, an analysis of the X-ray orbital modulations seen in *EXOSAT* timeseries from intermediate polars. These data have substantial implications for the accretion geometry in these systems.

The bulk of this thesis, however, is concerned with the systems BG Canis Minoris and GK Persei. Chapter 3 presents optical CCD photometry of BG CMi, and I refine the 913 s pulsational ephemeris using timings both new and previously published. In chapters 4 and 5, I present spin phase-resolved optical spectroscopy on these respective systems. A similar analysis of other systems has shown that this is a powerful method for probing the geometry and optical emission properties of the accretion flow in the vicinity of the white dwarf. This is of particular interest in BG CMi, where both the presence of an accretion disc and the spin period of the white dwarf are currently debated. In GK Per the existence of a disc is essentially incontestable, so the data presented in chapter 5 offer an excellent opportunity to investigate the curtain model which has been proposed to explain the spin modulation in intermediate polars. Finally, I detail, in an appendix, the various techniques

which I have employed for the reduction and analysis of the data contained in the previous chapters.

CONTENTS

FIGURES 15

TABLES 19

1. INTERMEDIATE POLARS: AN INTRODUCTORY REVIEW 21

1.1 Introduction: the cataclysmic variables 21

1.1.1 The standard model of a cataclysmic variable 22

1.2 Magnetic cataclysmic variables discovered 25

1.3 Polars: AM Herculis stars 27

1.4 Intermediate polars and DQ Herculis stars 27

1.4.1 The early systems: DQ Herculis stars 27

1.4.2 Long-period systems: intermediate polars 29

1.5 General properties of intermediate polars 31

1.5.1 X-ray emission 31

1.5.2 Optical spectroscopy 32

1.5.3 Discal or discless accretion? 33

1.5.4 Periodicities and their causes 34

1.5.4.1 Spin modulation 37

1.5.4.2 Beat modulation 40

1.5.4.3 Orbital modulation 43

2. X-RAY ORBITAL MODULATIONS IN INTERMEDIATE POLARS 45

2.1 Introduction 45

2.2 Observations 46

2.3 Data analysis 48

2.3.1 Orbitally related spin-cycle changes 48

2.3.2 Results from individual systems 52

2.3.2.1 TV Columbae (H0526−328) 52

2.3.2.2 TX Columbae (H 0542−407) 53

2.3.2.3 AO Piscium (H2252−035) 54

2.3.2.4 FO Aquarii (H2215−086) 56

2.3.2.5 BG Canis Minoris (3A 0729+103) 57

2.3.2.6 V1223 Sagittarii (4U 1849−31) 58

2.3.2.7 EX Hydrae 58

2.3.2.8 GK Persei (Nova Per 1901) 59

2.3.3 Summary of results 62

2.4 Discussion 62

2.4.1 Possible X-ray orbital modulation mechanisms 62

2.4.2 The quasi-periodicity in GK Persei 66

2.5 Summary of conclusions 69

3. SPIN-UP IN BG CANIS MINORIS: A CUBIC EPHEMERIS? 71

3.1 Introduction 71

3.2 Observations 72

3.2.1 Acquiring the data 72

3.2.2 Observing conditions 73

3.3 Data analysis 76

3.3.1 Magnitudes 76

3.3.2 Periodicities and their amplitudes 79

3.3.3 White dwarf rotation ephemerides 83
3.3.3.1 Pulse arrival times 84
3.3.3.2 Determining the errors on the arrival times 85
3.3.3.3 Ephemerides 90
3.3.3.4 Possible contaminations of the arrival times 91
3.4 Discussion 93
3.4.1 The amplitude of the 913 s modulation 93
3.4.2 Implications of the quadratic ephemeris 94
3.4.2.1 The accretion disc torque theory: a summary . . . 95
3.4.2.2 Expressions for the mass accretion rate 99
3.4.2.3 Primary mass and magnetic moment, and the accretion rate 101
3.4.3 Implications of the cubic ephemeris 103
3.5 Summary of conclusions 105

4. BG CANIS MINORIS: IS THE TRUE SPIN PERIOD 847 SECONDS? 107
4.1 Introduction 107
4.2 Observations 108
4.2.1 Acquiring the data 108
4.2.2 Observing conditions 109
4.3 Data analysis 111
4.3.1 Mean spectrum 111
4.3.2 Period-searching 113
4.3.3 The pulsational modulation 116
4.3.3.1 V/R ratio 116
4.3.3.2 Equivalent widths, line intensities, and continuum . 121
4.3.4 Orbital-cycle line variability 125
4.3.5 Summary of results 127

4.4 Discussion 129
4.4.1 Orbital effects 129
4.4.2 On the nature of the ∼1152 s period 131
4.4.3 Which is the true spin period? 131
4.4.3.1 A 913 s spin period? 131
4.4.3.2 A 1827 s spin period (twice 913 s)? 133
4.4.3.3 An 847 s spin period? 134
4.4.3.4 A 1693 s spin period (twice 847 s)? 136
4.5 Summary of conclusions 136

5. GK PERSEI: THE ACCRETION GEOMETRY 139
5.1 Introduction 139
5.2 Observations 141
5.3 Data analysis 142
5.3.1 Emission line spectrum 142
5.3.2 Secondary star spectrum 145
5.3.2.1 Spectral type 147
5.3.2.2 Luminosity class 149
5.3.3 The pulsational modulation 149
5.3.3.1 Equivalent width 150
5.3.3.2 Line intensities and continuum level 152
5.3.3.3 V/R ratio 154
5.3.4 Orbital-cycle line variability 160
5.3.5 Summary of results 161
5.4 Discussion 162
5.4.1 The line emission regions 162
5.4.1.1 The Balmer series and neutral helium lines 162
5.4.1.2 The He II λ4686 line 167

5.4.2 The inclination of GK Persei 167
5.4.3 The spin modulation 170
5.5 Summary of conclusions 172

APPENDIX: REDUCTION AND ANALYSIS 175

A.1 Introduction 175
A.2 General CCD reduction techniques 175
A.3 Photometry 177
A.3.1 Obtaining the count-rates 178
A.3.2 Atmospheric extinction 178
A.3.3 Magnitudes 179
A.3.4 Summary 180
A.4 Spectroscopy 181
A.4.1 Extracting the data 181
A.4.2 Wavelength calibration 182
A.4.3 Flux calibration 183
A.4.4 Removal of atmospheric absorption features 183
A.4.5 Calculating equivalent widths 184
A.4.6 Calculating V/R ratios 185
A.5 Reduction of X-ray temporal data 186
A.5.1 Medium energy 186
A.5.2 Low energy 187

REFERENCES 189

ACKNOWLEDGEMENTS 199

FIGURES

1. INTERMEDIATE POLARS: AN INTRODUCTORY REVIEW

1.1 Standard picture of a non-magnetic cataclysmic variable 23
1.2 Schematic representation of the 'front-back asymmetry' 37
1.3 Schematic representation of the accretion curtain scenario 39
1.4 Schematic representation of a discless accretion scenario 42

2. X-RAY ORBITAL MODULATIONS IN INTERMEDIATE POLARS

2.1 ME lightcurve orbital modulation of six intermediate polars 49
2.2 The spin-pulse profiles as a function of orbital phase 50
2.3 ME data, LE data, and hardness ratio of TV Col 52
2.4 ME data, LE data, and hardness ratio of TX Col 54
2.5 ME data, LE data, and hardness ratio of AO Psc 55
2.6 ME data and hardness ratio of FO Aqr 56
2.7 ME data, LE data, and hardness ratio of BG CMi 57
2.8 ME data, LE data, and hardness ratio of V1223 Sgr 58
2.9 ME and LE data of EX Hya folded on the orbital period 59
2.10 ME lightcurve of GK Per during outburst and quiescence 60
2.11 ME lightcurve and hardness ratio of GK Per during outburst 61
2.12 X-ray lightcurves of intermediate polars, LMXRBs, and dwarf novae 64

3. SPIN-UP IN BG CANIS MINORIS: A CUBIC EPHEMERIS?

3.1 Variation in seeing as a function of time 74
3.2 Raw lightcurves of BG CMi and a comparison star 75
3.3 Magnitude variation of BG CMi 78
3.4 Removing orbital trends from lightcurves 80
3.5 Fourier power spectra of BG CMi CCD photometry 81
3.6 The BG CMi photometry folded on the 913 s period 83
3.7 Best-fit quadratic and cubic ephemerides 93
3.8 The transition zones in a magnetically truncated accretion disc . . . 97
3.9 Relationships between $\dot{M}$ and M with $x_0 = 0.85 \pm 0.05$ 102

4. BG CANIS MINORIS: IS THE TRUE SPIN PERIOD 847 SECONDS?

4.1 Mean continuum variation in BG CMi 110
4.2 Mean Blue and red spectra of BG CMi 111
4.3 Comparing two period-searching routines 115
4.4 The average Balmer and He II λ4686 line profiles in BG CMi 116
4.5 Frequencygrams of the V/R ratio in the line wings of BG CMi . . . 118
4.6 Multiplying together the y-axes of the datasets in figure 4.5(a) . . . 119
4.7 BG CMi V/R ratio data folded on the possible spin periods 120
4.8 Frequencygrams of the line intensities and equivalent widths 122
4.9 Line intensity, equivalent width, and continuum frequencygrams . . 123
4.10 Line intensities and continuum flux folded at 1152 s 124
4.11 Intensity data folded on the candidate spin periods 125
4.12 Balmer line orbital variation in BG CMi 126
4.13 Balmer and He II λ4686 line orbital variation in BG CMi 128
4.14 Schematic showing a disc-fed accretion scenario for high i and m . . 134

5. GK PERSEI: THE ACCRETION GEOMETRY

5.1 The mean spectrum of GK Per 143
5.2 Absorption line radial velocity curve of GK Per 146
5.3 GK Per compared with standard G-star and K-star spectra 148
5.4 Fourier spectra of the Balmer lines' equivalent widths 151
5.5 Equivalent width, line intensities, and continuum folded on 351 s . . 152
5.6 Variations in the red continuum and the Hα line intensity 153
5.7 Fourier spectra of the V/R ratio in the Balmer lines of GK Per . . . 155
5.8 V/R ratio timeseries obtained from the Balmer lines of GK Per . . 156
5.9 The V/R ratio data folded on the spin period 157
5.10 Testing for the value of the period in the V/R ratio 159
5.11 Mean profiles of the blue Balmer lines on both nights 161
5.12 Model Balmer decrements 164
5.13 Views of GK Per at two inclinations and orbital phases 169

TABLES

1. INTERMEDIATE POLARS: AN INTRODUCTORY REVIEW

1.1 Periods in intermediate polars 35

2. X-RAY ORBITAL MODULATIONS IN INTERMEDIATE POLARS

2.1 *EXOSAT* observation log 47

2.2 Spin pulse-fractions for four intermediate polars 51

3. SPIN-UP IN BG CANIS MINORIS: A CUBIC EPHEMERIS?

3.1 Log of observations of standard stars and BG CMi 73

3.2 Comparison star magnitudes 77

3.3 Amplitudes of the 913 s modulation in BG CMi 84

3.4 Arrival times and cycle counts for the 913 pulsation 86

3.4 Continued 87

3.4 Continued 88

3.5 Best-fit BG CMi rotation ephemerides 92

4. BG CANIS MINORIS: IS THE TRUE SPIN PERIOD 847 SECONDS?

4.1 BG CMi spectroscopy observing details 109

4.2 Emission line strengths and equivalent widths in BG CMi 112

5. GK PERSEI: THE ACCRETION GEOMETRY

5.1 GK Per spectroscopy observing details 142
5.2 Emission line strengths in GK Per, relative to Hβ 144
5.3 Secondary star absorption line velocities in GK Per 146

1. INTERMEDIATE POLARS: AN INTRODUCTORY REVIEW

It seems a bit daft to ask me to write an introduction to this book, because basically it needs no introduction. So, let us go onto something else. It's a nice day today except that I hit my knee against the corner of a flower pot, which caused a slight abrasion to the skin, about, I would say, a quarter of an inch from the Patella.

Spike Milligan
The Goon Show Scripts (1972)

1.1 INTRODUCTION: THE CATACLYSMIC VARIABLES

In 1954, Walker discovered an optical eclipse in the classical nova DQ Her (Nova Her 1934), a star which we now know belongs to a subclass of the objects collectively referred to as cataclysmic variables. The term 'cataclysmic variable' derives from the eruptive behaviour of these objects—the so-called 'outbursts' which are observed from time to time. Walker's comment that *all* novae might be binary systems was extremely precocious, for now it is probably correct to say that all cataclysmic variables are indeed binary in nature, and that binarity is a necessary requirement for the outburst phenomenon.

By definition, a classical (or old) nova such as DQ Her is one which has shown only one outburst, with an amplitude of up to ~ 20 mag. Further categorisation of cataclysmic variables has been introduced over the years, and there now exist four additional major subclasses: the recurrent novae, which exhibit irregular but

repeated outbursts with an amplitude of ~ 4–9 mag and recurrence timescale on the order of decades; the dwarf novae, which also display recurrent outbursts, but with an outburst amplitude that is less than in the former systems (~ 5 mag) and with a smaller recurrence timescale ($\sim$ weeks or months); nova-like objects, which have the spectral signatures of novae, but for which no actual outbursts have ever been recorded; and the magnetic systems (i.e., where the primary star has a magnetic field $\gtrsim 1$ MG), which are a relatively new discovery (less than two decades old). The magnetic systems are further subdivided into two categories: the polars and the intermediate polars[1]. The latter systems are the subject of this thesis.

In this introduction, I give an overview of the magnetic cataclysmic variables, primarily intermediate polars. I concentrate on their history, their observational characteristics, and the physical interpretations thereof. I will also discuss briefly the polars (see §1.3), mainly to emphasise the physical differences between these two types of system. Prior to the discussion of the magnetic subclasses, however, I give a brief account of what has come to be recognised as the standard picture of a general cataclysmic variable (reviewed by Livio 1993, and Córdova 1993).

1.1.1 THE STANDARD MODEL OF A CATACLYSMIC VARIABLE

The original model for cataclysmic variables was proposed by Crawford & Kraft (1956), prompted by the discovery (Joy 1954) that AE Aqr was a binary system. Their overall picture still remains essentially valid. The systems are now known to comprise a white dwarf (the primary) and a late-type star usually near the Main Sequence (the secondary). The white dwarf is generally the more massive component. Owing to the proximity of the two stars (on the order of a Solar radius, deduced from orbital periods on the timescale of hours), the secondary is tidally distorted (refer to figure 1.1). Consider a coordinate system originating at the center of mass of the pair of stars and rotating with the binary motion. In this frame,

[1]Some authors argue that intermediate polars are distinct from the DQ Her stars (see §1.4.1), with the AM Her stars making *three* magnetic subclasses in total. For reasons which I discuss in §1.4.2, I treat intermediate polars and DQ Her stars as being *in*distinct in this thesis.

close to the centre of each star, away from the influences of their companions, the combined gravitational/centrifugal potentials are spherical. Further out, however, the potentials become elongated, until, for a critical value of the potential, those surrounding each star meet at the inner Lagrangian point (L_1), where the net force is zero. The 'surface' defined by this potential is known as the critical Roche surface, and the regions it encloses are called the Roche lobes. The relative sizes of the lobes depends solely on the ratio of the stars' masses, with the most massive star having a more extensive Roche surface. The scale of the system is determined purely by the separation of the two stars.

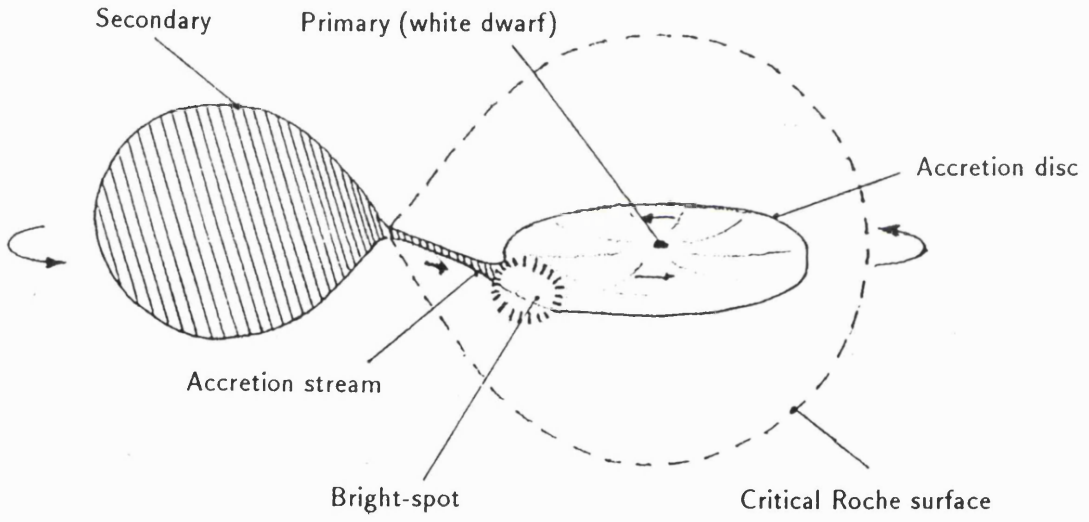

FIGURE 1.1: *Standard picture of a non-magnetic cataclysmic variable.*

The geometry of the secondary is non-spherical and is governed by the critical Roche surface, the importance of which was first discussed by Kuiper (1941). When the secondary just fits inside (i.e., 'fills') its Roche lobe, the gas at the L_1 point overflows into the primary Roche lobe. It has been known for some time that conservation of mass and of angular momentum during this transfer of material cannot occur, as this would cause the secondary to disconnect from its Roche lobe and would eventually halt the mass transfer process (Patterson 1984). For the

secondary to maintain Roche lobe contact and continue to drive the mass transfer, one of two criteria must therefore be satisfied: either it must expand on an evolutionary timescale as its mass is depleted, or the Roche lobe itself must contract. It is now well established that the secondaries in many, if not all, cataclysmic variables with orbital periods less than $\sim 9\,\mathrm{hr}$ (i.e., most systems) are not in a state of evolutionary expansion (e.g., Patterson 1984). Therefore, it follows from the above argument that the Roche lobe radii of such stars must be decreasing and that some process must be responsible for extracting orbital angular momentum from these systems.

The angular momentum-loss mechanisms which have been suggested are the emission of gravitational radiation for systems with periods less than $\sim 3\,\mathrm{hr}$, and magnetic stellar-wind braking for the longer period systems (see Lamb & Melia 1987). In the latter scenario, the secondary is assumed to possess a sizeable stellar wind and magnetic field (300–1000 G, Lamb & Melia 1987). Material is carried outwards in the stellar wind along magnetic field lines, braking the rotation of the secondary and therefore, because of tidal coupling between the secondary's rotation and the binary orbit, reducing the orbital period. The separation of the two stars, and thus the radii of the Roche lobes, also reduces. This has the effect of 'peeling' the secondary star, and leads to a sustained ejection of material at L_1.

In a non-magnetic system (i.e., where the white dwarf does not possess a strong magnetic field), once the accretion stream from L_1 enters the primary Roche lobe an accretion disc is formed. The formation of the disc is essentially promoted because the material leaving L_1 has such a large angular momentum that it is unable to accrete directly onto the surface of the degenerate primary. Inside the primary Roche lobe (initially containing only the white dwarf) the overflowing gas is expected to form a stream which orbits the compact star elliptically before interacting with itself. In this interaction kinetic energy is dissipated by the gas with the result that the orbit of the gas becomes smaller, more circular, and an accretion ring is formed. This ring will tend to form at a Kepler radius (R_{circ}) such

that its specific angular momentum is similar to that of the gas at L_1. Continued dissipation in the ring via processes such as collisions and viscous interactions leads to radiative losses, accompanied by a redistribution of angular momentum. The orbiting material spirals inwards, and angular momentum is transferred to the outer regions of the ring causing them to expand outwards, forming a fully fledged disc. The outer dimension of the disc is determined by tidal interaction with the secondary and/or by the influence of the impacting accretion stream.

Where the accretion stream from L_1 is incident on the disc, a region of enhanced emission ('bright-spot') is believed to exist. The varying aspect of this region may manifest itself in photometry as a quasi-sinusoidal modulation, or in spectroscopy as an 'S-wave' in trailed spectra (see §1.5.4.3).

If the white dwarf *does* possess a strong magnetic field, or at least has a magnetosphere which has a radius larger than R_{circ}, the magnetosphere presents an obstacle to the stream leaving L_1 and inhibits the formation of an accretion disc. Such conditions are thought to exist in some magnetic systems (see §1.3 and §1.5.3).

1.2 Magnetic cataclysmic variables discovered

A clue that some cataclysmic variables might contain magnetic white dwarfs has been available since at least 1956, when Walker discovered a 71 s modulation of amplitude 0.05 mag in optical photometry of DQ Her. It was finally suggested, two decades after Walker's discovery, that these pulses might be attributed to a magnetic 'oblique rotator' in the system (Lamb 1974; Herbst, Hesser & Ostriker 1974; Bath, Evans & Pringle 1974). In this model, the white dwarf is assumed to possess a strong (dipole) magnetic field which is inclined with respect to its spin axis. Material accreted by the primary is channelled along field lines and strikes the star at the magnetic poles, producing 'bright-spots' where the kinetic energy of the infalling gas is liberated. The varying aspect of these regions of enhanced brightness as the star spins produces the observed lightcurve modulation.

The oblique rotator model acquired swift recognition when spin-modulated cir-

cular and linear polarisation was discovered at optical wavelengths in DQ Her (Swedlund, Kemp & Wolstencroft 1974; Kemp, Swedlund & Wolstencroft 1974). The peak-to-peak amplitudes of the polarisations were recorded as 0.2% (linear) and 0.6% (circular), and Swedlund, Kemp & Wolstencroft attributed the 'broad-band circular polarisation ... to a magnetic field with a longitudinal component of at least $\sim 10^6$ G'. This was the first suggestion of a magnetic field in a cataclysmic variable.

Then, c. 1976–1977, attention began to centre around the nova-like variable AM Her when it was suggested that this system was the optical counterpart of the high-galactic latitude X-ray source 3U1809+50 (Berg & Duthie 1977; see also Hearn, Richardson & Clark 1976). A deluge of optical spectroscopic and photometric observations of this system followed (e.g., Szkody & Brownlee 1977, Priedhorsky 1977, and Cowley & Crampton 1977), culminating in the discovery of periodic linear and circular optical polarisation at peak-to-peak levels of $\sim 6\%$ and $\sim 13\%$ respectively (Tapia 1977; Stockman et al. 1977). Such a high degree of polarisation in astrophysical objects was unheard of at the time, and was attributed to cyclotron radiation from material being funnelled along field lines onto the pole(s) of a white dwarf. The strength of the polarisation implied that the surface magnetic field of the primary in AM Her was $\sim 10^8$ G, but this was an overestimate (see §1.3). Nowadays, it is recognised that some 20% of cataclysmic binaries are magnetic to some degree (Ritter 1990).

The discovery of a white dwarf magnetic field in AM Her and, possibly, DQ Her implied that a new subclass was needed for the cataclysmic variables. However, these two stars are not quite the same kind of system. In fact, with further discoveries of magnetic cataclysmic variables, AM Her and DQ Her became established as the prototypes of *two* subclasses of cataclysmic variable—called polars and intermediate polars respectively—each with substantially different physical and observational characteristics.

1.3 Polars: AM Herculis stars

Further systems showing characteristics similar to those of AM Her were discovered shortly after the prototype was revealed. Krzemiński & Serkowski (1977) reported strong optical circular polarisation (-9% to -35%) in the nova-like variable AN UMa, and they suggested, based on this distinct signature, that these objects be known thereafter as 'polars'—a name which has persisted (see also Krzemiński 1977 and references therein).

The original model for AM Her was put forward by Stockman et al. (1977) and remains accepted for all polars to this day. It is understood that the white dwarf's magnetic field in these systems is so strong (tens of MG) that, combined with a short orbital period (usually less than 2 hr), it is able to lock the primary into synchronous rotation. In other words, the white dwarf's spin period is equal to the binary period, so the system effectively rotates as a rigid body. No accretion disc is able to form because the primary's magnetosphere is so large that gas leaving the L_1 point interacts with it before it is able to circularise as discussed in §1.1.1.

The strong phase-dependent circular and linear optical polarisation and cyclotron emission in polars is one of the main features that distinguishes them from intermediate polars (see §1.4). The other main difference between these two types of system—owing to synchronous rotation in polars—is that AM Her stars do not show pulsations, such as those exhibited by DQ Her. Polars are further distinguished from intermediate polars in having an ultra-soft X-ray spectral component, and a stronger He II λ 4686 emission line. A fully comprehensive review on polars is given by Cropper (1990).

1.4 Intermediate polars and DQ Herculis stars

1.4.1 The early systems: DQ Herculis stars

After 25 years of fruitless searching by various investigators for stars having characteristics similar to those of DQ Her, such a star was finally discovered. Pat-

terson (1978, 1979a) announced the presence of 'rapid coherent oscillations in the lightcurve of the remnant of Nova Herculis 1963 (=V533 Her)'. In terms of the morphology of the oscillations, their periods, and their rates of change, DQ Her and V533 Her appeared to be very similar systems. Further similarities were that neither star had been detected significantly in X-rays (Córdova, Mason & Nelson 1981), and that both were old novae. Based on these factors, V533 Her was classified as a member of a new subclass of systems which were dubbed 'DQ Her stars'. In retrospect, however, it is somewhat ironic that V533 Her was classified as the second DQ Her star because its oscillations have since ceased (Robinson & Nather 1983), and its membership in this class is now doubtful.

A further suspected member of the DQ Her subclass was AE Aqr. Renewed interest in this nova-like variable was sparked, after a ~ 20 year absence from the literature, when Patterson (1979b) reported that this system, like those discussed above, exhibited a strictly periodic pulsation with a period of 33 s in its optical lightcurve. However, AE Aqr differs from DQ Her and V533 Her in at least one important respect, namely that it was detected as an X-ray source (*Einstein*, Patterson et al. 1980). This was therefore one of the first DQ Her stars to show a measurable X-ray flux (but see §1.4.2). Moreover, the 33 s pulsations which had been seen in optical photometry were also observed in X-rays, in phase with the optical modulation. Based on the observed upper-limits on the period change, AE Aqr was deduced to contain a white dwarf rather than a neutron star (Patterson et al. 1980), and was thus the first known white dwarf X-ray pulsar (all X-ray pulsars known up until that time comprised of neutron stars).

By the end of the seventies, basic ideas concerning the workings of this class of object had been investigated by various authors. Early attempts to explain the pulsed emission (e.g., radial pulsations: Walker 1958, and Kraft 1963) had been discarded. It ~~become~~ became generally recognised that the DQ Her stars contain a rapidly rotating magnetic white dwarf, as in the oblique rotator model, which is surrounded by an accretion disc (the presence of discs in both DQ Her and AE Aqr

had been fully established by this time). It was also realised that the disc would be disrupted at some distance from the degenerate dwarf which depended critically on its magnetospheric radius and the mass accretion rate. Surface fields in the range 10^6–10^8 G were predicted, for example, from the lack of circular polarisation in the optical continuum (AE Aqr, Patterson 1979b). However, although rotation of the white dwarf had been established as the basic clock which produced the pulsations in these systems, what had not been settled was the actual mechanism which was responsible for the observed modulation. For example, Lamb (1974) suggested that the modulation was generated by the varying aspect of a bright-spot on the surface of the white dwarf (as in Bath, Evans & Pringle 1974), but the oscillations in AE Aqr were attributed to reprocessing of radiation from the white dwarf at the inner edge of the accretion disc. More recent models for the pulsational modulations will be discussed in §1.5.4.1 and §1.5.4.2.

1.4.2 Long-period systems: intermediate polars

With the advent of better X-ray observatories, more X-ray-emitting systems with possibly asynchronously rotating magnetic white dwarfs began to emerge. The first was H2252−035, identified as the X-ray counterpart to the 13th magnitude cataclysmic variable AO Psc (*Ariel V*, Griffiths et al. 1980). Further X-ray observations of AO Psc (Patterson & Garcia 1980; White & Marshall 1980, 1981) revealed the presence of a pulsation at a period of 805.2 s. Optical observations of this star (e.g., five colour photometry—Motch & Pakull 1981; spectroscopy and photometry—Patterson & Price 1981, and Warner, O'Donoghue & Fairall 1981) showed this period also, but in addition contained a stronger variation at a period of 858.6 s. Later X-ray observations of AO Psc using the *EXOSAT* medium-energy (ME) experiment confirmed the presence of the 805.2 s period (Pietsch et al. 1984, 1987). These periods are an order of magnitude longer than in DQ Her, V533 Her, and AE Aqr. Furthermore, *EXOSAT* ME observations of TV Col, another X-ray emitting cataclysmic variable (*Ariel V*, Charles et al. 1979; *HEAO-1*, Schwarz et

al. 1979; Watts et al. 1982), revealed the presence of a 1943 s period (Schrijver et al. 1985), which was later refined to 1911 s (Schrijver, Brinkman & van der Woerd 1987). Again, these pulsation periods are an order of magnitude longer than in the earlier discovered systems.

With further discoveries of pulsating X-ray sources (4U 1849−31 = V1223 Sgr [Steiner et al. 1981]; 3A 0729+103 = BG CMi [McHardy et al. 1982, 1984]; H2215 −086 = FO Aqr [Patterson & Steiner 1983]) it was becoming apparent by 1983 that these new pulsating stars might actually belong to a subclass of magnetic objects distinct from the DQ Her stars, making three magnetic subclasses in total. The reasons for this are at least threefold: (a) the spin periods in the asynchronously rotating magnetic systems DQ Her, V533 Her, and AE Aqr (short-period systems) are an order of magnitude shorter than in more recently discovered objects such as TV Col and AO Psc (long-period systems); (b) only one of the short-period systems discovered showed X-ray emission (AE Aqr), whereas all long-period systems were seen in X-rays (indeed, they were often discovered *by virtue* of their X-ray emissions); (c) the long-period X-ray pulsars frequently contained more than the one pulsation seen in the shorter period DQ Her stars (see §1.5.4).

The new long-period systems were named 'intermediate polars' (Warner 1983). However, this has always been somewhat of a misnomer because none of the long-period systems *known at the time* had been reported to show polarisation. Even today, only two do: BG CMi (e.g., Penning, Schmidt & Liebert 1986, West, Berriman & Schmidt 1987) and RE0751+14 (Rosen, Mittaz & Hakala 1993).

The question of whether the DQ Her stars and intermediate polars are distinct remains subjective, but a few points concerning the above reasons (a) and (b) for believing in this distinction are worthy of note. Firstly, reason (a) is less important now with the discovery of the eclipsing intermediate polar H0253+193 (Kamata, Tawara & Koyama 1991), which shows a strong X-ray period of 206 s, more comparable to the short-period systems than are the periods of other intermediate polars. Secondly, reason (b) can no longer be considered important because, with the pos-

sible misclassification of V533 Her, only two DQ Her objects exist—the prototype itself and AE Aqr—and AE Aqr *is* an X-ray source (although the X-ray temperature is lower in AE Aqr than in the long-period systems; Osborne 1990; see §1.5.1). Moreover, DQ Her has the highest inclination amongst all the asynchronously rotating magnetic systems, being viewed essentially edge-on (90°, Ritter 1990 and references therein). Thus, it may be possible that this *is* an X-ray source, but that the accreting white dwarf is permanently obscured by a concave disc.

Throughout this work, I will therefore use the term 'intermediate polar' to describe *all* systems containing asynchronously rotating magnetic white dwarfs, irrespective of their spin periods. However, I do not necessarily claim that the long-period and short-period classes are one and the same.

1.5 General properties of intermediate polars

1.5.1 X-ray emission

Frank, King & Raine (1992) show that for typical electron densities ($10^{16}\,\mathrm{cm}^{-3}$) and magnetic field strengths ($10^{7}\,\mathrm{G}$) in the vicinity of the matter falling onto a white dwarf, the electrons and ions will be strongly directed along the field lines towards the polar caps in roughly a radial direction. The resulting structure is referred to as an 'accretion column'. Obviously, therefore, the material must be decelerated when it approaches the surface of the white dwarf. It is in this deceleration process that the kinetic energy of the infalling gas is dissipated and radiated away as high-energy electromagnetic radiation. If the accretion rate is sufficiently high, the accreting material will penetrate the photosphere and the resultant radiation will be optically thick blackbody emission with a characteristic temperature $T \sim 10^{5}\,\mathrm{K}$. However, observations point to a much higher X-ray temperature than this ($T \sim 10^{8}\,\mathrm{K}$, see Watson 1986 and Osborne 1988), suggesting that the majority of the emission is from a strong shock *above* the photosphere of the white dwarf. The post-shock gas cools via optically thin free-free (bremsstrahlung) interactions, emitting radiation in the form of hard ($\gtrsim 2\,\mathrm{keV}$) X-rays.

Soft X-rays ($\lesssim 0.1\,\mathrm{keV}$) might also be expected if a fraction of the hard X-rays are absorbed by the white dwarf and re-emitted as optically thick blackbody radiation ($T \sim 10^5\,\mathrm{K}$), as is often seen in polars. However, intense soft X-rays are not usually observed in intermediate polars. King & Lasota (1990) have shown that this is consistent with high accretion rates ($\dot{M} > 10^{17}\,\mathrm{gs}^{-1}$), large accretion polecaps (fractional area $f \gtrsim 0.1$), and a white dwarf mass $M \lesssim 0.6$–$1.0\,M_\odot$, as the effective blackbody temperature of the reprocessed emission is $T_{eff} \propto (M\dot{M}f^{-1}R^{-3})^{1/4}$. A large value of f is intuitively expected in intermediate polars because the white dwarf is in a state of rotation relative to the binary frame so that material accretes onto its surface in a wide range in latitude. Furthermore, Canalle & Opher (1991) have demonstrated that large inhomogeneous polecaps (and 5–25 MG fields) are in agreement with the lack of polarisation in intermediate polars. However, the size of the polecaps in these systems remains unsettled (see §1.5.4.1 and §1.5.4.2). An alternative explanation for the lack of soft X-rays is that, because intermediate polars all have high intrinsic column densities ($N_H \sim 10^{23}\,\mathrm{cm}^{-2}$, King & Lasota 1990) and show photoelectric absorption, the low-energy component might be completely absorbed.

1.5.2 OPTICAL SPECTROSCOPY

The optical spectra of intermediate polars have blue continua upon which are superimposed strong emission lines of the hydrogen Balmer series, and of neutral and singly ionised helium. Typical spectra from the intermediate polars BG CMi and GK Per are shown in chapters 4 and 5 (figures 4.2 and 5.1) respectively. Often, the optical continuum over the wavelength range $\lambda\lambda\,4500$–5000 may be described by a power law of the form $F_\nu \propto \nu^\alpha$, with α typically between +0.3 and +0.4 (e.g., +0.33 in AO Psc [Griffiths et al. 1980], +0.4 in V1223 Sgr [Steiner et al. 1981], and +0.4 in BG CMi [McHardy et al. 1987; see also chapter 4]). These numbers are in good agreement with the value $\alpha \simeq +0.3$ expected for a continuum formed in an optically thick accretion disc (Pringle & Rees 1972).

The Balmer lines often show an inverted decrement, with Hβ or Hγ being the strongest of the series (e.g., see §5.4.1.1). The low order lines at least are therefore inferred to be optically thick because the inverted decrement is not consistent with the pattern expected if the lines are produced via recombination in an optically thin gas (see Brocklehurst 1971). In the latter case, Hα is expected to be the strongest line, with lower order lines weakening in comparison down the sequence, [as fewer electrons will be excited to the higher energy levels than to the lower ones] Williams (1980) has suggested that in cataclysmic variables with discs, optically thick H I lines may be produced in the outer regions where the discs are optically thin in the continuum. Furthermore, Williams suggests that He II λ 4686 is likely to be emitted in a more localised region, such as a disc bright-spot. However, in intermediate polars the H I lines and He II λ 4686 frequently show spin modulation in radial velocity and intensity. Therefore, although the majority of the line emission may indeed arise in the outer regions of a disc (if present—this is still an unresolved question in these systems: see §1.5.3), an additional emission region must exist in a magnetically controlled accretion flow (see §1.5.4.1).

1.5.3 Discal or discless accretion?

One of the greatest points of debate concerning intermediate polars is whether or not these systems contain accretion discs. The short-period intermediate polars, DQ Her and AE Aqr, were well studied and had been known for some time to contain discs, and it was therefore implicitly assumed that the newly discovered, longer period systems did also. By the mid-eighties, however, with more and more polars being discovered with strong fields (tens of MG), the notion was entertained that perhaps the magnetic fields in polars and intermediate polars had comparable strengths. Hameury, King & Lasota (1986) drew attention to the fact that if the magnetosphere of the primary is greater than the natural circularisation radius of the gas which leaves the L_1 point, then an accretion disc will not be able to form. In this situation, the gas impacts directly onto the magnetosphere and is possibly

thereafter magnetically channelled, as is thought to occur in polars.

Observational and theoretical arguments pertinent to the discal/discless debate have been presented by Hellier (1991, 1992a, 1992b) and by King, Mouchet & Lasota (1991). To summarise these works, a large body of observations point to the presence of a disc in many systems (e.g., spectroscopic eclipse observations, §1.5.4.3; spin modulation, §1.5.4.1), whilst theoretical arguments suggest otherwise (e.g., magnetic moments and evolution, see King, Frank & Ritter 1985, Lamb & Melia 1987, Hameury, King & Lasota 1986, and Hameury et al. 1988). A compromise is that a 'non-accretion disc' might be present (e.g., King, Mouchet & Lasota 1991, and King & Lasota 1991). In this situation, a truncated disc or ring exists, but the accretion flow from L_1 skips over the surface of the disc or ring to impinge directly onto the white dwarf magnetosphere. Thereafter, the flow either becomes channelled along the field lines, or it breaks up and continues in the form of 'blobs' on ballistic trajectories down to the surface of the white dwarf (e.g., McHardy et al. 1987). A non-accretion disc would be observationally similar to an *accretion* disc, but the accretion flow is not carried through the disc at all, so the system exhibits characteristics of both geometries. A gas streams which overflows a disc has been suggested for the dwarf nova Z Cha (Lubow 1989).

This debate is unlikely to be resolved without detailed multi-wavelength analyses of all intermediate polars. I return to this problem in chapters 2 and 4.

1.5.4 PERIODICITIES AND THEIR CAUSES

The X-ray and optical photometric periodicities of currently *confirmed* members of the intermediate polars are summarised in table 1.1. Further members have been suggested, but their status as intermediate polars remains uncertain due to lack of firm detections of the pulsation periods; in most of these cases the pulsations are not independently determined. Examples include YY Dra (Patterson et al. 1992; Mateo, Szkody & Garnavich 1991), KO Vel (Chiappetti et al. 1989b; Kubiak & Krzemiński 1989; Mukai & Corbet 1991; Sambruna et al. 1992), H0538−581

Source name	P_{orb}	Pulse periods		Refs
	(hr)	X-ray (s)	Opt. phot. (s)	
GK Per	47.92	351.34	none	1, 2
AE Aqr	9.88	33.08, 33.11	33.08	3, 4
RE0751+14	~ 6?	833.72	833.72, ~ 912	5, 6
H0253+193	6.06	206.30	?	7, 8
TX Col / H0542−407	5.72	~ 1910, ~ 2110	~ 2110	9
TV Col / H0526−328	5.49	~ 1911	none	10, 11
FO Aqr / H2215−086	4.85	1254.45, 1351.57	1254.45, 1351.57	12, 13
DQ Her	4.65	Not an X-ray source	71.07	14
AO Psc / H2252−035	3.59	805.20	805.20, 858.69	15, 16
V1223 Sgr / 4U 1849−31	3.37	745.50	794.38	17, 18, 19
BG CMi / 3A 0729+103	3.23	847.03, 913.48	913.48	20, 21
EX Hya	1.64	4021.62	4021.62	22

References for this table:

[1] Crampton, Cowley & Fisher (1986); [2] Ishida et al. (1992); [3] De Jager (1991); [4] Patterson (1979b); [5] Rosen, Mittaz & Hakala (1993); [6] Mason et al. (1992); [7] Patterson & Halpern (1990); [8] Kamata, Tawara & Koyama (1991); [9] Buckley & Tuohy (1989); [10] Schrijver et al. (1985); [11] Barrett, O'Donoghue & Warner (1988); [12] Osborne & Mukai (1989); [13] Norton et al. (1992a); [14] Patterson, Robinson & Nather (1978); [15] Kaluzny & Semeniuk (1988); [16] Pietsch et al. (1987); [17] van Amerongen, Augusteijn & van Paradijs (1987); [18] Jablonski & Steiner (1987); [19] Osborne et al. (1985); [20] Norton et al. (1992b); [21] Patterson & Thomas (1993); [22] Jablonski & Busko (1985).

TABLE 1.1: *Periods in intermediate polars.*

(Buckley & Tuohy 1990), 1H0709−360 (Tuohy et al. 1990), V795 Her (Ashoka et al. 1990; Shafter et al. 1990; Zhang et al. 1991), and SW UMa (Shafter, Szkody & Thorstensen 1986).

Table 1.1 shows that all intermediate polars except EX Hya have orbital periods greater than 3 hr. However, the majority of polars have orbital periods less than 2 hr. Interestingly, therefore, polars and intermediate polars in general lie respectively below and above the so-called 'period gap'—the name given in recognition of the deficiency of cataclysmic variables having orbital periods in the range $\sim$2–3 hr. This has led some authors to believe that polars are intermediate polars in a later stage of evolution (see King, Frank & Ritter 1985, Lamb & Melia 1987, and Hameury et al. 1988).

In general, intermediate polars are multiply periodic, with one system (TV Col, Hellier, Mason & Mittaz 1991) showing as many as four periods between X-ray and optical energies. The more usual number of periods, however, is three, exhibited by seven out of twelve systems. In fact, this three-period pattern is often described as the signature of an intermediate polar, though not all members conform to this picture. These three principle periods are generally attributed to the orbital motion, the spin period (rotation period of the white dwarf ~~period~~ in the observer's frame), and the beat period (rotation period in the binary frame). The latter two periods are those referred to as the 'pulse periods' in table 1.1. Additional beat periods are occasionally seen (e.g., as seen in TX Col; Buckley & Sullivan 1992), but these are not indicated in table 1.1. In all cases bar one[2] where two pulses are seen, the shortest period is believed to represent the spin of the white dwarf, and is the one most readily detected in X-rays. Beat-period modulations are also occasionally seen in X-rays (e.g., TX Col [Buckley & Tuohy 1989] and BG CMi [Norton et al. 1992b, hereafter NMLW]), but are more commonly manifested in the optical band, sometimes at a higher amplitude than the optical spin-pulse.

[2]In BG CMi, it is currently uncertain which of the two X-ray periods is the spin period (see chapter 4).

1.5.4.1 Spin modulation

The earliest attempts to explain the pulsational emission in AE Aqr and DQ Her have since been modified, and now quite elaborate spin modulation mechanisms have been proposed.

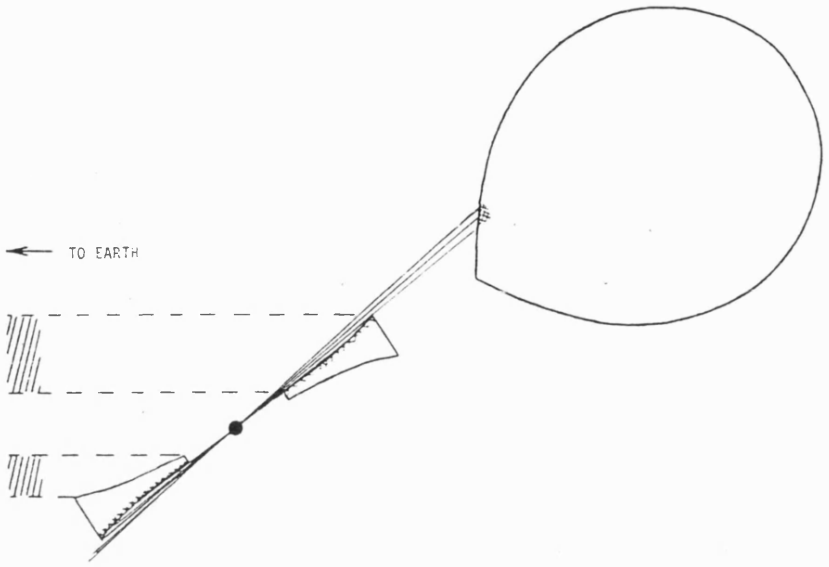

FIGURE 1.2: *Schematic representation of the 'front-back asymmetry' perhaps expected in a system with a disc (adapted from Penning 1985). See the explanation in §1.5.4.1.*

King & Shaviv (1984, hereafter KS) proposed that the hard ($\gtrsim 3\,\mathrm{keV}$) X-ray lightcurves of accreting magnetic white dwarfs could be explained as 'due solely to occultations of the emission region by the white-dwarf body'. Shortly thereafter, Penning (1985) and Warner (1985) investigated a model in which the *optical* spin modulation was generated. This was referred to by Penning as the 'rotation illumination model'. In this model, an X-ray beam from the white dwarf sweeps around at the spin period and is reprocessed into optical radiation in axisymmetric regions of a concave accretion disc. The disc is inclined and therefore presents a 'front-back asymmetry' (see figure 1.2)—the parts of the disc furthest from the observer present a larger surface area projected perpendicularly to the line-of-sight than do the nearer regions of the disc. Therefore, optical maximum is observed

with the upper magnetic pole pointing away from the observer, coincident with X-ray minimum. When the nearest regions of the disc are illuminated, minima in optical and maxima in X-rays are expected. Furthermore, as the velocity of the material in an illuminated region at any given time approximately reflects the (supposedly) Keplerian disc motion, the reprocessed optical radiation will exhibit a radial velocity modulation at the spin period.

Penning's (1985) representation has now been essentially abandoned by many authors, with the advent of spin phase-resolved optical spectroscopy. The reasons are manyfold. For example, maximum blueshift in the emission lines is expected in Penning's model when the left side of the disc (relative to the observer) is illuminated. This phase follows a quarter of a spin cycle after the expected phase of maximum optical intensity, but observations show that maximum blueshifted emission generally occurs at maximum photometric pulse intensity (see Hellier et al. 1987, Hellier, Mason & Cropper 1990, and Hellier, Cropper & Mason 1991). Furthermore, the X-ray and optical pulses are usually in phase—in clear contradiction to Penning's model.

An advance in the understanding of the spin-pulsation was achieved when *EXOSAT* observations clearly demonstrated that aspects of the X-ray spin modulation are energy dependent (e.g., Norton & Watson 1989). Larger modulation depths are observed at the lowest energies, a dependence which suggests that spin phase-varying photoelectric absorption plays a significant rôle in the modulation. Phase-varying photoelectric absorption had not been seen from intermediate polars when KS proposed their occultation model. Norton & Watson showed that the KS model by itself was inappropriate, and that a combination of occultation and phase-varying photoelectric absorption was needed.

Probably the most successful model for the spin modulation which takes into account the effects of photoelectric absorption in intermediate polars is the so-called 'accretion curtain' scenario. This was originally proposed by Rosen, Mason & Córdova (1988, hereafter RMC) to explain the X-ray spin modulation in EX Hya.

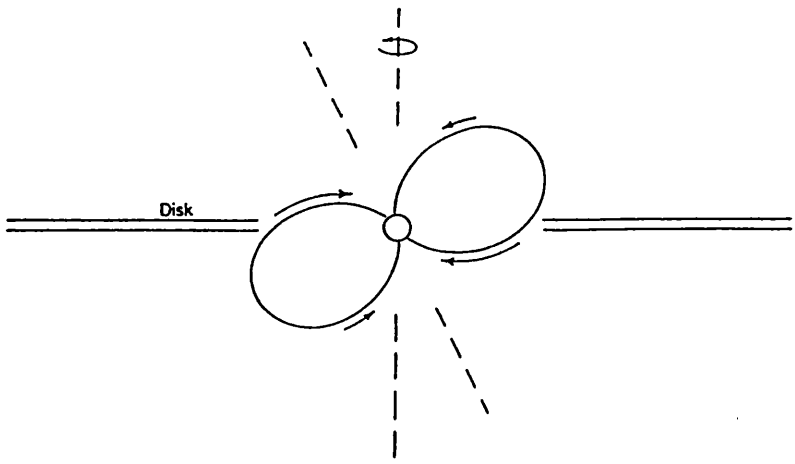

FIGURE 1.3: *Schematic representation of the accretion curtain scenario in an intermediate polar (adapted from Hellier et al. 1987). When viewing from the left, the upper pole, preferentially accreting, is observed through a large optical depth, and a minimum X-ray flux is observed. When viewing from the right, a minimum optical depth is encountered, and a maximum X-ray flux seen.*

The main requirement of the accretion curtain model, schematised in figure 1.3, is an accretion disc which is truncated by the magnetic field in the vicinity of the Alfvén radius, where the energy density of the magnetic field is comparable to that in the accreting plasma. The magnetic field is assumed to be dipolar. Material accretes onto both poles, preferentially along the shortest field lines, forming diametrically opposed, optically thick 'curtains'. X-ray emission arises from the bremsstrahlung process in the stand-off shock at the base of the curtain. When viewing from the left above the disc in figure 1.3, the upper pole is observed through a large optical depth, and a minimum X-ray flux is seen. When viewing from the right, a minimum optical depth to the upper pole is encountered, and a maximum X-ray flux observed. It is also possible for the lower pole to contribute to the modulation provided it is visible. This has been suggested for EX Hya (Hellier et al. 1987; Beuermann & Osborne 1988; Rosen et al. 1991).

Results of subsequent spectroscopic observations of EX Hya (Hellier et al. 1987) and other systems (FO Aqr [Hellier, Mason & Cropper 1990] and AO Psc [Hellier,

Cropper & Mason 1991]) were found to be consistent with the behaviour expected according to RMC's model. For example, if the optical line/photometric emission arises in the curtain as well, maximum blueshift and maximum X-ray/optical spin intensity will coincide in phase, as is indeed observed in the three systems mentioned here. This emphasises a fundamental difference between the models of RMC and KS: maximum X-ray intensity is seen when the accreting pole points *away* from the observer in the RMC case, and *towards* the observer in the KS model. Another difference concerns the polecap geometry. In the KS model the accreting polecap(s) are assumed to be circular and to occupy a large fraction of the white dwarf's surface ($f = 0.25$). In the accretion curtain model, however, arc shaped emission regions, which partially trace circles centred on the magnetic axis and which have $f = 0.01$ (Rosen 1992), are favoured.

Recent *Ginga* results have shown that the X-ray pulses seen in intermediate polars are more complex than simple sinusoids (Ishida et al. 1992; Norton et al. 1992a; NMLW). Moreover, there clearly exist modulated components at high energies (e.g., 'notches') which cannot be due to photoelectric absorption, as the cross-section for this process is proportional to ν^{-3} (where ν is the radiation frequency). This suggests (see also Norton & Watson 1989) that KS's occultation picture may play *some* rôle in the modulation. It is also likely that further energy-independent mechanisms such as electron scattering are operating (Rosen et al. 1991), but it has been emphasised (Rosen 1992) that 'unless the material further out in the curtain is significantly ionised or is deficient in heavy elements, electron scattering alone probably can not explain the high-energy rotational modulation in intermediate polars [sic.]'.

1.5.4.2 Beat modulation

There are two ways to generate the optical photometric beat modulation. The most favoured is by reprocessing of X-ray flux from the white dwarf at structures fixed in the binary frame (e.g., the surface of the secondary, or a non-axisymmetric

disc structure). The white dwarf is assumed to rotate (period P_{spin}) in the same sense as the orbital motion (period P_{orb}), and therefore has to 'catch-up' with the reprocessing site—which will since have moved on—once every rotation. Thus, the reprocessing site is illuminated by the white dwarf at the beat period, P_{beat}, given by

$$\frac{1}{P_{beat}} = \frac{1}{P_{spin}} - \frac{1}{P_{orb}}, \tag{1.1}$$

producing the observed optical beat modulation at a negative orbital-sideband frequency (a retrograde rotation would produce a *positive* sideband, but this situation is unlikely to occur). This relationship was shown to account for the period pattern in TV Col (Motch 1981), and was recognised by Patterson & Price (1981) as being able to link the three periods seen in AO Psc to within one part in a thousand. Equation 1.1 is now known to describe similar period relationships in other systems.

Not all of the X-rays incident on the reprocessing site will be re-emitted at optical wavelengths. Some of the radiation will be directly reflected and so, theoretically, this picture should also be capable of producing an *X-ray* beat period. However, in practice this mechanism is very inefficient. This is because the hard X-ray albedo is low (only ~ 0.3), and the solid angle subtended at the white dwarf by the reflection site is likely to be very small (even the secondary is unlikely to subtend an angle of more than $\sim 30°$). These factors significantly reduce the power in the reflected X-ray signal. Buckley & Tuohy (1989) invoked this model for TX Col, but had to assume, therefore, that the X-rays from the white dwarf were concentrated, or 'beamed', otherwise the strength of the reflected signal is insufficient to account for the observed amplitude of the modulation. X-ray beaming mechanisms in intermediate polars have not been studied and are poorly understood. Furthermore, it is unclear from this model why the X-rays from the white dwarf would only be seen after reflection, and not directly: if the X-ray beam is seen directly its power should always exceed that in the beat-pulse simply because of the albedo attentuation.

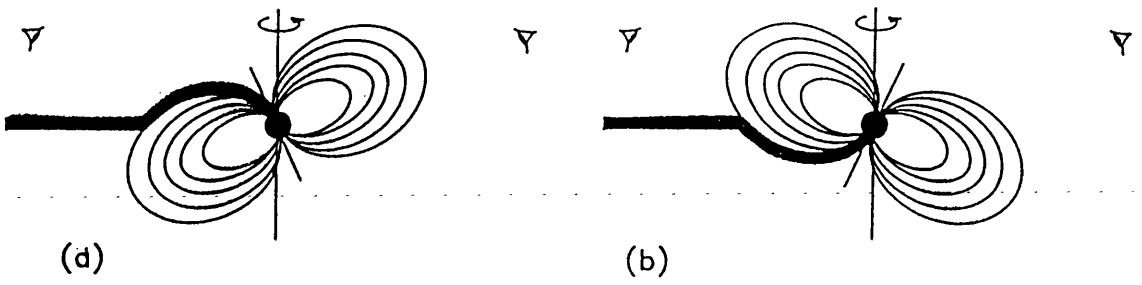

FIGURE 1.4: *Schematic representation of a discless accretion scenario in an intermediate polar (adapted from Norton et al. 1992a). (a) shows the system in the maximum of its beat cycle, when the upper pole preferentially accretes. In (b), the lower pole accretes and the minimum in the beat cycle is observed. See the discussion in §1.5.4.2.*

A second way to generate a beat-period modulation, in both X-rays and in the optical, has been discussed extensively by Norton et al. (1992a; see also NMLW) in view of their *Ginga* results from FO Aqr and BG CMi (refer to figure 1.4). A full disc is assumed absent, but a truncated non-accretion disc (e.g., King, Mouchet & Lasota 1991; see §1.5.3) may be present. For half a beat cycle, either the top or bottom magnetic pole will preferentially accrete. Half a beat cycle later, this switches over, so that the opposite pole becomes active instead. When the upper pole is active (figure 1.4[a]), the system exhibits a maximum in its beat-pulse in both X-rays and in the optical. This will be true irrespective of the orbital phase, although the intensity of the beat-pulse will be orbitally modulated (see §1.5.4.3). Half a beat cycle later, when the lower pole accretes, a minimum is observed (figure 1.4[b]). The easiest way to envisage the modulation is to imagine the situation in the event of a low inclination. In this case, a square-wave beat modulation is observed, as the upper pole appears to switch 'on' and 'off' every half cycle, and the lower pole is never seen.

This model would seem ~~the only~~ a very viable way to explain the pulsations seen in X-rays from BG CMi (NMLW), requiring the spin period to be 847 s with 913 s as the beat period. However, optical spectroscopy (see chapter 4) ~~are~~ is unable to

satisfactorily resolve this issue.

1.5.4.3 Orbital modulation

Orbital modulation is seen in intermediate polars, both in the optical and in the X-ray band. X-ray orbital modulation is discussed extensively in chapter 2. In optical photometry, the orbital modulation generally takes the form of a quasi-sinusoidal variation ~~(e.g., see figure 3.3)~~. Optical eclipses have been reported in four systems (DQ Her, TV Col, FO Aqr, and EX Hya; see the references in table 1.1), with only EX Hya and H0253+193 exhibiting an eclipse in the X-ray band. The quasi-sinusoidal morphology of the non-eclipse modulation immediately suggests the varying aspect of a region of enhanced emission to be the cause. The sites which are generally considered to contribute to this modulation are the heated surface of the secondary (e.g., Davey & Smith 1992), a disc bulge, or, in a discless system, a bright magnetospheric impact region, or combinations of these.

An orbital modulation in both X-rays and the optical band will also be produced in the discless scenario of NMLW discussed in §1.5.4.2. At any given orbital phase, when the active pole points away from the observer (e.g., viewing from the right in figure 1.4[a]), the accretion shock is seen from the side, through a low optical depth, and the intensity at this beat phase and orbital phase will be at a maximum. However, half an orbital cycle later, though still at the same beat phase (looking from the left, with the active pole now pointing *towards* the observer), the radiation from the white dwarf will be seen through a larger optical depth, resulting in a weaker flux.

In three eclipsing systems (EX Hya, DQ Her, and FO Aqr), optical spectroscopic observations reveal a 'rotational disturbance' in the emission lines during the eclipse phase (the necessary data have not been published on the other two eclipsing systems, TV Col and H0253+193). In other words, the emission lines show a red excursion at the onset of the eclipse, minimum intensity at mid-eclipse, and a blue excursion at the end as first the blueshifted portions of the disc, followed

by the redshifted regions, are obscured by the secondary. Indeed, in FO Aqr, a photometric eclipse is not readily apparent, and the eclipse was actually discovered *by virtue* of a rotational disturbance (see Hellier, Mason & Cropper 1989). A rotational disturbance provides evidence of material circulating in a disc or ring about the primary. However, this evidence should be regarded with caution because Williams (1989) has shown that not all eclipsing systems show this signature.

Optical spectroscopy also reveals orbital modulation of the emission line profiles by processes other than rotational disturbance. Firstly, some systems exhibit orbital phase-dependent self-reversal in their emission lines. For example, AO Psc shows a double-peaked He I λ 4471 line, which is attributed to line absorption in material at a disc/stream impact site (Hellier, Cropper & Mason 1991), such as that material which has been postulated to cause the X-ray orbital modulation in low-mass X-ray binaries (Mason 1989). Similar X-ray features in intermediate polars may arise from the same processes (see chapter 2).

Secondly, the emission lines of intermediate polars often show an orbital S-wave: a component may be present which executes a sinusoidal modulation about the system zero-velocity as a function of orbital phase, making an S-shaped pattern in trailed spectra. The modulation may be caused by the same bright-spot which is believed responsible for the smooth photometric modulation. As the system orbits its centre of mass, the line-emitting gas in the enhanced region exhibits a modulated radial Doppler shift. The semi-amplitude of the velocity is typically $\sim 400\,\mathrm{km\,s^{-1}}$ (see Hellier 1991 and references therein). This amplitude has been used as an argument that such systems contain discs (Hellier 1991), on the grounds that the amplitude would be higher if the S-wave component originated in the white dwarf's magnetosphere.

In subsequent chapters I present an analysis and interpretation of original observational data of intermediate polars. Many aspects of the current understandings of magnetic cataclysmic variable research, including those outlined in the present chapter, will be seen in further detail.

2. X-RAY ORBITAL MODULATIONS IN INTERMEDIATE POLARS

You asked, 'What is this transient pattern?'
If we tell the truth of it, it will be a long story;

Omar Khayyam
Attributed (c. 1100)

2.1 INTRODUCTION

Intermediate polars are among the most X-ray-bright cataclysmic variables, and observations of these systems using *EXOSAT* during the past decade have proven them to be invaluable for the study of accretion flows in magnetically controlled environments. All the systems known at that time were observed more than once, and at least two new members (GK Per and TX Col) were proposed on the strength of pulsations seen in the *EXOSAT* data (see Osborne 1988 for a review). These pulsations, caused by a spinning, magnetic white dwarf, have been extensively studied by Norton & Watson (1989). In addition to the pulsations, the *EXOSAT* observations showed variations on a timescale of a few hours in several systems. These features, usually taking the form of broad 'dips' in the lightcurves, are now recognised in the literature as being orbitally related in some systems; in other systems, however, the dips have not been investigated sufficiently to determine their nature.

To investigate the causes of the X-ray dips in intermediate polars in general I have made a systematic study of the *EXOSAT* archive timeseries data, the results of which are presented in the current chapter. Similar dip phenomena in the lightcurves of some low-mass X-ray binaries (LMXRBs, reviewed by Mason 1989) have given rise to a model wherein structured accretion discs play a significant rôle in modulating the light output at the binary period. However, it is still unclear whether intermediate polars contain accretion discs: the similarity between the orbital modulations found in LMXRBs and the dips observed in intermediate polars presents an opportunity to expand upon this debate.

2.2 OBSERVATIONS

In this chapter I consider TV Col, TX Col, FO Aqr, AO Psc, BG CMi, V1223 Sgr, EX Hya, and GK Per. These comprise the complete set of (then known) intermediate polars that were observed with *EXOSAT*. A journal of the observations is contained in table 2.1 (see White & Peacock 1988 for a review of *EXOSAT* and its instruments).

For the analysis I extracted medium-energy (ME) timeseries data covering the energy range 1.4–8.5 keV. These data were then split into two passbands (1.4–4.5 keV and 4.5–8.5 keV) to provide a measurement of the hardness ratio. The choice of 4.5 keV as the pivotal energy in this analysis is arbitrary, but it will be seen that photoelectric absorption plays a substantial rôle in producing dips in the lightcurves of intermediate polars. This process is strongly energy dependent (cross-section $\propto \nu^{-3}$, where ν is the radiation frequency), and is expected not to operate as efficiently, if at all, at high energies.

In addition to the ME data, I have examined the low-energy (LE, 0.05–2 keV) timeseries data from all systems except FO Aqr and GK Per. These latter two systems were not detected significantly by the LE imaging telescope. For example, the LE count-rate from FO Aqr was less than 0.005 count s^{-1} during observations 1983/284 (1983, day 284) and 1985/295–296—a factor 2–6 less than those observed

System	No.	Date	Day number	Data used
TV Col	1	1983 Nov 26	330–331	ME, LE1
	2	1983 Nov 28	332	ME, LE1
	3	1985 Nov 17	321–323	ME, LE1
TX Col	1	1985 Feb 23	054	ME, LE1
AO Psc	1	1983 Sep 14	257–258	ME, LE1
	2	1983 Sep 17	260	ME, LE1
	3	1985 Oct 23	296–297	ME, LE1
	4	1985 Oct 26	299–300	ME, LE1
FO Aqr	1	1983 Aug 10	222	ME
	2	1983 Oct 11	284	ME
	3	1985 Oct 22	295–296	ME
BG CMi	1	1984 Jan 4	004–005	ME, LE1
	2	1985 Apr 10	100–101	ME, LE1
V1223 Sgr	1	1983 Oct 11	284–285	ME, LE1
	2	1984 Aug 29	242–243	ME, LE1
	3	1984 Sep 1	245–246	ME, LE1
EX Hya	1	1983 Jul 30	211–213	ME, LE1
	2	1984 Feb 4	035	ME, LE1
	3	1985 Jul 14	195–196	ME, LE1
	4	1985 Jul 15	196–197	ME, LE1
	5	1985 Jul 17	198	ME, LE1
GK Per	1	1983 Aug 9	221	ME
	2	1983 Aug 15	227–228	ME
	3	1983 Aug 24	236	ME
	4	1984 Sep 2	245–246	ME
	5	1984 Jan 9	009–010	ME

TABLE 2.1: *EXOSAT observation log.*

for the other systems. The appendix (§A.5) details the reduction techniques used.

2.3 DATA ANALYSIS

The ME data on six of the systems, binned at one spin-cycle resolution, are shown in figure 2.1. The bins typically contain 1000–4000 counts, so photon errors are $\sim$2–3%. Hence, the variability seen in this diagram is statistically significant and can be attributed to either flickering or orbital modulation. One can distinguish between the two, however, only by repetition with orbital phase. Thus, the data are plotted against orbital cycle to emphasise any such variability. The references used for the orbital ephemerides are discussed in §2.3.2, but in general, binary phase zero is defined as either optical photometric minimum, or, where known (e.g., in eclipsing systems) inferior conjunction of the secondary (i.e., when the secondary is between the observer and the white dwarf). To reveal any energy dependences of the variability shown in figure 2.1, the ME data are shown again in figures 2.3–2.8 along with the LE data and the ME hardness ratio at the same time resolution. These diagrams are discussed in §2.3.2.

EX Hya is omitted from figure 2.1 as binning over the spin period (67 min) prevents resolution of the orbital cycle (98 min). Instead, I present the data for EX Hya folded on the orbital cycle in figure 2.9. GK Per is also excluded from figure 2.1. Obviously, this system's 2 d orbital period (Crampton, Cowley & Fisher 1986, hereafter CCF) means that the data are not suitable for studying any orbital modulation—only about 75% of the orbit was covered by *EXOSAT*. However, GK Per has been included in this study because the X-ray lightcurves, particularly during 1983, exhibit features similar to those found in other intermediate polars (see §2.3.2.8).

2.3.1 ORBITALLY RELATED SPIN-CYCLE CHANGES

Where a significant orbital modulation is seen, and where feasible, I have searched

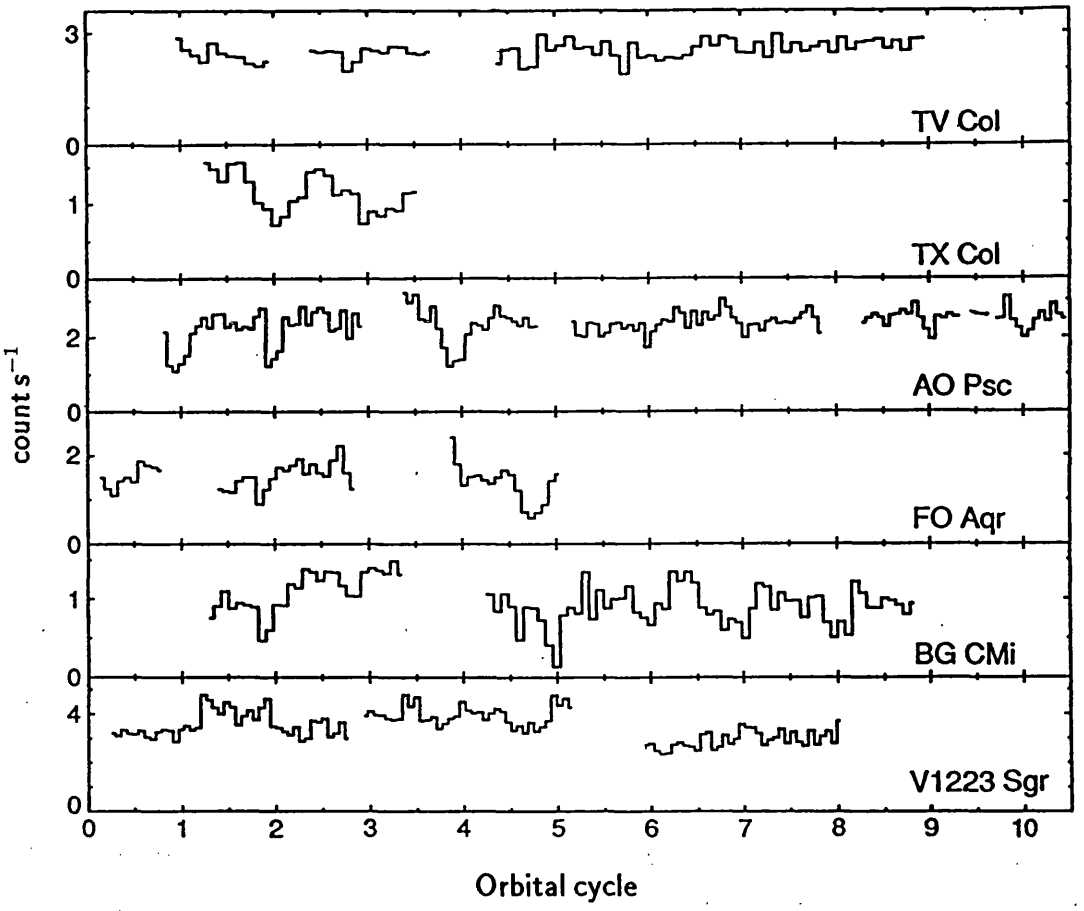

FIGURE 2.1: *The EXOSAT ME 1.4–8.5keV lightcurves showing the variation as a function of orbital cycle. All systems are shown except EX Hya and GK Per. In FO Aqr and TV Col orbital phase zero represents the optical eclipse, whereas in BG CMi, AO Psc, and V1223 Sgr the same phase corresponds to the orbital photometric minimum. In TX Col the orbital X-ray minimum has been arbitrarily defined as phase zero. Orbital ephemerides are from Kaluzny & Semeniuk 1988 (AO Psc), Osborne & Mukai 1989 (FO Aqr), Jablonski & Steiner 1987 (V1223 Sgr), Hellier (private communication, TV Col), and Augusteijn, van Paradijs & Schwarz 1991 (BG CMi).*

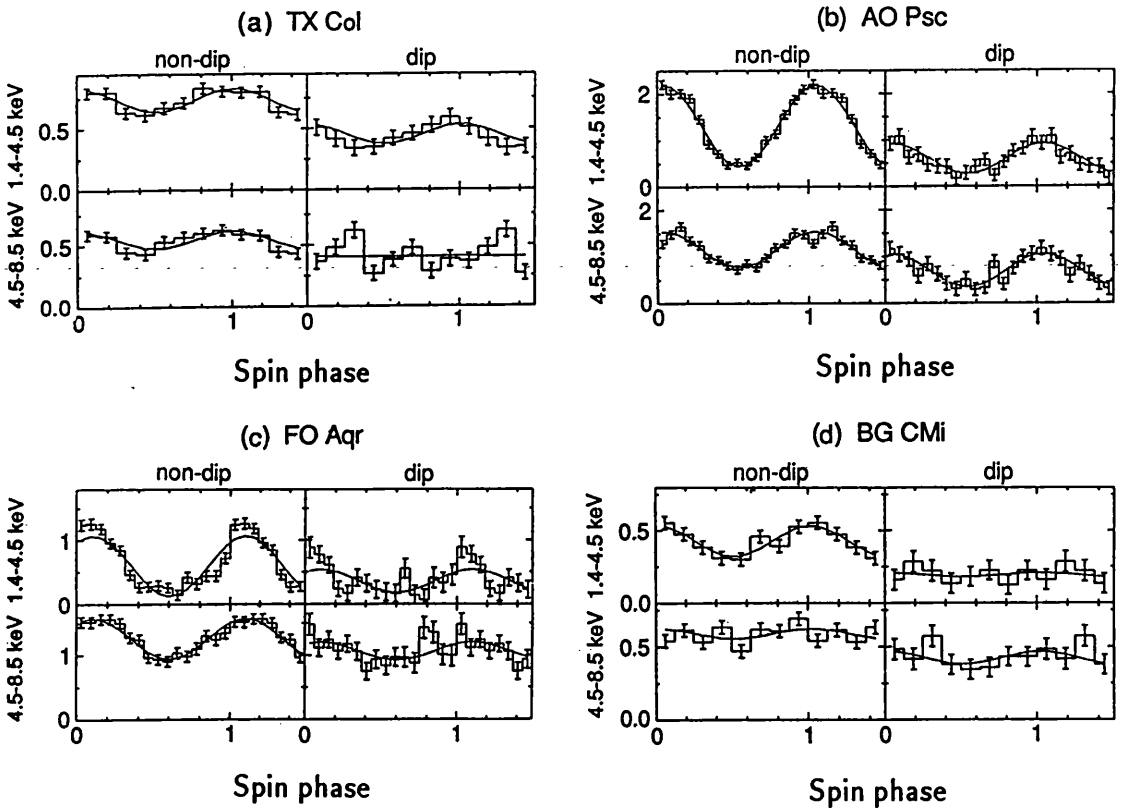

FIGURE 2.2: *The spin-pulse profiles obtained by folding the data from dip and non-dip regions, shown together with the best-fitting sinusoids. The phasing is arbitrary, and two cycles are shown for clarity. The calculated pulse-fractions are given in table 2.2.*

for possible influences on the spin pulsations by comparing the pulse-fractions during and outside orbital minima. Sections of ME data at minimum and out of minimum were chosen (the chosen regions are shown in figures 2.4–2.7), folded on the spin cycle, and then rebinned. The folded data are shown in figure 2.2. I then fitted each of these folded datasets with a sinusoid of the form

$$y = c + a \sin\left(2\pi[x - \phi]\right), \tag{2.1}$$

whilst constraining the phase of the sinusoids to be the same in both orbital maximum and minimum data as that phase calculated when the entire dataset is folded and fitted with a sinusoid. Here, x is the phase of the folded data, and c, a, and ϕ are the mean offset, semi-amplitude and phase of the fitted sinusoid respectively.

System	Obs no.	Region	Pulse-fraction (%)	
			1.4–4.5 keV	4.5–8.5 keV
TX Col	1	non-dip	24 ± 4	24 ± 6
		dip	31 ± 10	1 ± 12
AO Psc	1	non-dip	80 ± 3	50 ± 3
		dip	71 ± 10	68 ± 9
	2	non-dip	74 ± 3	44 ± 3
		dip	57 ± 12	30 ± 9
	Mean	non-dip	77 ± 2	47 ± 2
		dip	65 ± 8	49 ± 6
FO Aqr	2	non-dip	88 ± 5	40 ± 3
		dip	69 ± 17	21 ± 7
	3	non-dip	82 ± 7	60 ± 5
		dip	34 ± 46	48 ± 14
	Mean	non-dip	86 ± 4	45 ± 3
		dip	64 ± 16	26 ± 6
BG CMi	1	non-dip	42 ± 7	11 ± 6
		dip	13 ± 26	19 ± 12

TABLE 2.2: *Spin pulse-fractions for four intermediate polars. Errors are* 3σ.

Finally, I calculated the pulse-fractions as the ratio of the full amplitude of the best-fitting sinusoid to maximum intensity of that sinusoid. Table 2.2 lists the calculated pulse-fractions.

2.3.2 RESULTS FROM INDIVIDUAL SYSTEMS

2.3.2.1 TV Columbae (H0526−328)

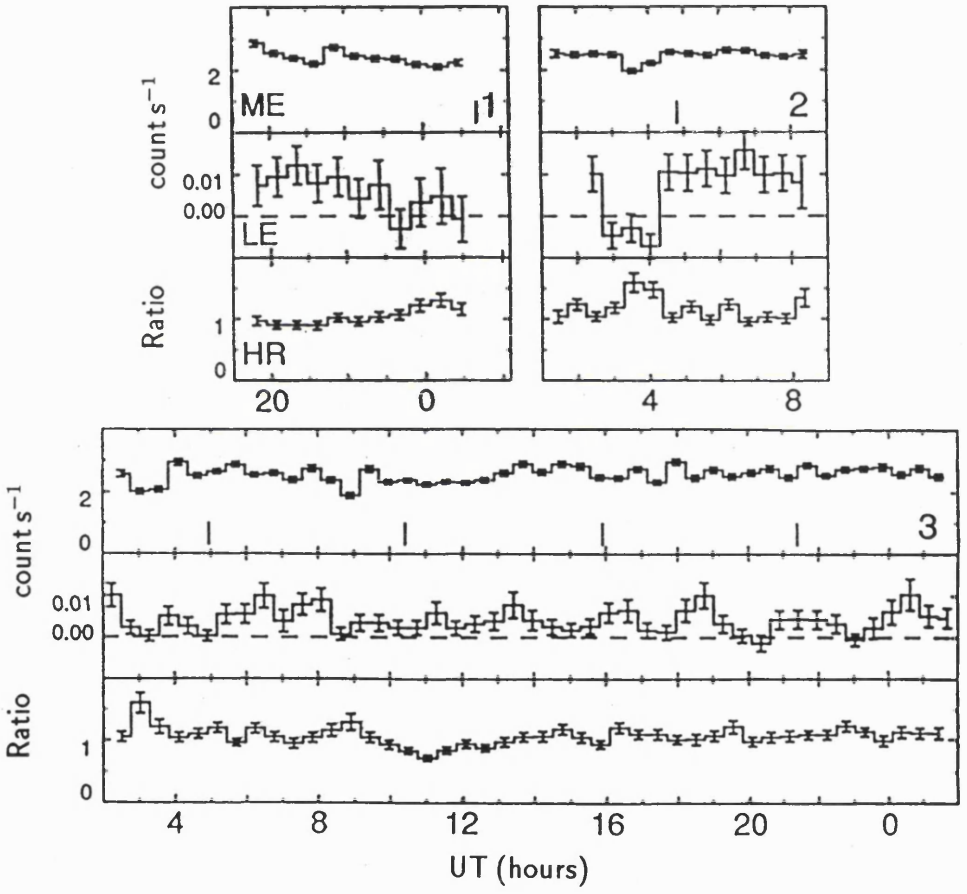

FIGURE 2.3: *The EXOSAT ME data of TV Col as in figure 2.1, together with the LE data and the hardness ratio. The resolution is one spin cycle. Observation numbers are given on the right in the ME panels. The tick marks next to the ME data indicate the expected time of the eclipse according to Hellier (private communication).*

There is a dip in both the ME and LE data near 04:00 UT in the second observation

of TV Col (figures 2.1 and 2.3), preceeding one found by Schrijver et al. (1985) by an integral number of orbital cycles. However, this latter dip, at 23:40 UT, is not apparent when the data are binned at one spin-cycle resolution. Similarly, as reported by Schrijver et al. (1987) there are two dips separated by an orbital cycle near the beginning of the much longer third observation (near 03:00 UT and 09:00 UT). However, these dips do not repeat later in the observation. The observed increase in hardness ratio during the dip in the second observation and the greater depth of the LE dips compared to the ME dips indicate clearly that the dipping mechanism is energy dependent.

It was not possible to investigate changes in the spin-pulse of TV Col as a function of orbital phase, as the dips cover an insufficient number of spin cycles, and because the spin-pulse is very weak.

Hellier, Mason & Mittaz (1991) have reported an observation of an eclipse in this system and have derived an eclipse ephemeris based upon their data. A revised version of this ephemeris (C. Hellier, private communication) shows that the dips occur 0.2–0.3 orbital cycles prior to the eclipse (see figure 2.1).

2.3.2.2 TX Columbae (H 0542−407)

Both LE and ME data from TX Col (figures 2.1 and 2.4) display a strong, quasi-sinusoidal variation on a timescale compatible with the 5.7 hr orbital period (Buckley & Tuohy 1989). Again the modulation is energy dependent, being strongest in the LE band and weakest at 4.5–8.5 keV.

Measuring the spin pulse-fraction at different orbital phases is not straightforward in TX Col, as the system shows a beat-period pulsation comparable in amplitude to that of the spin-pulse (Buckley & Tuohy 1989). These interfere constructively at orbital X-ray minimum and destructively at orbital X-ray maximum. Therefore, I have subtracted the best-fit beat-period sinusoid from the data before measuring the spin pulse-fractions. To calculate the sinusoid parameters the data were first folded on the beat period (2100 s), binned into eight phase bins, and

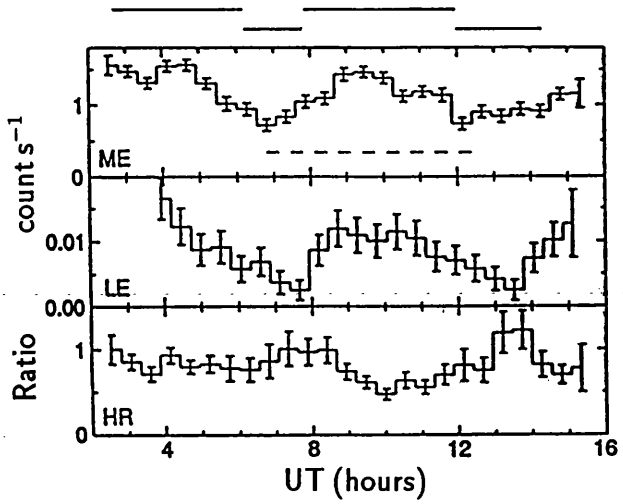

FIGURE 2.4: *As figure 2.3, but for TX Col. As the orbital phasing is unknown, I have drawn dashed lines to illustrate one cycle of the binary period. Solid lines above the HR panel show (upper lines) the extent of the ME data from non-dip regions used for the spin-pulse analysis and (lower lines) the corresponding 'dip' regions.*

fitted with a sinusoid of the form given by equation 2.1. When the new datasets are folded on the spin period, the result shown in figure 2.2(a) is obtained. At 1.4–4.5 keV, the pulse-fraction remains unchanged (see table 2.2); however, at 4.5–8.5 keV the spin-pulse is not seen at orbital minimum and it is not possible to tell whether this is a change in the spin-pulse, or in the beat-pulse, or the result of flickering.

The phasing of the X-ray minimum cannot be inferred in TX Col due to a lack of observational history. Therefore, I have arbitrarily defined the X-ray orbital minimum as phase zero.

2.3.2.3 AO Piscium (H2252−035)

Dips are seen repeating with the orbital cycle in all of the *EXOSAT* observations of AO Psc (see figures 2.1 and 2.5), although they are more prominent in the first two observations (from 1983) than in the second two (from 1985). Many of the dips are deeper at lower energies, showing increases in hardness ratio. The LE flux

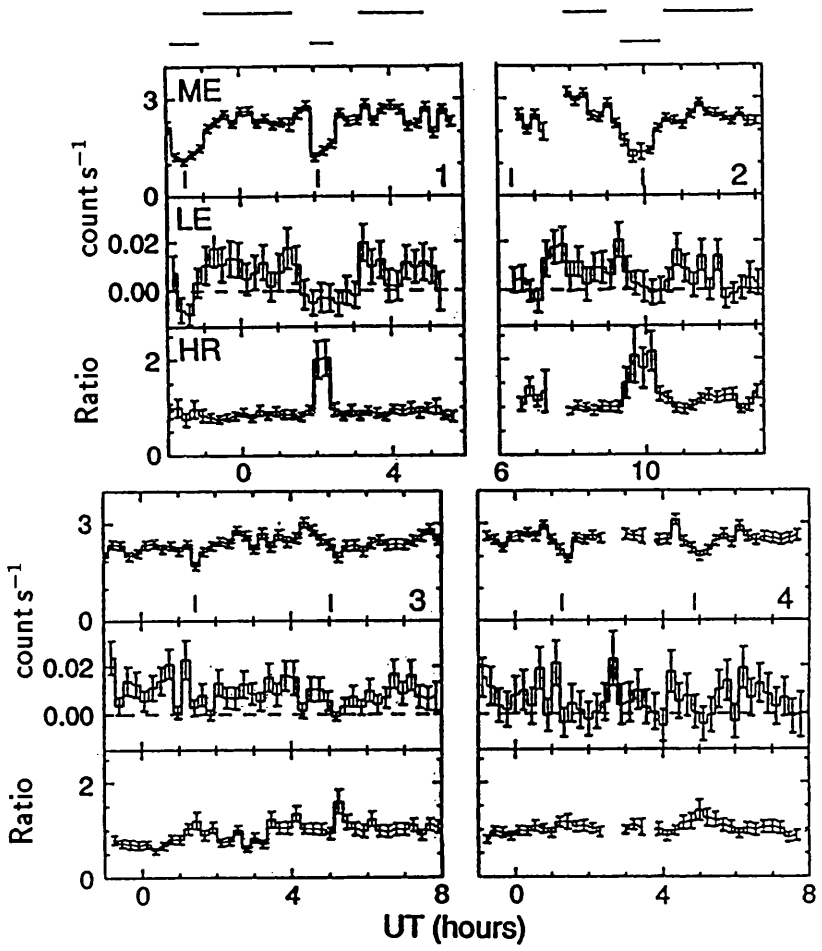

FIGURE 2.5: *As figure 2.3, but for AO Psc.*

is entirely extinguished during the dips. The spin pulse-fraction in both ME bands does not change as a function of orbital phase (see figure 2.2[b] and table 2.2).

The phase of inferior conjunction of the secondary is unknown in AO Psc. However, the dips occur at the minimum of the optical orbital modulation according to the ephemeris of Kaluzny & Semeniuk (1988). At this orbital phase the optical spin-pulse and beat-pulse arrive in phase, and an optical 'S-wave'[1] emission line region, perhaps arising from the impact of the accretion stream with the edge of a disc, is at inferior conjunction (Hellier, Cropper & Mason 1991). This suggests that inferior conjunction of the secondary follows ~ 0.1 orbital cycles after the

[1]See §1.5.4.3 for a discussion of the S-wave.

X-ray/optical minimum.

2.3.2.4 FO Aquarii (H2215−086)

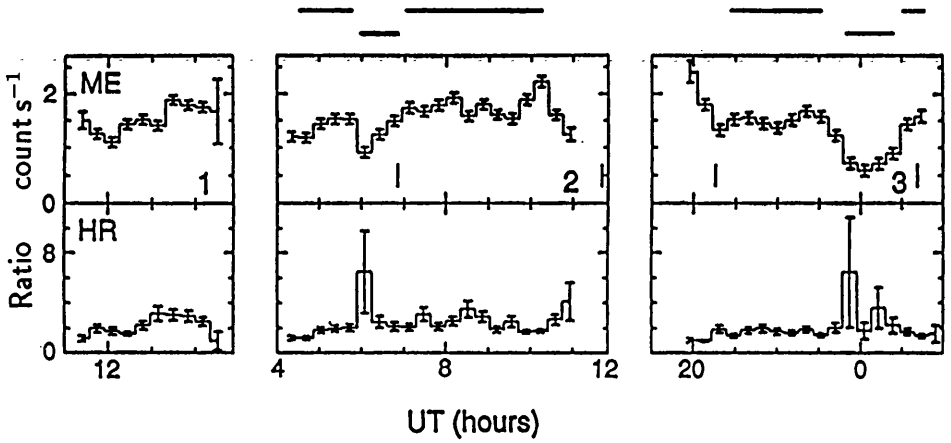

FIGURE 2.6: *As figure 2.3, but for FO Aqr. Note that LE observations are not included.*

In FO Aqr, the phasing of inferior conjunction of the secondary is established by an optical eclipse (Hellier, Mason & Cropper 1989), and in both observations of FO Aqr which cover the phases *preceding* eclipse (the second and third), dips are present. The dip in the second observation begins later (phase 0.8) than that in the third (phase 0.6), but it is narrower and they both end at phase ~ 0.0. Both observed dips are coincident with increases in hardness ratio (figure 2.6), although this is not significant given the error bars in these regions.

There is a reduction of the pulse-fraction in the 4.5–8.5 keV band during the dip in the second observation (figure 2.2[c] and table 2.2), but note that this dip covers only three spin cycles. A *Ginga* observation of FO Aqr confirms the presence of an X-ray orbital modulation (Norton et al. 1992a). There is also an apparent change in the X-ray spin-pulse with orbital phase, although this might be due to interference from the beat-pulse seen in this observation. According to the ephemerides of Osborne & Mukai (1989) the optical spin-pulse and beat-pulse arrive in phase during the X-ray orbital minimum.

2.3.2.5 BG Canis Minoris (3A 0729+103)

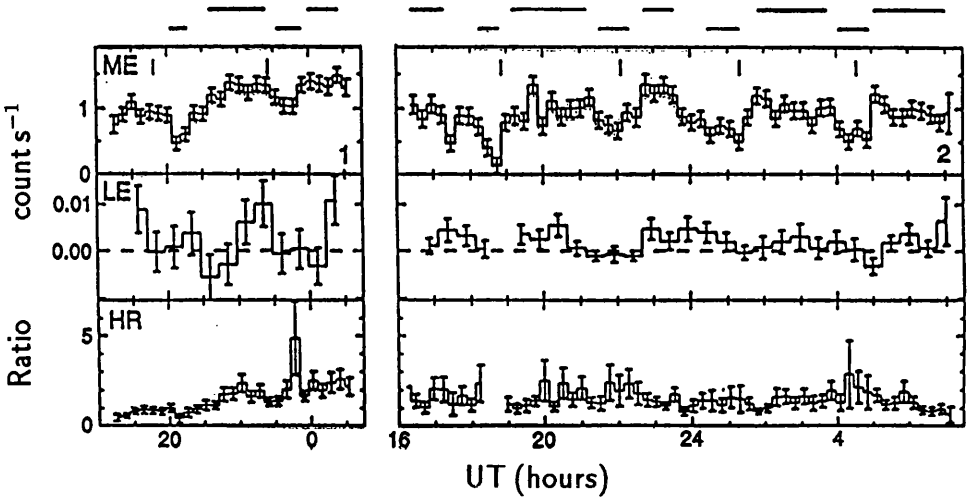

FIGURE 2.7: *As figure 2.3, but for BG CMi. As the LE data are particularly sparse, they are binned over two spin cycles rather than one.*

The ME data on BG CMi (figures 2.1 and 2.7), both from 1984 and 1985, reveal a strong orbital modulation, as reported by McHardy et al. (1987). The LE data are statistically poor but show similar variability. Once again the modulation is in general strongest in the LE, and weakest (though still apparent) at 4.5–8.5 keV. According to the ephemeris of Augusteijn, van Paradijs & Schwarz (1991) the X-ray orbital minima occur in phase with the optical modulation. However, the phase of inferior conjunction of the secondary is unknown.

Following a *Ginga* observation of BG CMi (Norton et al. 1992b, hereafter NMLW) the identification of the 913 s pulse with the spin period (McHardy et al. 1982, 1984, 1987) is now uncertain (this is discussed extensively in chapter 4). NMLW suggest that the true spin period is 847 s, and that 913 s is the usual negative orbital sideband. As the 847 s period is not seen in *EXOSAT* data I was unable to test for the presence of orbital modulation of the 847 s pulse. On the other hand, no change in the 913 s pulse-fraction as a function of orbital phase is detected in the *EXOSAT* data (see figure 2.2[d] and table 2.2), but the superior statistics of the *Ginga* data show the 913 s pulse to be orbitally modulated.

2.3.2.6 V1223 Sagittarii (4U1849−31)

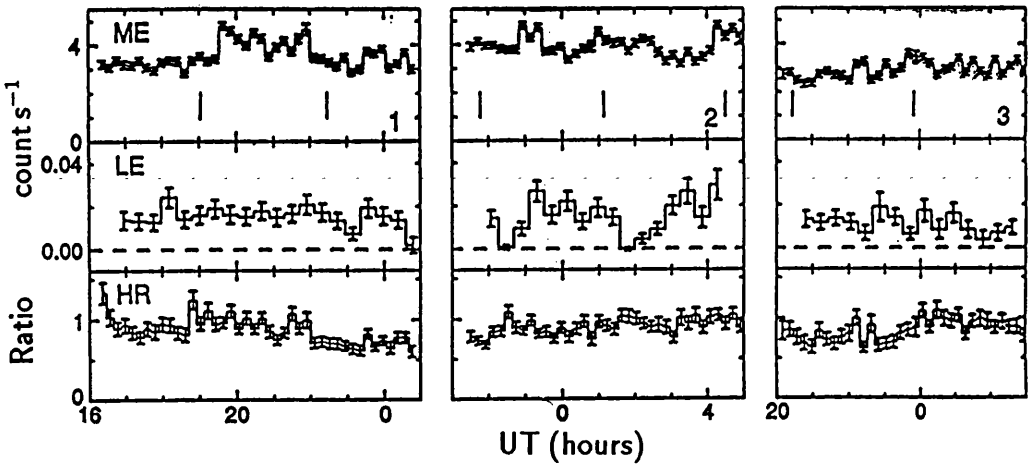

FIGURE 2.8: *As figure 2.3, but for V1223 Sgr. Note that the LE data are again binned at a resolution of two spin cycles.*

The ME lightcurves of V1223 Sgr are very erratic and show no orbitally related modulation. In the LE data from the second observation (see figure 2.8), however, there are two points where the LE emission is extinguished, separated by one orbital cycle.

Again the phasing of the secondary is not established in V1223 Sgr. Jablonski & Steiner (1987) calculated that the optical spin and beat modulations in V1223 Sgr arrive in phase 0.10 ± 0.03 orbital cycles before the photometric minimum. In comparison, the LE dips occur 0.25 cycles *after* the photometric minimum. This is in contrast to the previously discussed systems (FO Aqr, BG CMi, and AO Psc) where the dips occur either at photometric minimum or when the optical beat-pulse and spin-pulse are in phase.

2.3.2.7 EX Hydrae

The phase of inferior conjunction of the secondary in EX Hya is established by an optical and X-ray eclipse. The eclipse can be seen in figure 2.9, which shows the ME data from the fourth observation of EX Hya folded on the orbital cycle. Aside

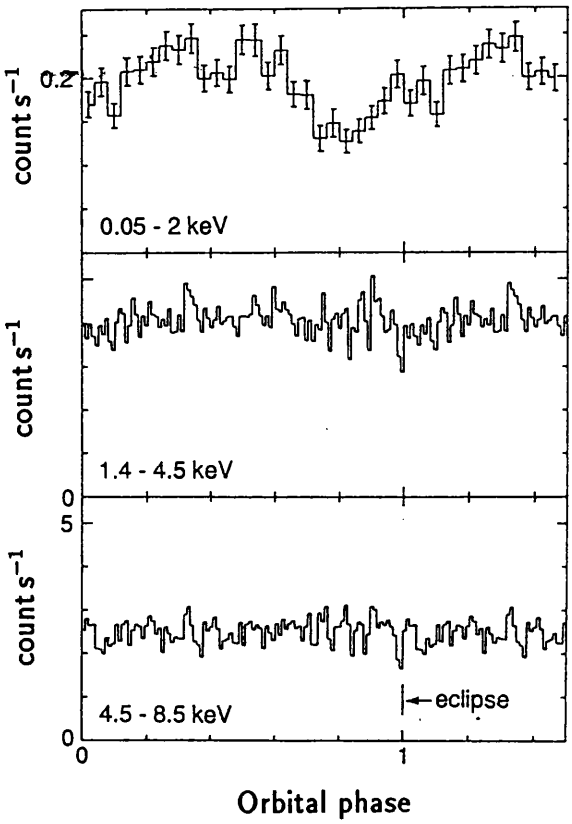

FIGURE 2.9: *The EXOSAT ME and LE lightcurves of EX Hya folded according to the orbital ephemeris of Jablonski & Busko (1985).*

from the eclipse, no orbital modulation is evident in the ME data. However, as reported by Córdova, Mason & Kahn (1985), there is a prominent asymmetric dip of fractional depth 60% in the LE data, centred ~ 0.15 orbital cycles before the eclipse phase.

2.3.2.8 GK Persei (Nova Per 1901)

Figure 2.10 shows the ME data from all five observations of GK Per plotted as a function of orbital phase and binned at one spin-cycle resolution. The phase accords to the radial velocity ephemeris of CCF, with orbital phase 0.75 representing inferior conjunction of the secondary (i.e., *absorption* lines switching from blueshifted to redshifted). Obviously, the long orbital period of this system does not permit a detailed examination of the lightcurves in a search for evidence of

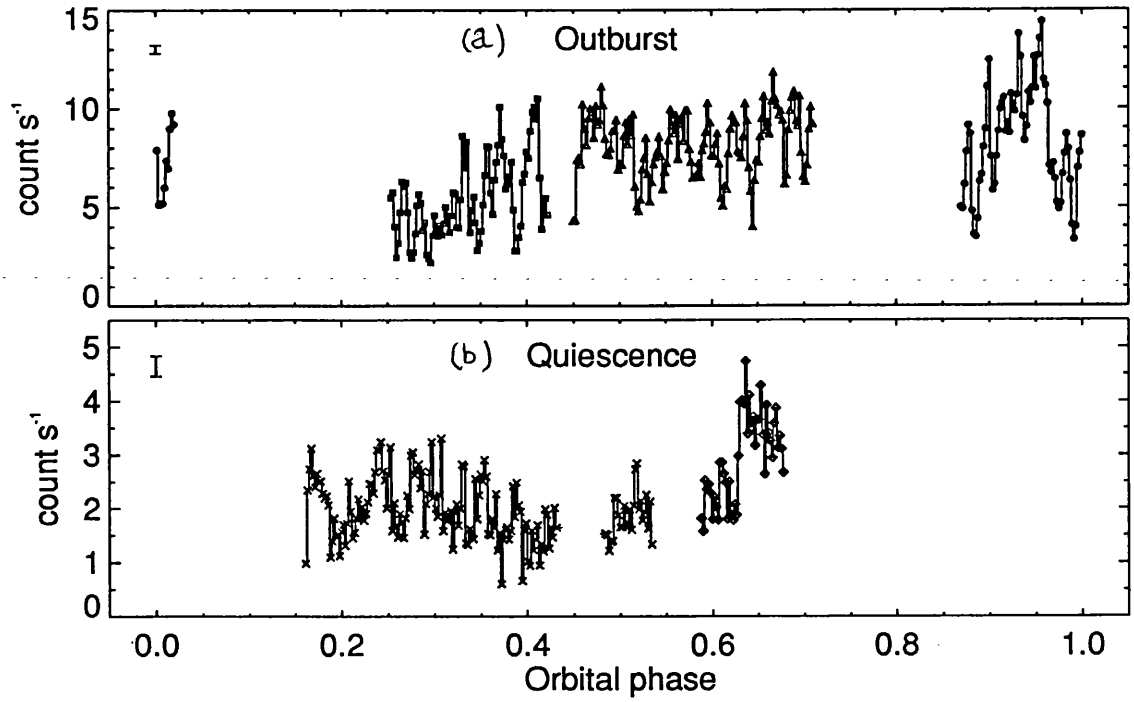

FIGURE 2.10: *The ME lightcurves of GK Per during (a) outburst and (b) quiescence, plotted as a function of orbital phase. Typical error bars are indicated in the top left of each panel. Observation numbers are: 1—filled circles; 2—squares; 3—triangles; 4—diamonds; 5—crosses.*

orbital modulation—only 75% of the orbital cycle was covered by *EXOSAT*. However, figure 2.10 does indicate that the lightcurve is very variable, both in outburst and in quiescence.

The variability during outburst is seen in more detail in figure 2.11 which presents the ME outburst lightcurves again, and which also shows the hardness ratio as a function of both time and count-rate. In all cases a very prominent modulation is observed on timescales upwards of ~ 0.5 hr; a Fourier analysis indicates that the variability is not strictly periodic. Watson, King & Osborne (1985) commented on this variability, but did not investigate any energy dependence. In fact, there is a strong anticorrelation between the hardness ratio and count-rate in the second and third observations. The observed behaviour therefore mimics the variability seen in the previous systems. In the first observation, however, the hardness ratio is anticorrelated with the count-rate only in selected portions of

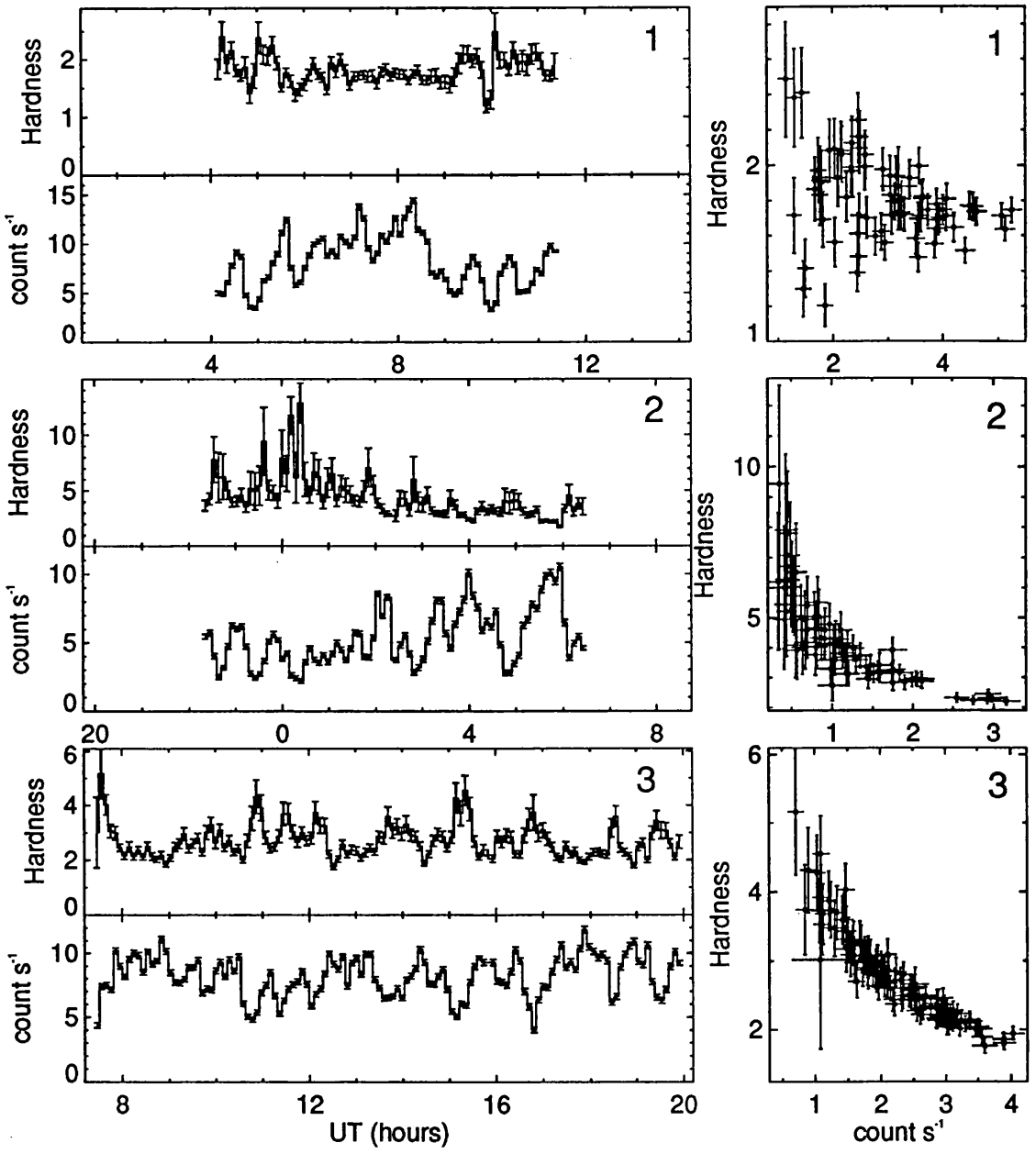

FIGURE 2.11: *The ME lightcurve and hardness ratio of GK Per during the 1983 outburst. The panels on the right show the hardness ratio plotted as a function of the count-rate to emphasise further any relationship. A clear anticorrelation is indicated in the second and third observations, whilst a positive correlation is seen in the first observation.*

the lightcurve, whereas in other parts of the same lightcurve the variability and hardness ratio are *positively* correlated (e.g., near 05:00 UT, 06:00 UT, and 09:00–10:00 UT). This is also seen in the fourth and fifth observations (quiescence), where, for example, the hardness ratio remains approximately constant (~ 1.0) throughout the variability, but reduces to ~ 0.3 during the dip in lightcurve 5 at orbital phase 0.2 (figure 2.10). Such behaviour is not seen in any other intermediate polar.

2.3.3 SUMMARY OF RESULTS

I have found evidence for X-ray orbital modulation in all intermediate polars examined in this chapter except GK Per, although in the case of V1223 Sgr it is marginal. The modulations are generally deeper at lower energies and in two cases (V1223 Sgr and EX Hya) are seen in the LE band only. This energy dependence suggests that photoelectric absorption contributes significantly to the orbital modulation mechanism in intermediate polars.

In the eclipsing systems FO Aqr, EX Hya, and TV Col the minima of the modulations occur ~ 0.2 orbital cycles before inferior conjunction of the secondary. The dips seen in AO Psc most probably occur at a similar orbital phase (see §2.3.2.3 and figure 2.1). For the remaining stars (V1223 Sgr, TX Col, and BG CMi) the phasing is less certain. In BG CMi the X-ray dips occur in phase with the optical minima, as seen in AO Psc, and so may again have a similar phasing. In contrast, the dips in V1223 Sgr (seen in the LE data only, §2.3.2.6) occur 0.25 orbital cycles *after* the optical minimum, although one cannot be certain that these are related to the orbital cycle.

2.4 DISCUSSION

2.4.1 POSSIBLE X-RAY ORBITAL MODULATION MECHANISMS

This compilation shows that intermediate polars exhibit variations in their X-ray lightcurves which are reminiscent of the orbital dips seen in LMXRBs. The sim-

ilarities include the marked irregularity, the preferential occurrence near orbital phase 0.8, and the presence of photoelectric absorption. The dips in LMXRBs are believed to be caused by obscuration of the compact star by material above the disc plane (e.g., Mason 1989). There is currently no accepted explanation for this structure; however, observations indicate that this material subtends elevation angles at the primary of 5–12° in X1822−371 (Hellier & Mason 1989), 8–15° in XBT0748−676 (Parmar et al. 1986), and $> 11°$ in XB1916−053 (Smale et al. 1988).

That similar phenomena can occur in other cataclysmic variables is shown by the LE band data of an observation of the dwarf nova U Gem in outburst (Mason et al. 1988). These dips are again caused by photoelectric absorption and occur prior to inferior conjunction of the secondary. The orbital modulations of U Gem, four intermediate polars, and two LMXRBs are compared in figure 2.12. It is also interesting to compare these results with the X-ray lightcurve of the eclipsing intermediate polar H0253+193 (Kamata, Tawara & Koyama 1991). This shows a quasi-sinusoidal modulation caused by absorption, with minimum intensity near orbital phase 0.4 (0.0 being the eclipse phase), and underlines that the phasing of the X-ray modulations, and features such as the presence of more than one dip per cycle (e.g., in XB1916−053), are not understood. There is, however, increasing evidence for complex accretion flows in compact binaries. For instance, the SW Sex stars show emission line behaviour incompatible with a Keplerian accretion disc, and have absorption events 0.4–0.5 orbital cycles after eclipse of the white dwarf (Thorstensen et al. 1991). It is interesting to note that in FO Aqr and AO Psc the X-ray dips occur when the optical spin-pulse and beat-pulse are in phase. Under the assumption that the beat-pulse is caused by optical reprocessing in non-axisymmetric disc structure (see §1.5.4.2), this result indicates that such material is then at inferior conjunction.

The height that material can attain above the orbital plane in intermediate polars is currently unknown. However, for the obscuration model to explain the modulations seen in these systems the height must be sufficient, given the system

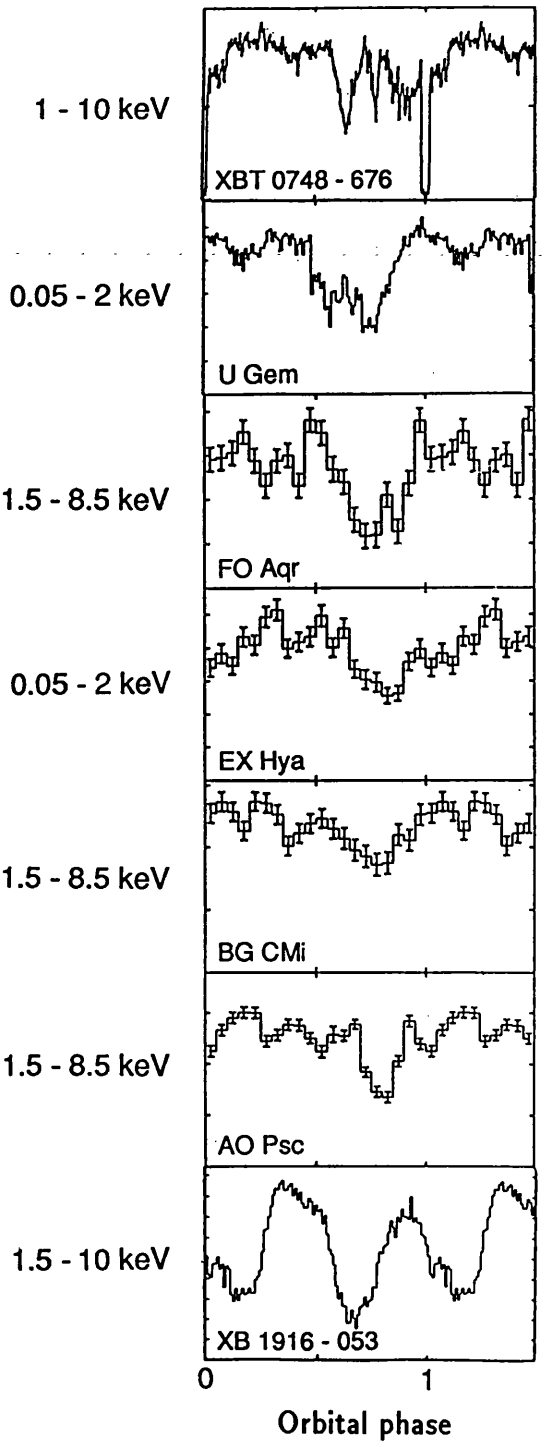

FIGURE 2.12: *X-ray lightcurves of four intermediate polars compared with those of a dwarf nova (U Gem) and two low-mass X-ray binaries (XBT0748−676 and XB1916−053). Where known (upper four panels) orbital phase zero is eclipse; for the lower three panels the phasing is arbitrary. The data are from the ME detector except in EX Hya and U Gem, where the modulation is seen only in the LE band. Data for U Gem, XBT0748−676, and XB1916−053 are taken from Mason et al. (1988), Parmar et al. (1986), and Smale et al. (1988) respectively.*

inclination, for such material to interpose into the line-of-sight to the white dwarf. Of the eight intermediate polars for which adequate orbital coverage in the X-ray band has now been obtained, seven (TV Col, TX Col, BG CMi, EX Hya, FO Aqr, AO Psc, and H0253+193) show secure orbital modulation and one (V1223 Sgr) displays marginal evidence for similar variability. Thus, if the disc obscuration mechanism is indeed the cause, the preponderance of systems showing dips suggests either that the angle which material can attain above the disc plane is large, or that these intermediate polars are predominantly at high inclination. With the small number of systems currently known (~ 12) this could be due to chance or might otherwise indicate a selection effect in favour of high-inclination systems. It is worthwhile noting that four of the above systems show eclipses of either the white dwarf (EX Hya, H0253+193) or of part of the accretion flow (FO Aqr, TV Col)—inclination estimates for the non-eclipsing systems are too imprecise.

So far I have compared the orbital modulations seen in intermediate polars with those in systems which contain accretion discs (e.g., U Gem, LMXRBs). However, the suggestion by Hameury, King & Lasota (1986) that intermediate polars do not accrete through discs offers the potential for alternative mechanisms for orbital modulations. The impact of the stream directly onto the magnetosphere might produce orbitally localised emission regions at the point of impact on the magnetosphere or on the white dwarf's surface. A similar situation in polars produces modulations very different from those seen in intermediate polars, commonly showing periods of zero flux when the emission region is in the hemisphere away from the observer. However, it is possible that the effect of the spinning white dwarf changes the accretion flow sufficiently to produce intermediate polar-type orbital modulations. In particular, the impact of the stream with the magnetosphere could produce a shock region throwing material out of the orbital plane. As suggested by Norton et al. (1992a), obscuration of the X-ray source by such material might produce modulations mimicking those produced by a stream/disc interface.

The geometry of the stream/magnetosphere interaction is currently too un-

certain to enable a comparison with the observations contained in this chapter. Nevertheless there are several points that can be raised concerning such ideas. For instance, in AO Psc the low-energy X-rays are completely spin-pulsed, ruling out additional orbitally related emission regions. The fact that this spin-pulsed emission is extinguished during the dips argues strongly for the dipping (i.e., structured disc) model (Hellier, Cropper & Mason 1991). Similarly, McHardy et al. (1987) have argued that the large dips seen in BG CMi might result from self-obscuration in an emission region situated where the stream hits the magnetosphere. However, the large depth of the dips (50%) and their presence at 4.5–8.5 keV would require that the majority of the hard X-ray emission originates at the magnetosphere, which seems unlikely given that only $\sim 10\%$ of the gravitational energy has been liberated by the time the accreting material has reached this radius. Again though, a similar model with material at the stream/magnetosphere impact obscuring X-rays from the white dwarf might be viable provided BG CMi were at a high inclination.

A simple absorption model for the orbital dips cannot, in itself, explain the changes in spin pulse-fraction during the dips seen in FO Aqr, TX Col, and BG CMi. However, all three systems have shown X-ray modulation at beat periods, which will interfere with the spin-pulses and might account for the apparent changes in the spin-folded profiles. Such sidebands are incompatible with simple discal accretion and imply a more complex scenario in which at least part of the accretion flow retains a memory of orbital phase when it encounters the magnetosphere. In such a hybrid disc-fed/discless accretion model the contribution of each mode can be deduced from the relative strengths of the spin-pulse and the beat-pulse (Hellier 1991, 1992; Wynn & King 1992; NMLW).

2.4.2 THE QUASI-PERIODICITY IN GK PERSEI

Whether or not the X-rays from GK Per are orbitally modulated is not known, owing to the long binary period. However, the quasi-periodic variations in the

X-ray lightcurves and their associated hardness ratios (see figures 2.10 and 2.11), especially during the second and third observations, are remarkably similar to the *orbital* modulations previously discussed—in the third observation, the hardness ratio might almost be a mirror-image of the count-rate timeseries. This is firm evidence that photoelectric absorption also contributes to the quasi-periodic variability in GK Per.

The indications are, therefore, that the variability in GK Per may be caused by mechanisms similar to those operating in LMXRBs and perhaps in other intermediate polars. Further evidence in support of this is lent by the observation that the spin pulse-fraction is unaffected by the aperiodic variations (Watson, King & Osborne 1985). However, the obscuration does not recur on the orbital cycle, but at a range of 'periods' greater than about 0.5 hr. Thus, the obscuration may be caused by the passage, in a disc, of a transient bulge across the line-of-sight to the white dwarf. It should be noted that if GK Per is driven by Roche lobe overflow, then the presence of an accretion disc is essentially incontestable, as the specific angular momentum of any material at the inner Lagrangian point is such that its natural Keplerian circle would have a radius which is larger (a factor of a few) than the magnetospheric radius of a typical intermediate polar primary. Under the assumption that the disc bulge orbits the white dwarf at the local Keplerian velocity, the observed timescale of the variability implies that this material must lie at a distance $\sim(2.2\text{–}3.5)\times10^{10}\,M^{1/3}$ cm from the primary ($\sim 3\text{–}5r_c$, where M is the ~~Solar~~ mass, and r_c is the corotation radius, where the Keplerian speed of the disc material equals the rotation speed of the white dwarf).

Of course, the above scenario requires, as is the case for the previous systems, that GK Per is at a high inclination. It is therefore interesting that, according to the accretion disc outburst model recently published by Kim, Wheeler & Mineshige (1992, hereafter KWM), 'a binary inclination of $\sim 82°$–$86°$... [is] required to fit the observed visual magnitude of the outburst peak'. Moreover, one of the requirements of their model is that the inner disc radius exceeds the corotation radius by a factor

of four, so the expected distance from the white dwarf of the suggested transient bulge(s) is (are) consistent with the inner disc radius derived by KWM.

The requirement that the inner disc radius exceeds r_c by a factor of four is, however, rather severe. Accretion ought not to occur under such circumstances (e.g., Wang 1987; Ghosh & Lamb 1978, 1979a, 1979b; see §3.4.2.1 for a summary of these theories) because of the centrifugal force on the inner disc material which halts radial inflow. Nevertheless, the X-ray emission from GK Per clearly indicates that accretion onto the white dwarf is taking place. Ghosh & Lamb (1979a) did speculate, however, that unsteady accretion might occur provided the ratio of the rotation rate of the white dwarf to that of the material in the inner disc were not *too* large ($\omega_s \not\gg \omega_{max}$). In GK Per this ratio is approximately 5–11, assuming the inner disc radius of KWM. The outcome of the unstable accretion which might arise in this scenario has, as far as I am aware, not been examined, and is beyond the scope of this thesis. Thus, I am currently unable to comment on the validity of the implicit assumption that this scenario might produce transient structures at or near the inner disc edge. In chapter 5, I show evidence which suggests that bulges may be orbiting at the corotation radius in this system.

A final point concerns the *decrease* in hardness which is occasionally observed to accompany the dips in the lightcurves (figure 2.11). This suggests that hard X-rays are primarily being obscured, whereas softer X-rays are not. This, in turn, implies that the soft and hard X-ray emission regions are either spatially separated, have differing sizes, or both. As the timescale of the variability in all lightcurves is similar, the variations in all cases may be caused by the same obscuring cloud structures. It is not understood how such a cloud of gas might show the characteristic signature of photoelectric absorption at some times, but not at others. It may be possible to reproduce the above observed behaviour if the harder X-ray emission region is small and surrounded by a larger, softer X-ray emission site, so that the hard X-ray region is completely obscured (by an optically thick gas) whilst a substantial fraction of the softer X-ray region is not. Turbulence and variations

in the opacity of the obscuring gas could then be invoked to explain the observation that the hardness ratio is also seen, at other times, to vary in antiphase with the lightcurve variation.

2.5 Summary of conclusions

I have presented evidence that the orbital modulations in many intermediate polars are similar to those seen in dipping LMXRBs and may, therefore, be caused by obscuration of the X-rays from the white dwarf. The absorption could be due to accretion disc structure raised by the impact of the stream, as is thought to occur in LMXRBs. Alternatively, in a discless accretor, the analogous impact of the stream with the magnetosphere might also produce vertical structure and hence similar modulations. As obscuration of the white dwarf is most likely in highly inclined systems, the preponderance of X-ray orbital modulations in intermediate polars suggests that they are indeed predominantly at high inclination. Clearly, this is true in the eclipsing systems EX Hya, TV Col, FO Aqr, and H0253+193, and in chapter 5 I argue that GK Per (which shows similar X-ray absorption features) might indeed be at a high inclination as well (§5.4.2).

ADDENDUM 2

1. On page 56, after the last sentence, add: 'This is in contrast to the X-ray spin- and beat-pulses, which are antiphased at X-ray orbital minimum.'

3. SPIN-UP IN BG CANIS MINORIS: A CUBIC EPHEMERIS?

One day on my yacht,
A plague I have caught,
To discover P-dot.

In time it did seem
It would take a great team
To unravel the crazes
Of cycles and phases.

'Gainst this I have fought,
Lest it all come to nought,
Now I've got a P-dot,
But hardly a thought,
For my brain's turned to rot.

Joseph Patterson
In Accretion-Powered Compact Binaries (1990)

3.1 INTRODUCTION

This chapter details the analysis and interpretation of optical CCD photometry of the intermediate polar BG CMi. This system has become the subject of debate since the suggestion of Norton et al. (1992b, hereafter NMLW) that the white dwarf's spin period may be 847 s, not, as inferred by McHardy et al. (1982, 1984, 1987), 913 s. An 847 s period has not been seen in photometry of this system, and the present data, as will be seen, do not contain this period either. The main concern here, however, is the 913 s pulsation ephemeris. It became apparent during the

following analysis that the 913 s pulsation ephemeris of Augusteijn, van Paradijs & Schwarz (1991, hereafter APS) was inconsistent with these new data (and with the spectroscopy presented in chapter 4), so a revision was undertaken. Although a more recent ephemeris has now been published (Patterson & Thomas 1993, hereafter PT), I have nevertheless revised the quadratic ephemeris by combining all previously published arrival times (including those of PT) with three new timings derived here. Following suggestions that a cubic ephemeris might provide a better description of the arrival times (T. Augusteijn, private communication), as is the case in FO Aqr (Osborne & Mukai 1989), I have also derived a cubic fit.

3.2 OBSERVATIONS

3.2.1 ACQUIRING THE DATA

The photometry (Johnson *BVR*) was obtained on 1992 January 3 at El Observatorio Astrofísica del Roque de los Muchachos on La Palma using the CCD camera on the Jacobus Kapteyn Telescope (JKT). To adequately cover the 913 s periodicity in this system, high time resolution was required (~ 60 s). Therefore, to reduce losses arising from filter changes, the observations were carried out contiguously in each filter rather than switching filters between single integrations, and readout times were minimised by windowing the chip (GEC P8603) such that only $\sim 17\%$ of its area was used.

The object field containing BG CMi and two brighter field stars (for use as comparisons) was observed first using the *B* filter for a duration of ~ 2.5 hr, then with the *R* filter for ~ 2.0 hr, and then with the *V* filter for ~ 1.1 hr (approximately ten, eight, and four 913 s cycles respectively). The on-source integration time per frame was 45 s for all three filters (except for the first 14 frames in the *B* band, where an experimental integration time of 30 s was used), giving an effective time resolution of ~ 90 s.

Throughout the observing run, regular observations of several standard stars

Date	Start time (UT)	Integration time (s)	Filter (Johnson)	Target
1992 January 2	19:19	10	*B*	2Z524
	19:24	10	*V*	2Z524
	19:27	10	*R*	2Z524
	21:55	10	*V*	2Z524
	23:35	30	*B*	BG CMi
	23:57	45	*B*	BG CMi
1992 January 3	02:12	45	*R*	BG CMi
	04:09	5	*R*	99Z408
	04:11	5	*V*	99Z408
	04:14	5	*B*	99Z408
	05:18	45	*V*	BG CMi
	06:34	10	*V*	100340

TABLE 3.1: *Log of photometric observations of standard stars and BG CMi.*

(selected from the JKT control room standard star catalogue) were also obtained for magnitude calibration. In addition, bias frames and sky flatfields were acquired at the start and end of the night. The atmospheric conditions were stable and good throughout all observations (see §3.2.2). Table 3.1 summarises the observations.

3.2.2 OBSERVING CONDITIONS

Two diagnostics have been used to determine the observing conditions. Firstly, I have calculated the seeing as a function of time throughout the run by measuring the mean full-width at half-maximum (in pixels) of the point-spread function of the brightest object in the field using a pixel size of 0.3″. The result is shown in figure 3.1. The best seeing was around 1.7″, typical of December/January on La Palma (Isaac Newton Group Observers' Guide 1988).

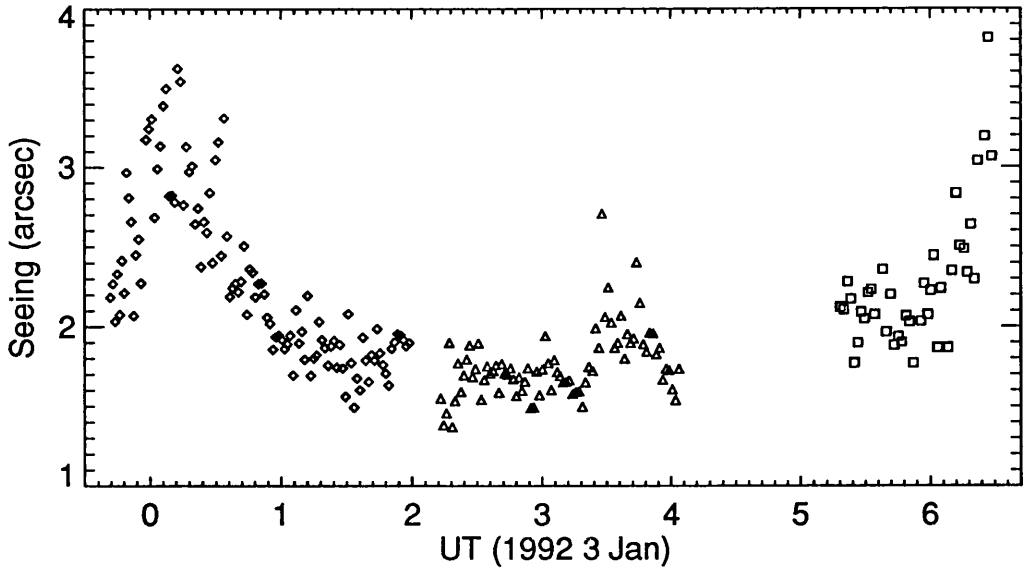

FIGURE 3.1: *Variation in seeing as a function of time. The diamonds represent the B band observations, the triangles the R band, and the squares the V band. The U-shaped trend is caused by the field rising and then setting in the sky.*

Secondly, I have fitted quadratic curves to each of the comparison star counts datasets and determined the r.m.s. residual of the counts about the best fit. A quadratic curve is necessary due to the effects of changing airmass. For both comparison stars in all three bands this residual is less than 2% of the mean count-rate (1.9% in B, 1.7% in R, and 1.5% in V). Both the measurement of the seeing and the scatter of the raw counts indicate photometric conditions.

Figure 3.2 shows the raw lightcurves (count s^{-1}) of BG CMi and the brightest of the two comparison stars. There are four points in the V band observation—marked as A, B, C, and D—which are situated away from the trend of the rest of the data. At these points the telescope skipped suddenly through distances of, typically, 14″, creating a double image of each source on the CCD. In these cases the relocated image of BG CMi was partially outside the CCD frame. Thus, the count-rate for BG CMi in all four of these frames could not be accurately determined, and they have been removed from the remainder of this analysis. The reason for this telescope behavior is not known.

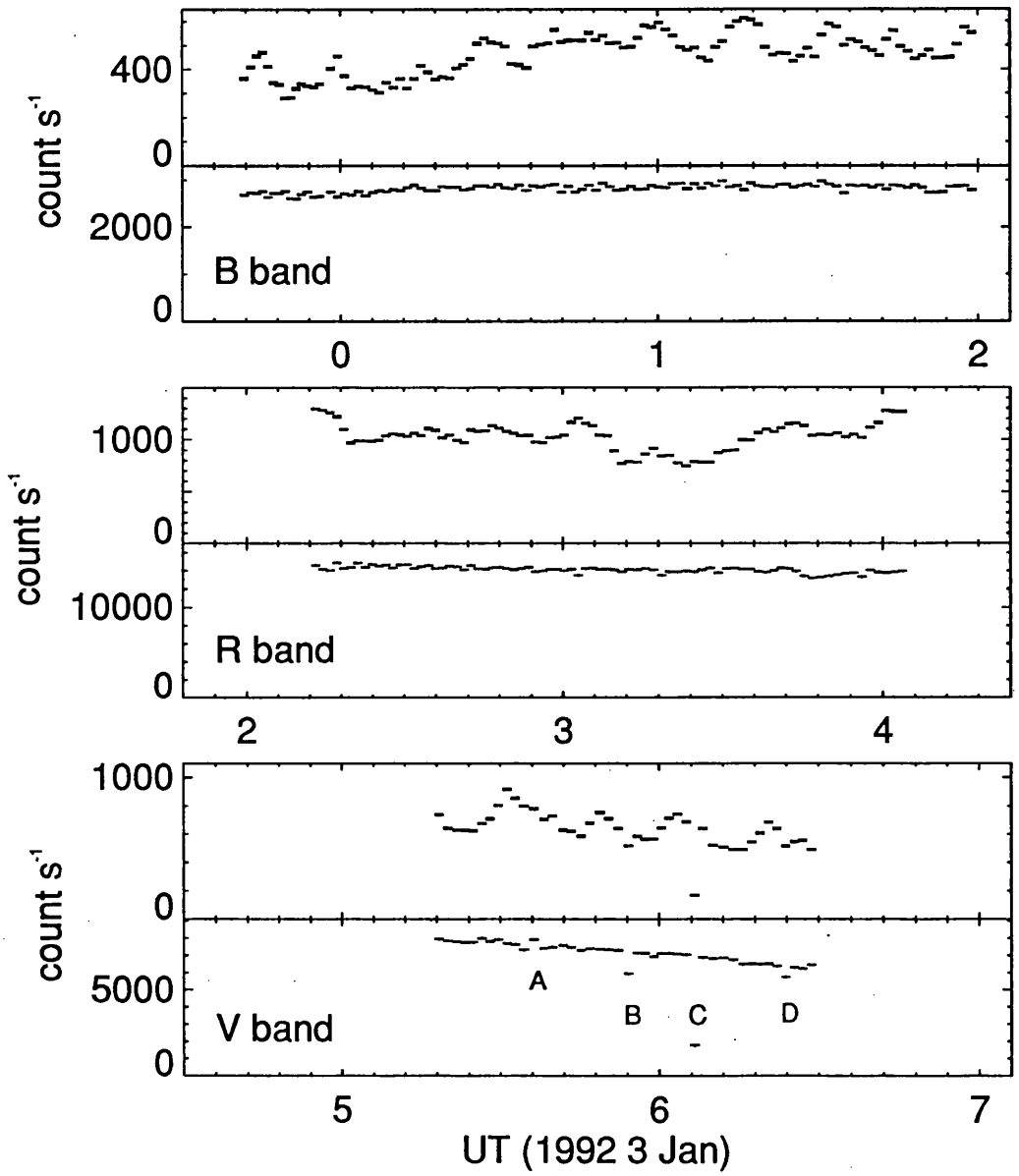

FIGURE 3.2: *Raw lightcurves showing the variation of BG CMi (top panels in each block) and the brightest of the two comparison stars as a function of time. The typical error is less than 1.0%. At A, B, C, and D the telescope moved suddenly (for reasons unknown) creating a double image of each source on these CCD frames. See §3.2.2 for further discussion.*

3.3 DATA ANALYSIS

3.3.1 MAGNITUDES

The V band atmospheric extinction coefficient is calculated, using the method outlined in §A.3.2, as $k_v = 0.23 \pm 0.01\,\mathrm{mag\,airmass^{-1}}$, a value typical of 1992 January as a whole, according to measurements made by the Carlsberg Automatic Meridian Circle (D. Jones, private communication). The coefficients in B and R, however, could not be reliably measured using this method because these data do not cover a large enough range of airmass (0.20 and 0.16 airmasses in B and R respectively, compared to 1.11 in V). Nevertheless, as explained in §A.3.2, it is possible to infer values for k_B and k_R if one assumes that the extinction is grey. Under this assumption, changes in k_V do not alter the coefficients in the colours $B-V$ and $V-R$, thus $k_B - k_V$ and $k_V - k_R$ are constant. The coefficients in B and in R for the night of 1992 January 3 are $k_B = 0.34 \pm 0.01\,\mathrm{mag\,airmass^{-1}}$ and $k_R = 0.16 \pm 0.01\,\mathrm{mag\,airmass^{-1}}$, using the relations A.4 and A.5.

To calculate the magnitude of the comparison stars, three standard star observations were obtained in the V band, and two were obtained in each of the bands B and R. After correcting the count-rates measured for the standard stars and the comparison stars to the values expected above the atmosphere, I calculated the magnitude of the comparison stars using the method discussed in §A.3.2. This yields one estimate of the magnitude of each comparison star for each standard star in each band. The results are given in table 3.2. The final comparison star magnitudes quoted in each band are a mean of the observations with 1σ errors.

As two comparison stars were observed, it was possible to obtain two magnitude estimates of BG CMi in each band. These were found to be in agreement to two decimal places. The mean values are shown in figure 3.3. The orbital phasing for this diagram was calculated according to the orbital ephemeris of PT ($P_{orb} = 0.1347486[\pm 3]\,\mathrm{d}$), with phase zero defined as minimum optical orbital intensity. The B band magnitude variation in this figure (between 14.8 mag and 15.6 mag)

Band	Magnitudes	
	Comparison #1 (Mean)	Comparison #2 (Mean)
B	13.143	13.564
	13.104	13.524
	(13.124 ± 0.028)	(13.544 ± 0.028)
V	12.978	12.455
	12.865	12.342
	12.995	12.472
	(12.946 ± 0.071)	(12.423 ± 0.071)
R	12.068	12.640
	11.982	12.555
	(12.025 ± 0.061)	(12.598 ± 0.060)

TABLE 3.2: *Comparison star magnitudes.*

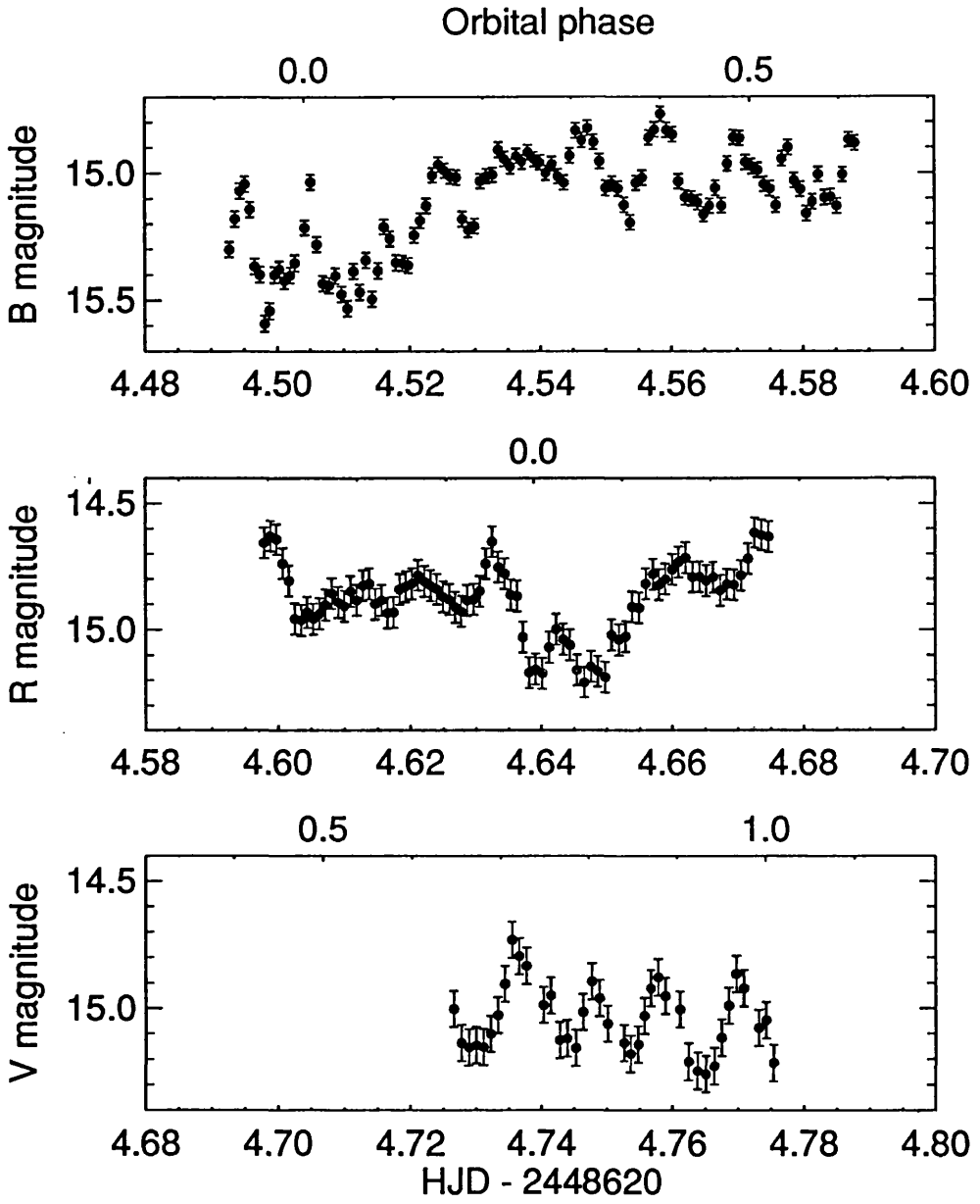

FIGURE 3.3: *Magnitude variation of BG CMi as a function of time (lower axes) and orbital phase (upper axes). Orbital phase has been calculated according to the orbital ephemeris of Patterson & Thomas (1993), with phase zero representing minimum optical intensity.*

compares well with the B band lightcurves given by McHardy et al. (1987; see their figure 6). The average V band magnitude cannot be compared easily with the value reported in the literature (14.5 ± 0.2 mag, McHardy et al. 1984) because the V band lightcurve samples only a small segment taken from orbital minimum intensity. However, under the assumption of an orbital variation in V magnitude of similar amplitude to that observed in the B band, the mean value is probably near 14.8 mag. An R band magnitude has not been directly published, but PT reported $V - R = +0.1$, comparable to the present data before orbital photometric minimum, although it is not known which system (Johnson or Cousins) the colours of PT refer to.

3.3.2 Periodicities and their amplitudes

The lightcurves displayed in figure 3.3 are typical of intermediate polars, showing the orbital modulation (most obvious in the B band data) and a pulsational modulation generated by the rotation of the white dwarf. The latter is less obvious in the R band, having a lower amplitude there. Although the photometry was not obtained simultaneously in each filter, the same orbital phase range is covered by the R band data as by the data from the B band. Moreover, the R band data were acquired after B but before V, so the decrease in amplitude of the pulsational modulation in the R band is not a result of poor observing conditions.

Previous authors have assumed a 913 s spin period for BG CMi (e.g., McHardy et al. 1982, 1984, 1987). However, a recent *Ginga* observation reported by NMLW has thrown some doubt on the assumed spin period of the white dwarf in this system. These latter authors find evidence for an 847 s period in their data and argue that this is the true rotation period, and that the 913 s period is caused by beating between the orbital period and the new rotation period ($1/P_{913} = 1/P_{847} - 1/P_{orb}$). Therefore, to search for possible evidence of an 847 s period in the current data I have perfomed a Fourier power spectrum analysis. In order to reduce unwanted low-frequency peaks in the power spectrum I first removed any

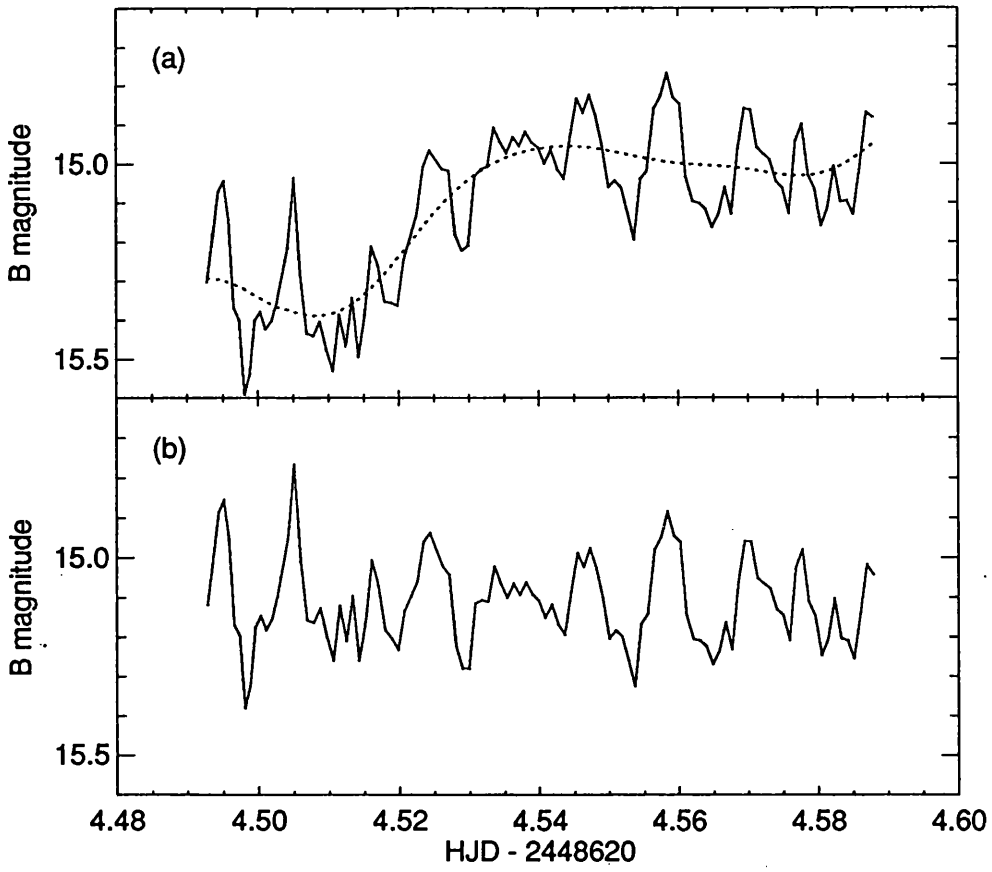

FIGURE 3.4: *(a) The removal of the slow orbital trend from a typical lightcurve (in this case, B band) by smoothing and subsequent subtraction of the smooth curve. (b) The resultant dataset.*

orbital trend from the data prior to this analysis. A smoothing algorithm was employed to remove short-period oscillations from the data using a Fast Fourier Transform as a low-pass filter (Press et al. 1989). The resultant smoothed dataset, approximating the slow orbital trend, was then subtracted from the original data. This procedure, demonstrated in figure 3.4, was adopted by Osborne & Mukai (1989) for removing trends from their photometry of FO Aqr.

The Fourier power spectra of the resultant datasets are shown by the thin traces in figure 3.5. These power spectra show that the dominant periodicity in each dataset is consistent with the known 913 s period. Gaussian fits to the strongest peaks in each band yield periods of 925 ± 36 s in B, 980 ± 80 s in V, and 940 ± 65 s

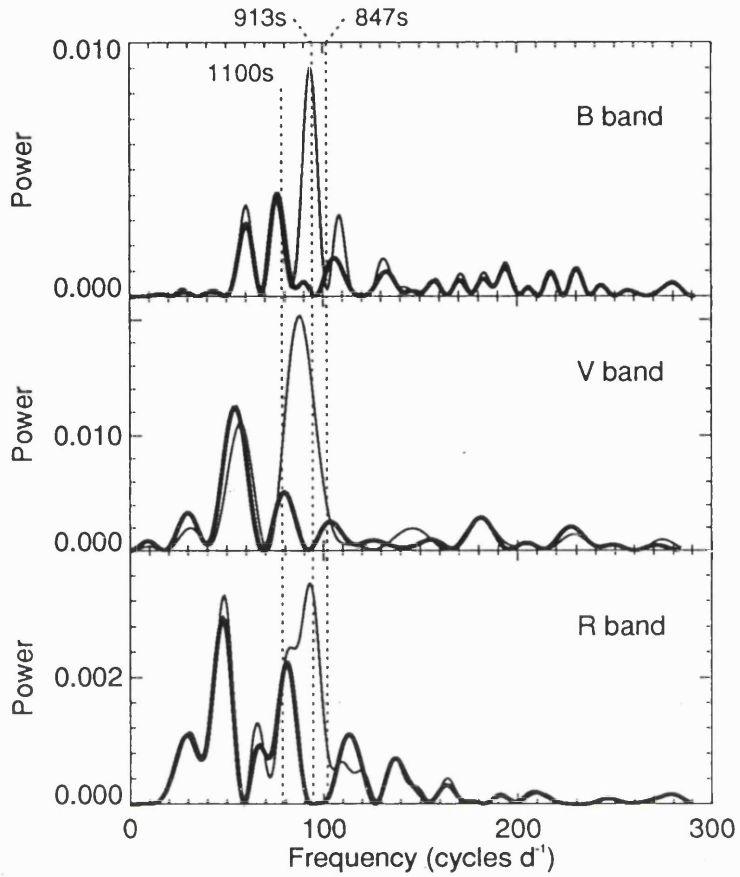

FIGURE 3.5: *Fourier power spectra of CCD photometry. The thin line shows the spectrum of the data obtained after the orbital trend has been removed. The thick line shows the trace obtained after a 913 s sinewave has also been subtracted.*

in R, using the half-width at half-maximum as an estimate of the uncertainty. There are several peaks in the Fourier spectra, however, which cannot be explained as harmonic frequencies, or by the window function, and which are not due to aliasing or beating. Some of these frequencies are caused by random flickering in the data, and have been amplified because of the short duration of these datasets. For example, the R band data contains two broad flares near Heliocentric Julian Dates (HJD) 2448624.60 and 2448624.63 (see figure 3.3), giving rise to the large peak observed near $F = 50\,\mathrm{d}^{-1}$ in the Fourier spectrum. However, a period of $\sim 1100\,\mathrm{s}$ in the B and R bands may be intrinsic to the source, for a similar period

has been detected by Augusteijn in optical photometry (private communication) and is also strongly observed in the emission lines of this system (see chapter 4).

The Fourier spectra do not exhibit any significant power at a period of 847 s. However, given the sampling rates of the datasets (once every 90 s) and their brevity, the 913 s and 847 s periods would not be resolved in these power spectra even if the 847 s variability *were* present. Instead one would observe a single asymmetric peak centred at some point between the required two frequencies. With the possible exception of the V band (which is the shortest dataset anyway), none of the 913 s peaks in the Fourier spectra exhibit excess high-frequency power. In fact, the 913 s peak is displaced slightly towards the *lower* frequencies in all three cases. These considerations indicate that the 847 s period is probably not present in these data.

To further investigate the possibility of an 847 s period in these data, I subtracted, from each lightcurve, a sinewave representing the 913 s periodicity, and repeated the Fourier analysis. To calculate the sinewave parameters each dataset was folded according to the quadratic ephemeris of PT ($P_{913} = 0.01057298[\pm 1]$ d) and rebinned into ten phase bins. This ephemeris has maximum intensity at phase zero. These data were then fitted, using a weighted least-squares method, with a sinusoidal function of the form

$$y = c + a \sin\left(2\pi[x - \phi]\right), \tag{3.1}$$

where x is the phase of the folded data and c, a, and ϕ are the mean offset, semi-amplitude and phase of the fitted sinusoid, respectively. Figure 3.6 shows the folded data along with the best-fitting sinusoids.

The Fourier spectra obtained from the new, de-pulsed datasets are shown as the thick lines in figure 3.5. There *is* non-zero power at the frequency corresponding to 847 s in both the V and R bands, but it is not significant compared to the level of noise. I have therefore determined upper-limits for the full amplitude of a modulation at this period, in each band, by adding sinusoidal tracers of varying amplitude to each of the original datasets (i.e., before subtracting the 913 s periodicity) and

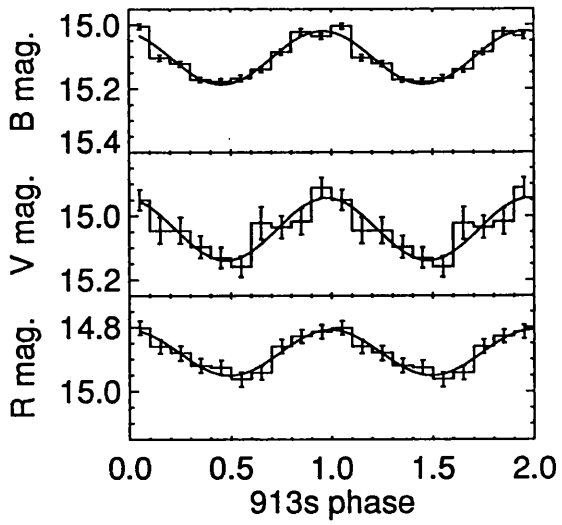

FIGURE 3.6: *The de-trended data folded on the 913s period using the ephemeris of Patterson & Thomas (1993). Maximum intensity is at phase zero. Two cycles are shown for clarity.*

observing at which amplitude the corresponding peak in the power spectrum is comparable to the power seen at the 847 s period. The derived full-amplitude upper-limits for an 847 s modulation are 0.07 mag in B and in V, and 0.06 mag in R. These are to be compared with the amplitudes of the 913 s modulation, given in table 3.3, which are typically a factor of 2–3 larger.

3.3.3 WHITE DWARF ROTATION EPHEMERIDES

When this analysis was begun, it became apparent that the pulse maxima arrival times in these data were inconsistent with those expected according to the two most recent ephemerides available at that time (APS; Singh et al. 1991, hereafter S91). I thus calculated a new quadratic ephemeris. During this calculation, however, a more recent ephemeris for the 913 s pulsation was published (PT), which is in excellent agreement with the current data (see figure 3.6). Their publication contains seven new pulse arrival times, two of which are more recent than the epoch of the current observations (1992 January 3). I therefore recalculated the

Filter	Mean magnitude	Full amplitude	
		Magnitudes	% of mean
B	15.110 ± 0.002	0.185 ± 0.005	1.23 ± 0.05
V	15.031 ± 0.011	0.244 ± 0.032	1.62 ± 0.22
R	14.884 ± 0.007	0.114 ± 0.019	0.77 ± 0.13

TABLE 3.3: *Mean magnitudes and full amplitudes of the 913 s modulation.*

quadratic ephemeris by combining all previous published pulse timings with new timings derived here (see §3.3.3.1). I have also derived a cubic ephemeris, following suggestions by Augusteijn (private communication) that such a result might be better suited for BG CMi.

3.3.3.1 Pulse arrival times

The published arrival times for maximum optical intensity of the 913 s pulsation used in the derivation of these ephemerides are those given in PT[1], APS, and S91. Some of the timings given in PT (all except the last seven) were originally given in table 2 of Patterson (1990). All were determined from blue, ultraviolet, and white light photometry. The timings of APS were calculated from Walraven V, B, L, U, and W photometry, and the S91 arrival times were determined from Johnson B and U photometry. It should be pointed out that the variability in BG CMi is a broadband feature, and thus dependence of the pulse arrival times on colour is not expected (e.g., Patterson 1990). Figure 3.6 indeed shows that the pulses in each dataset occur in phase.

In addition to published data, I obtained three new arrival times, representing

[1]Henceforth, when I mention the timings of PT, I refer only to their own data, and exclude the arrival times of S91 and APS which are also listed in table 2 of PT.

epochs from each of the three (*BVR*) datasets discussed here. To calculate these timings the data with only the orbital trend removed were folded and rebinned on a period of 0.01057298 d (PT) with phase zero taken as the epoch at the start of each dataset, having applied the Heliocentric correction. By fitting sinusoids to these folded data and obtaining the phase of maximum light, the arrival times could be calculated by adding or subtracting the appropriate fraction of the cycle to the original folding epoch. The period used for folding the data was found not to appreciably affect the results of this analysis: although I have consistently used a period of 0.01057298 d, the folds are indistinguishable from those obtained when using periods in the range 0.01057260–0.01057300 d, covering all previously published values of the pulsation period.

Pulse timings over a ten-year baseline have resulted in a period of sufficient accuracy that cycle count ambiguities for the new arrival times were not encountered. The arrival times and cycle counts for the new and previously published data are presented in table 3.4. Note that the timings in PT are given only to four decimal places, whereas all other authors list their timings to five places. I have adopted the same practice for the uncertainties.

3.3.3.2 Determining the errors on the arrival times

Many different methods for calculating the uncertainty associated with a particular arrival time, or a set of arrival times, have appeared in the literature. The method used here for the new timings is similar to that used in APS (hereafter referred to as 'method A'). First the data were folded, binned into ten phase bins and fitted with a sinusoidal function of the form given by 3.1. Now labeling the error on the fit as Δy (the 'dispersion' of the data about the best fit, i.e., the standard deviation of y about y_{fit} divided by the square root of the number of data points), the corresponding uncertainty in x may be understood as that value Δx such that

$$y - \Delta y = c + a \sin\left(2\pi[x \pm \Delta x - \phi]\right). \tag{3.2}$$

Cycle count	Arrival time (HJD)	Error (d)	Reference
0	2445020.28194	0.00050	2
25977	2445294.9340	0.0007	4
35876	2445399.59637	0.00030	1
36163	2445402.63141	0.00038	1
36251	2445403.56216	0.00034	1
36263	2445403.6872	0.0007	4
36535	2445406.56395	0.00034	1
36630	2445407.56855	0.00030	1
36833	2445409.7145	0.0007	4
36913	2445410.56085	0.00033	1
37007	2445411.55513	0.00035	1
41746	2445461.6594	0.0007	4
56147	2445613.9207	0.0007	4
56533	2445618.0012	0.0007	4
64700	2445704.35072	0.00050	3
67140	2445730.14857	0.00078	5
95060	2446025.34581	0.00078	5
97612	2446052.32583	0.00078	5
103791	2446117.65659	0.00036	1
103978	2446119.63349	0.00028	1
104169	2446121.65288	0.00032	1
104357	2446123.64096	0.00034	1
129078	2446385.0131	0.0007	4
131234	2446407.80852	0.00032	1
131326	2446408.78182	0.00029	1
131425	2446409.82827	0.00045	1
168356	2446800.29545	0.00078	5

TABLE 3.4: *Arrival times and cycle counts for the 913 s pulsation.*

Cycle count	Arrival time (HJD)	Error (d)	Reference
198766	2447121.81586	0.00044	1
198952	2447123.78238	0.00034	1
199802	2447132.76944	0.00036	1
201028	2447145.73206	0.00038	1
201693	2447152.76299	0.00033	1
204016	2447177.32414	0.00078	3
204293	2447180.25220	0.00078	3
207737	2447216.6653	0.0007	4
207932	2447218.7266	0.0007	4
208112	2447220.6301	0.0007	4
215681	2447300.6550	0.0007	4
215777	2447301.6704	0.0007	4
230264	2447454.83889	0.00041	1
230359	2447455.84340	0.00047	1
230454	2447456.84895	0.00074	1
232262	2447475.9636	0.0007	4
232343	2447476.8202	0.0007	4
232641	2447479.9717	0.0007	4
234227	2447496.73927	0.00033	1
232829	2447481.9580	0.0007	4
235550	2447510.72758	0.00043	1
238255	2447539.32610	0.00078	3
240276	2447560.6950	0.0007	4
240363	2447561.6142	0.0007	4
240612	2447564.24568	0.00078	3
241046	2447568.8347	0.0007	4
241142	2447569.8503	0.0007	4

TABLE 3.4: *(Continued).*

Cycle count	Arrival time (HJD)	Error (d)	Reference
241876	2447577.61117	0.00074	1
243579	2447595.61701	0.00040	1
243676	2447596.64205	0.00056	1
247260	2447634.53382	0.00058	1
247354	2447635.52864	0.00046	1
262152	2447791.9866	0.0007	4
262249	2447793.0108	0.0007	4
262344	2447794.0145	0.0007	4
262439	2447795.0200	0.0007	4
266024	2447832.9229	0.0007	4
266219	2447834.9842	0.0007	4
266595	2447838.9591	0.0007	4
269048	2447864.8948	0.0007	4
274062	2447917.9065	0.0007	4
276881	2447947.7115	0.0007	4
284915	2448032.6510	0.0007	4
302145	2448214.8206	0.0007	4
307439	2448270.7952	0.0007	4
340893	2448624.49419	0.00058	6
340903	2448624.60058	0.00061	6
340915	2448624.72669	0.00075	6
344398	2448661.5522	0.0007	4
344494	2448662.5669	0.0007	4

References for this table:

[1] Augusteijn, van Paradijs & Schwarz (1991); [2] McHardy et al. (1984); [3] McHardy et al. (1987); [4] Patterson & Thomas (1993); [5] Singh et al. (1991); [6] Present work (1992).

TABLE 3.4: *(Continued).*

In other words, if x is altered by an amount Δx, the intensity, y_{fit}, of the sinewave evaluated at $x \pm \Delta x$ is assumed not to lie outside the range $y \pm \Delta y$. Differentiating both sides, setting dy/dx equal to zero, and solving for Δx gives

$$\Delta x = \mp \frac{1}{2\pi} \arcsin\left(1 - \frac{\Delta y}{a}\right) - \frac{1}{4}. \tag{3.3}$$

Multiplying this phase error by the period used to fold the data yields an estimate for the uncertainty on the arrival time, ΔT_{max}. The uncertainties calculated for the three new arrival times using this method are ± 0.00058 d, ± 0.00075 d, and ± 0.00061 d for the B, V, and R bands respectively. These errors are comparable to those tabulated in APS.

As PT and S91 did not publish uncertainties in their arrival times, and as method A cannot be used to derive these, I have determined them using a different procedure ('method B'), as follows. For each of these authors' set of timings, the $O - C$ values were first calculated relative to a linear 913 s ephemeris ($2445020.28194 + 0.0105728772\,N$). The errors on these $O - C$ values were then set equal to unity, the $O - C$ values fitted with a quadratic curve, and the reduced chi-squared (χ^2_ν) for the fit calculated. Finally, the scatter on the $O - C$ values and, therefore, the arrival times for that dataset, were approximated by $\sqrt{\chi^2_\nu}$. For the data of PT an uncertainty of 0.0007 d is calculated. The error on the arrival times in S91 is 0.00078 d.

McHardy et al. (1984, 1987) did not publish individual arrival times for their data, but instead quoted single epochs of maxima in each of these papers. In McHardy et al. (1984) the authors published extensive photometry taken over three months and derived a linear ephemeris for their data. No error on their epoch of maximum (HJD 2445020.28194) was given. In McHardy et al. (1987) the authors published a further epoch of maximum (HJD 2445704.35072) and quoted an error of 0.00009 d without explaining how this was determined. The data in this latter publication span 5.5 hr, which is of the same duration, typically, as the individual runs published by PT, S91, and APS. Therefore, as the quoted error of 0.00009 d is almost an order of magnitude less than the uncertainties given in

APS and those which I have calculated for the data of PT and S91, it is likely that this uncertainty is an underestimate. Errors on the two McHardy epochs cannot be determined using either method A or B, so these epochs have been assigned notional errors of 0.00050 d, typical of the rest.

To investigate systematic differences between the two methods outlined above, I have calculated the typical error on the arrival times in APS using method B and compared this with their own values, which were obtained using method A. The errors quoted in APS occupy the range 0.00030–0.00074 d with a mean of 0.00043 d. The scatter which I calculate for their data is 0.00040 d. These two methods are therefore judged to be in good agreement.

3.3.3.3 Ephemerides

The $O - C$ values were calculated according to

$$O - C = HJD_{max} - (T_0 + P_0 N), \tag{3.4}$$

where HJD_{max} is the *observed* time of maximum, P_0 is an initial estimate for the period, T_0 is the first epoch of maximum in the dataset (HJD 2445020.28194), and N is the number of cycles elapsed since this epoch. The initial period estimate may be chosen arbitrarily. The value used here is that quoted in the ephemeris of APS, 0.0105728772 d. The method employed in calculating the ephemerides is the same as was used in S91, and may be summarised as follows. If the required quadratic ephemeris is considered as the sum of the original linear ephemeris and a quadratic 'correction' function, that is

$$HJD_{max} = T_0 + NP_0 + (\delta T + N\delta P + N^2 P\dot{P}/2), \tag{3.5}$$

or

$$HJD_{max} - (T_0 + NP_0) = \delta T + N\delta P + N^2 P\dot{P}/2, \tag{3.6}$$

then the left side of equation 3.6 is simply the formula for $O - C$ quoted in equation 3.4. Thus, if the $O-C$ values are fit, using χ^2 minimisation, with the parabolic

function

$$O - C = \alpha + N\beta + cN^2, \tag{3.7}$$

then, comparing equations 3.6 and 3.7, one may associate:

$$O - C \equiv HJD_{max} - (T_0 + P_0 N), \tag{3.8}$$

$$\alpha \equiv \delta T, \tag{3.9}$$

$$\beta \equiv \delta P, \tag{3.10}$$

$$c \equiv P\dot{P}/2. \tag{3.11}$$

Strictly, this method is iterative; the new value for the period, $P_0 + \delta P$, was used as a second estimate, and the above method applied again. This was repeated until χ^2_ν became 'stable'.

A similar methodology was employed when fitting a cubic ephemeris. In this case the correction function is a cubic polynomial, so an additional parameter, the coefficient of the N^3 term, enters:

$$d \equiv P^2\ddot{P}/6. \tag{3.12}$$

The best-fit ephemerides and the period derivatives are presented in table 3.5, and the $O-C$ diagram showing both fits can be seen in figure 3.7. The r.m.s. $O-C$ residuals for the quadratic and cubic fits are 0.00069 d and 0.00060 d respectively. As can be seen from the diagram, the cubic ephemeris passes through all three of the new datapoints whereas the quadratic fit does not, indicating that the cubic fit better represents the new arrival times. The χ^2_ν's for the fits are 1.52 (74 degrees of freedom [d.o.f.]) for the quadratic and 0.97 (73 d.o.f.) for the cubic. These formally demonstrate, using an F-test, that the cubic ephemeris is a better fit than the quadratic at a confidence level of 97.3%.

3.3.3.4 Possible contaminations of the arrival times

Warner (1986) and Osborne & Mukai (1989) have warned of the dangers of using data sections shorter than the orbital cycle for determining pulse timings, as the

	Ephemerides (HJD_{max} =)	χ^2_ν (d.o.f.)	Period derivatives
Quadratic:	2448624.49525(±16)	1.52	$\dot{P} = -6.54(\pm 17) \times 10^{-11}$
	$+0.0105727438(\pm 24)\,N$	(74)	
	$-3.46(\pm 07) \times 10^{-13}\,N^2$		
Cubic:	2448624.49430(±25)	0.97	$\dot{P} = -1.60(\pm 76) \times 10^{-11}$
	$+0.0105727120(\pm 64)\,N$	(73)	$\ddot{P} = -9.66(\pm 08) \times 10^{-12}\,\mathrm{yr}^{-1}$
	$-5.89(\pm 41) \times 10^{-13}\,N^2$		
	$-4.93(\pm 76) \times 10^{-19}\,N^3$		

TABLE 3.5: *Best-fit BG CMi rotation ephemerides.*

interaction of the white dwarf's spin period with any sideband(s) might distort the pulse profile sufficiently so as to produce errors in timings as significant as ~ 0.1 cycles. I have therefore followed the analysis of Osborne & Mukai (1989) to investigate this possibility. Briefly, these authors subtracted from their pulse timings the arrival times calculated from their best-fit cubic ephemeris and folded the resultant data on the orbital cycle. The result clearly showed that their pulse arrival times varied quasi-sinusoidally as a function of the orbital period, indicating the presence of two pulsational modulations which interfered constructively at some orbital phase and then destructively half an orbital cycle later (see their figure 4). In contrast, however, no periodic phase shift in the pulse emission around the orbital cycle is observed in BG CMi.

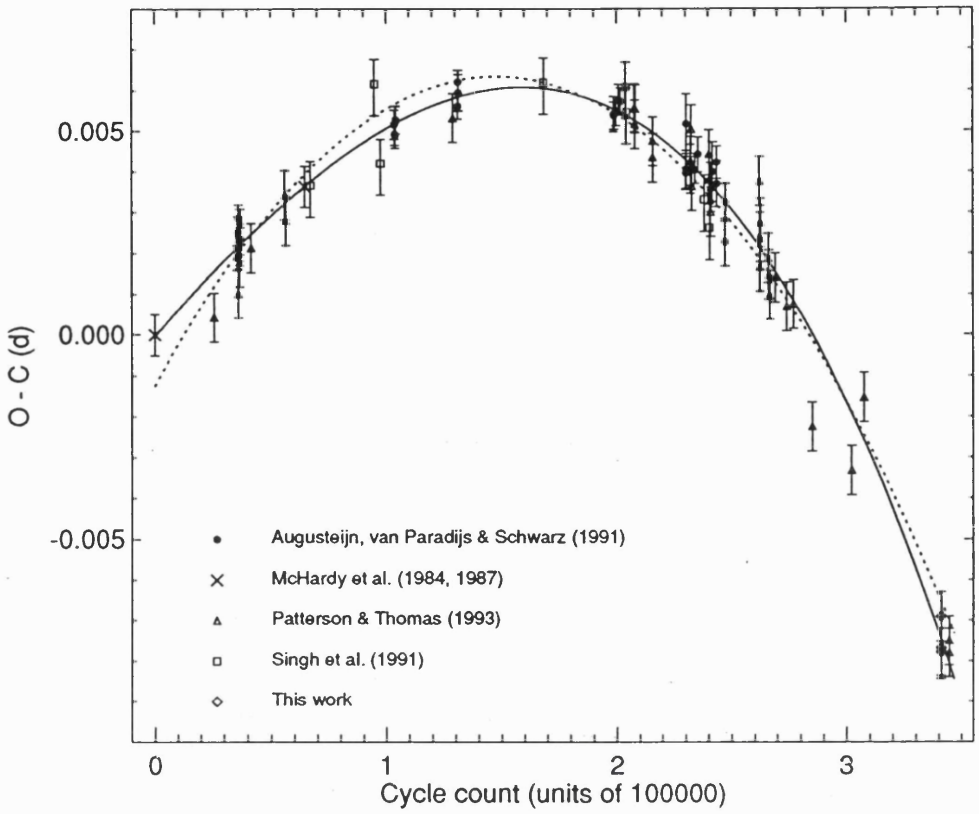

FIGURE 3.7: *Best-fit quadratic (dotted line) and cubic (solid line) ephemerides to published and new arrival times.*

3.4 DISCUSSION

3.4.1 THE AMPLITUDE OF THE 913 S MODULATION

The full amplitude of the 913 s modulation derived from the sine-fitting (see table 3.3) is a factor ~ 2 smaller in the R band (0.114 ± 0.019 mag) than in the V band (0.244 ± 0.032 mag) and, in contrast to the findings of McHardy et al. (1984), the B band modulation amplitude (0.185 ± 0.005 mag) is less than that in the V band. However, irrespective of its formal error, the V band amplitude is not very reliable because the dataset is of too short a duration to average out the contribution from the orbital modulation (in fact, all three datasets give insufficient coverage of the orbital cycle). For example, if the amplitude of the pulse varies throughout

the orbital cycle, then its average amplitude over four pulse cycles will also vary, depending on which part of the orbital cycle these pulsations are sampled from. Therefore, one cannot rule out the possibility that the orbitally averaged amplitude in B may indeed be larger than that in V, consistent with the result of McHardy et al. More photometric observations are needed to clarify this issue.

A wavelength-dependent optical pulsational modulation has been seen previously in intermediate polars other than BG CMi (e.g., AO Psc [van der Woerd, de Kool & van Paradijs 1984], FO Aqr [Chiappetti et al. 1989a], and EX Hya [Siegel et al. 1989]). In all of these cases and in BG CMi the same colour dependence is observed, with the amplitude being lower in the red than in the blue (e.g., a factor ~ 3 lower in AO Psc [van der Woerd, de Kool & van Paradijs 1984] compared to ~ 2 in BG CMi). If the pulsed component is emitted in the accretion column above the stand-off shock near the surface of the white dwarf (e.g., Rosen, Mason & Córdova 1988), then the colour dependence is naturally interpreted as being due to a temperature stratification in the accretion column. Owing to the tapered structure of the column (narrowest at the bottom), the lower regions, where blue light is emitted in preference to red, are more easily obscured by material up-stream as the line-of-sight changes. The cooler, redder regions are more extensive, resulting in a lower pulse-fraction.

An alternative interpretation is possible if an accretion disc is present which has inner regions that are truncated by the strong primary magnetic field. The accretion disc in this case, lacking the hot, innermost regions, would appear redder than if the disc extended down to the surface of the white dwarf. This preferentially dilutes the red pulsation.

3.4.2 IMPLICATIONS OF THE QUADRATIC EPHEMERIS

As the orbital period in cataclysmic variables decreases (see, e.g., Lamb & Melia 1987), the binary becomes more compact and this leads to a decrease in the mass transfer rate, $\dot{M}$, on a timescale $\tau_{\dot{M}} \sim M_s/\dot{M}$ (Rappaport, Verbunt & Joss 1983;

Patterson 1984; King, Frank & Ritter 1985). This diminishing mass transfer rate is expected to cause the angular velocity of the white dwarf (assumed to be rotating in equilibrium with no net torque acting) to decrease on a timescale similar to $\tau_{\dot{M}}$. However, this timescale ($\sim 5 \times 10^8$ yr) is typically three orders of magnitude longer than the period change timescales inferred from observations of intermediate polars (e.g., $P/|\dot{P}| = 4.5 \times 10^5$ yr in BG CMi from the quadratic term). Moreover, the above scenario cannot explain those systems (e.g., EX Hya, BG CMi, and DQ Her) which contain primaries that are clearly in the process of spinning up, not down. The usual interpretation of the observed period changes is that the white dwarf is *not* spinning in equilibrium, but is instead subject to a net torque resulting from the interaction of the white dwarf's magnetic field with the accreting material.

In the rest of this subsection I explore the implications of $\dot{P}$ as measured from the quadratic term. I investigate the case of discal accretion using the general accretion disc torque theory of Ghosh & Lamb (1978, 1979a, 1979b, hereafter GL; see also Ghosh, Lamb & Pethick 1977) and Wang (1987, hereafter W87), and discuss whether the (implicit) assumption of an accretion disc is a valid one. However, I first summarise the accretion disc torque theory.

3.4.2.1 The accretion disc torque theory: a summary

The GL accretion torque theory was originally devised to quantitatively explain the period changes observed in magnetic neutron stars accreting via an axisymmetric disc. However, Lamb & Patterson (1983) showed that by using this theory, period changes in intermediate polars could *also* be accounted for if the compact objects in these systems were white dwarfs rather than neutron stars. The theory has since been used by various authors for this purpose (e.g., Shafter & Macry 1987, Osborne & Mukai 1989, and van Amerongen, Augusteijn & van Paradijs 1987).

According to the GL model, the magnetic field of the white dwarf invades the disc plasma via three principle mechanisms: the Kelvin-Helmholtz (K-H) instability, magnetic field reconnection, and turbulent diffusion. The K-H instability is

driven by the velocity-discontinuity which exists between the low-density magnetic field and the disc. In turbulent diffusion, vertical temperature gradients generate large-scale convection in the disc plasma, enabling the magnetic field to diffuse vertically through the disc. The other important process, reconnection, arises because of the presence of smaller magnetic fields in the disc itself, which are created by differential rotation, convection, and shearing. These fields link with the stellar field at the surfaces of the disc and eventually lead to the disc being threaded. All three processes occur on a timescale shorter than the typical radial drift time of the plasma, enabling the magnetic field to penetrate the disc.

The threading of the disc plasma by the magnetic field creates a broad transition zone in the accretion disc. The inner radius of the transition zone occurs at the Alfvén radius, r_A, where the energy density of the stellar field is comparable to the energy density in the accreting plasma. The outer edge of the transition zone is situated at the so-called 'screening radius', r_s, beyond which the stellar magnetic field is completely screened by currents in the accretion disc, promoting an essentially unperturbed disc flow. The situation is schematised in figure 3.8.

The transition zone is itself divided into two distinct regions. The narrow, inner region, or boundary layer, extends from r_A out to some radius, r_0, where the velocity of material in the disc begins to resemble that of Keplerian rotation. Within this boundary layer, the stellar field is strongly but not completely screened (by a factor of ~ 5) and the plasma at the inside edge of the disc corotates with the star, leaves the disc vertically, and accretes along the stellar field lines. The outer transition region extends from r_0 out to r_s and is immersed in a residual magnetospheric field, with screening of the stellar field due to disc currents becoming more and more important until the magnetic field is entirely screened at r_s.

The net torque on the accreting object is a combination of the (positive) matter torque exerted by the material attaching to magnetic field lines in the boundary region, and the (negative) torque due to the magnetic stress which the twisted stellar magnetic field exerts on the material in the outer transition zone. GL showed

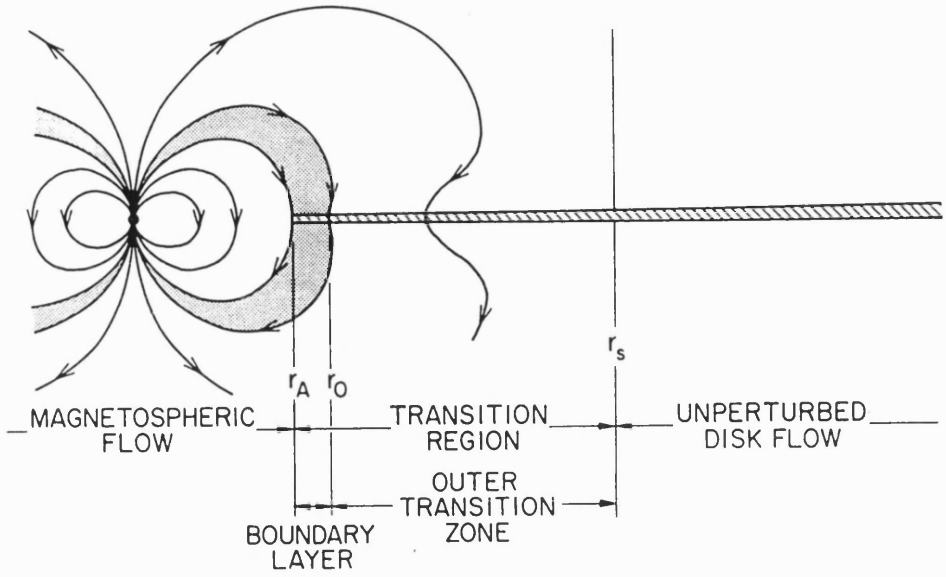

FIGURE 3.8: *A schematic showing Ghosh & Lamb's (1978, 1979a, 1979b) definitions of the inner and outer transition zones in an accretion disc truncated at its inner edge by a strong magnetic field (diagram taken from Ghosh & Lamb 1979b). Refer to the discussion in §3.4.2.1.*

that the total torque on the accreting object may be positive, resulting in spin-up, or negative, leading to a spin-down. The factors which primarily determine the sign of the torque are the rotation period of the white dwarf and the mass accretion rate (luminosity). This is because outside the corotation radius, r_c, where the Keplerian velocity of the disc plasma equals the stellar rotation velocity, the magnetic field lines have a positive pitch (i.e., they are bent in the direction of flow of the disc material), whereas inside this radius the pitch is negative. For sufficiently 'fast' rotators, having rotation velocities comparable to the Keplerian velocity at the inner edge of the disc, or for sufficiently small mass transfer rates, the magnetic coupling between the stellar field and the outer transition zone in the disc exceeds the matter torque and acts to spin the star down. If the rotation is faster still, the combined centrifugal force and magnetic pressure at r_0 exceeds the gravitational attraction, preventing radial inflow, and steady accretion is thought not to occur. For 'slow' rotators the matter torque dominates and the star is spun up. In this

latter regime, under the assumption of steady mass transfer, the angular velocity of the star gradually increases until an equilibrium value is reached at which point the net torque acting on the star vanishes.

The torque itself is parameterised in the GL theory by the dimensionless torque function, $n(\omega_s)$, where ω_s—the 'fastness parameter'—is the ratio of the stellar angular velocity to the Keplerian angular velocity at the outer edge of the boundary layer, at radius r_0. However, GL's dimensionless torque is not well known. It has a value ~ 1.4 when $\omega_s \ll 1$, is zero when the star is spinning in equilibrium ($\omega_s \simeq 0.8$–0.9), and is negative in the regime of 'fast' rotation ($\omega_s \sim 1$). As already mentioned, stable accretion may not occur for $\omega_s > 1$.

According to W87, GL's treatment of the accretion torque is subject to some physical difficulty. He pointed out that the magnetic pitch on the surface of the disc in GL's theory is too large, which implies that the toroidal component of the magnetic field is so great that the resulting magnetic stress ought to exceed the thermal pressure of the disc plasma at the corotation radius and cause the disc to break up. This problem has been noted previously by other authors (e.g., Shafter & Macry 1987, Osborne & Mukai 1989). Initially, GL calculated the value of ω_s at which the star spins in equilibrium as 0.35. However, they later suggested that the value of ω_s stated above (0.8–0.9) would be more reasonable for equilibrium rotation (see Shafter & Macry 1987 and references therein), but no revision of their theory was given.

W87 has assessed this problem and derived a more recent estimate for the dimensionless torque. In the following calculations I adopt this new formulation to derive crude estimates of the mass accretion rate in BG CMi, the white dwarf mass, and the white dwarf magnetic moment, using the measured values of the spin period, P, its rate of change, $\dot{P}$, and the magnetic field strength, B (from Chanmugam et al. 1990).

3.4.2.2 Expressions for the mass accretion rate

I begin by quoting Elsner & Lamb's (1977) equation for r_0 in terms of the characteristic Alfvén radius for spherical accretion, $r_A^{(0)}$:

$$r_0 \simeq 0.52\, r_A^{(0)} = 0.52\mu^{4/7}\,(2GM_{wd})^{-1/7}\dot{M}^{-2/7}, \tag{3.13}$$

where μ is the magnetic moment (assumed to be dipolar), G is the gravitational constant, M_{wd} is the mass of the white dwarf, and $\dot{M}$ is the mass accretion rate. This equation may be expressed in the form

$$r_0 = 0.52\, B^{4/7}R_{wd}^{12/7}(2GM_{wd})^{-1/7}\dot{M}^{-2/7} \tag{3.14}$$

by writing $\mu = BR_{wd}^3$, where B represents the intensity of the stellar magnetic field and R_{wd} is the radius of the white dwarf.

Having expressed r_0, I now turn to the corotation radius, defined by

$$r_c = \left(\frac{GM_{wd}}{\Omega_s^2}\right)^{1/3}, \tag{3.15}$$

where Ω_s is the stellar angular velocity ($2\pi/P$). The prescription for the dimensionless torque acting on the star is dependent in W87's theory only on the parameter $x_0 = r_0/r_c$.[2] I therefore combine equations 3.14 and 3.15, and substitute $\Omega_s = 2\pi/P$, to yield the following expression for x_0:

$$x_0 = 1.62 \times 10^3\, B_6^{4/7}R^{12/7}M^{-10/21}\dot{M}_{16}^{-2/7}P_3^{-2/3}. \tag{3.16}$$

Here, B_6, P_3, R, and M are the white dwarf's magnetic field strength, rotation period, radius, and mass, in units of 10^6 G, 10^3 s, $R_\odot$, and $M_\odot$ respectively, and $\dot{M}_{16}$ is the mass accretion rate in units of $10^{16}\,\mathrm{g\,s^{-1}}$.

I now observe that the radius of a white dwarf may be expressed as a function of its mass alone using the mass-radius relation of Nauenberg (1972). On the assumption that the white dwarf has a mean molecular weight of 2 (e.g., Shafter & Macry 1987), this relation may be written in the form

$$R = 0.01274\,(M^{-2/3} - 0.607M^{2/3})^{1/2}. \tag{3.17}$$

[2]Note that x_0 is analogous to the fastness parameter in the GL model: $x_0 = \omega_s^{2/3}$.

Finally, combining equations 3.16 and 3.17 leads to the following expression for the mass accretion rate:

$$\dot{M}_{16} \simeq 0.732\, B_6^2 P_3^{-7/3} (M^{-11/9} - 0.607 M^{1/9})^3 x_0^{-7/2}. \tag{3.18}$$

As this equation contains too many unknown parameters, it is of little use on its own. However, it is possible to derive a further estimate of the mass accretion rate, yielding a pair of simultaneous equations which provide a useful tool for estimating the mass accretion rate and the mass of the white dwarf.

To derive the second equation for $\dot{M}$, I begin with the expression for $\dot{P}$ in terms of the torque, N, acting on the white dwarf. This formula is given by W87 (his equation 37) as

$$-\frac{\dot{P}}{P} = \frac{N}{I\Omega_s}, \tag{3.19}$$

where I is the moment of inertia of the white dwarf. Following van Amerongen, Augusteijn & van Paradijs (1987) I adopt Motz's (1952) expression for the latter quantity:

$$I = \frac{M_{wd} R_{wd}^2}{5}. \tag{3.20}$$

I then use this, the expression for the accretion torque of W87 (his equation 33)

$$N \simeq \dot{M} (G M r_c x_0)^{1/2} \left(1 + \frac{2}{9} \frac{1}{x_0^{9/80}} \left[1 - x_0^{3/2} - \frac{x_0^{9/4}}{(1 - x_0^{3/2})^{1/2}} \right] \right), \tag{3.21}$$

and put $\Omega_s = 2\pi/P$, to obtain the following, after some manipulation, from equation 3.19:

$$-\dot{P} \simeq 1.16 \times 10^{-15}\, \dot{M}_{16} M^{-1/3} P_3^{7/3} R^{-2} f(x_0); \tag{3.22}$$

$$f(x_0) \equiv x_0^{1/2} + \frac{2}{9} x_0^{31/80} \left(1 - x_0^{3/2} - \frac{x_0^{9/4}}{(1 - x_0^{3/2})^{1/2}} \right). \tag{3.23}$$

Finally, making use, once again, of the mass-radius relation 3.17 and rearranging equation 3.22 yields the second equation for the mass accretion rate as

$$\dot{M}_{16} \simeq -1.40 \times 10^{11} \dot{P} P_3^{-7/3} (M^{-1/3} - 0.607 M)\, f(x_0)^{-1}. \tag{3.24}$$

3.4.2.3 Primary mass and magnetic moment, and the accretion rate

I have derived a pair of simultaneous equations relating two unknowns: the mass of the white dwarf and the mass accretion rate. If $\log(\dot{M})$ is plotted against M, the intersection of the curves yields estimates for each of these quantities.

A similar methodology was used by Shafter & Macry (1987) in their analysis of the changing spin period in V1223 Sgr, but these authors derived equations for B versus M rather than $\dot{M}$ versus M and had to assume a value for the mass accretion rate because it was not well known. In the present case, however, P and $\dot{P}$ are known from the new quadratic ephemeris, whereas B has been measured by various authors. West, Berriman & Schmidt (1987) deduced a field strength of 5–10 MG from near-infrared polarisation measurements, whereas the latest calculations, from optical-to-infrared polarimetry, suggest that B lies in the range 4–6 MG (Chanmugam et al. 1990). This is the range assumed here. This leaves only the parameter x_0. The usual assumption made by investigators in this field is that the white dwarf is rotating close to (but not at) its equilibrium value, for if the star were rotating much slower than its equilibrium period the net torque would spin the star up on a timescale much shorter than the mass transfer timescale (King, Frank & Ritter 1985). According to W87, equilibrium rotation occurs when $x_0 = x_{eq} \simeq 0.971$.

For plausible values of x_0 in the range 0.8–0.9, the result shown in figure 3.9 is obtained. It should be noted that I have assumed $P_3 = 0.913$ rather than 0.847 (the latter suggested by NMLW), although this decision does not significantly alter the results. From these curves it can be seen that, with the values chosen for the parameters, the mass of the white dwarf lies in the range 0.8–1.0 $M_\odot$. This result is in good agreement with the value ($0.8 \pm 0.2\,M_\odot$) calculated by Penning (1985) from measurements of the orbital phase lag between the H I and He I lines seen in this system. The mass accretion rate suggested from figure 3.9 lies in the range $(5.6\text{–}15.8) \times 10^{16}\,\mathrm{g\,s^{-1}}$. This is larger than that value calculated from the empirical $\dot{M} - P$ relationship for cataclysmic variables given in Patterson (1984)

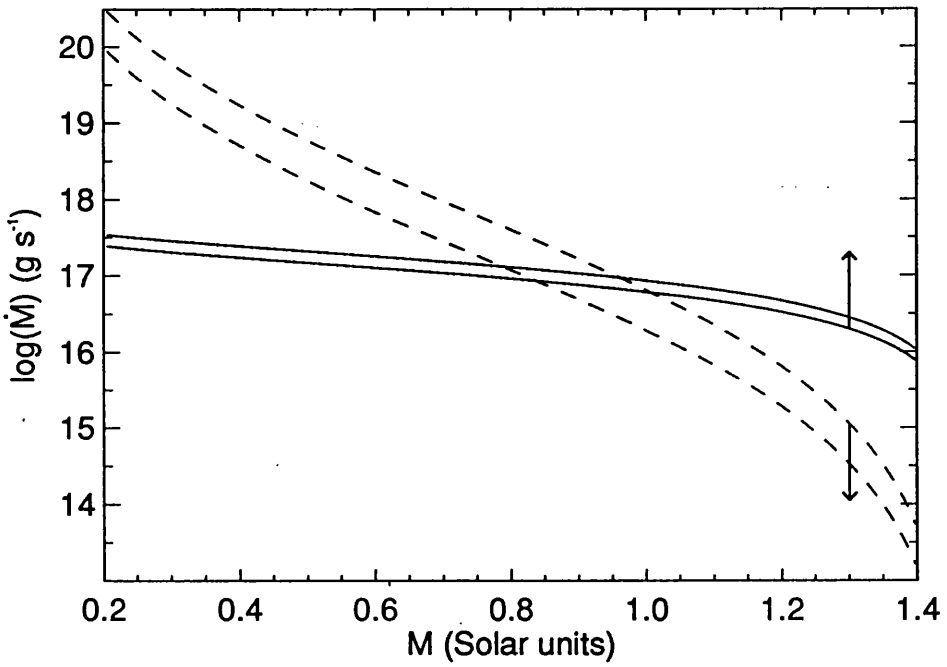

FIGURE 3.9: *The relationships between $\dot{M}$ and M for $x_0 = 0.85 \pm 0.05$. The dashed curves show the association given by equation 3.18, and the solid curve that defined by equation 3.24. The space between each pair delimits the uncertainty implied from the errors on the parameters P, $\dot{P}$, B, and x_0. Arrows on each pair of curves indicate the direction of the dependence on x_0. The overlapping region represents the solution to the simultaneous equations.*

(1.0–4.8 $\times 10^{16}\,\mathrm{g\,s^{-1}}$), but this observed departure is not atypically large given the high scatter in Patterson's $\log(\dot{M}) - \log(P)$ plot (see his figure 7).

Given these results, what can be said about the existence of an accretion disc in BG CMi? Hameury, King & Lasota (1986) have shown that for orbital periods less than $\sim$5 hr, no disc should form because the magnetospheric radius of the white dwarf exceeds the natural circularisation radius of the accreting material. In this instance the material leaving the inner Lagrangian point impacts directly onto the magnetosphere. From the possible white dwarf masses already inferred from figure 3.9 (0.8–1.0 $M_\odot$), the mass-radius relation 3.17 gives R = 0.0081–0.0107. This yields, when combined with the magnetic field strength (4–6 MG) via $\mu = BR_{wd}^3$, a magnetic moment μ_{33} = 0.7–2.5. Now, in figure 7 of Lamb & Melia

(1987), in which disc criteria curves are plotted as a function of orbital period, it is apparent that an accretion disc is not expected to form in BG CMi for values of μ_{33} greater than ~ 0.6. Thus, the initial view based upon the above calculations is that an accretion disc should not reside in this system. However, the magnetic moments given in figure 7 of Lamb & Melia are uncertain by a factor of 2–3. In conclusion, therefore, given the large error on the threshold value of $\mu_{33} \simeq 0.6$, its similarity to the lower-limit of 0.7 derived above, and the uncertainty in the correct value of x_0, it is not possible, based on the data in this chapter, to rule out the presence of an accretion disc in this system.

3.4.3 Implications of the cubic ephemeris

A cubic ephemeris has been reported also for the intermediate polar FO Aqr (Osborne & Mukai 1989). These authors advanced two possible explanations to account for the non-zero $\ddot{P}$ term.

(i) The first possibility is that the change in $\dot{P}$ might be a result of variations in the accretion geometry, or in the mass accretion rate. The question then arises as to what could be causing these changes. An interesting suggestion, proposed by Warner (1988), is that quasi-periodic Solar-type magnetic cycles may be operating in the secondaries of cataclysmic variables. In this situation the secondary is assumed to possess a dynamo-generated magnetic field which is anchored to a radiative core. Any cyclical variation in the strength of this magnetic field then produces corresponding changes in the size of the active convection region in the secondary, modulating the radius of the star accordingly in a quasi-periodic manner. This process in turn modulates the mass accretion rate and, therefore, the torque acting on the degenerate companion.

Two possible diagnostics are available to test this theory. Firstly, as pointed out by Osborne & Mukai (1989), one might expect changes in the mass accretion rate to be reflected in the observed luminosity of the source if an accretion disc produces the majority of the light, with an increase in luminosity producing spin-

up and a decrease in luminosity causing a spin-down. Osborne & Mukai found no evidence for changes in brightness of FO Aqr (aside from the orbital and pulsational modulation) but could not rule out low (~ 0.1 mag) amplitude changes. Similarly in BG CMi, the B band magnitude has not changed, and the V band magnitude measured here is actually 0.3 ± 0.2 mag *greater* than the value quoted by McHardy et al. (1984). This latter result cannot be confirmed owing to the brevity of the V band dataset, but it is not consistent, under the above assumption that a disc produces the majority of the light, with the system being in a state of spin-up.

The second test of the Solar cycle hypothesis is to turn to the $O - C$ *orbital* diagram. The tidal link between the secondary's rotation and the orbital cycle should produce a cyclical variation in the orbital period if the radius of the secondary star varies as discussed above. This process may, for example, be operating in EX Hya (see Hellier & Sproats 1992 and references therein). The orbital $O - C$ modulation in EX Hya has a period (or quasi-period) on the order of twenty years. As BG CMi has been known for a relatively short time (since 1982), it is evident that more observations of pulse arrival times are required before any evidence of a quasi-periodic change in orbital period can be found. So far only a linear ephemeris has been needed to describe the orbital modulation in this star.

(ii) The other possible cause of the $\ddot{P}$ term offered by Osborne & Mukai (1989) is more esoteric, but not impossible. Namely that it is generated due to the orbit of FO Aqr about a third component. This causes $\dot{P}$ to change periodically as FO Aqr alternately advances and recedes about the centre of gravity. If this is true in BG CMi, then the orbit of the companion about the system barycentre clearly has a longer period than the six years spanned by the arrival times reported up until now, as can clearly be seen in figure 3.7. In contrast, the cubic ephemeris shown in figure 3 of Osborne & Mukai shows signs that the 'period' of the $O - C$ curve is of a similar timescale (~ 7 yr) to the timebase of the observations in that paper (i.e., $\dot{P}$ shows signs of being positive at one epoch and negative at another).

3.5 SUMMARY OF CONCLUSIONS

I have calculated new quadratic and cubic ephemerides for the white dwarf's optical pulsations in BG CMi. I have demonstrated that the observed $\dot{P}$ may conceivably be caused by the accretion torques produced by material circulating about the white dwarf in an axisymmetric disc or ring. However, it is also possible, when considering only the data in this chapter, that there may actually be no such structure, so that the accretion stream impinges directly upon the white dwarf's magnetosphere. The latter scenario has been suggested for this system by McHardy et al. (1987) and NMLW. This issue will be discussed extensively in chapter 4.

The cubic ephemeris I have derived provides a better description of the arrival times than does the quadratic one, at a confidence level of 97.3%. Augusteijn (private communication) has stated that for his data (in APS) a cubic ephemeris was also found to fit better than a quadratic, and at a similar ($\sim$95%) confidence level to the present result. I have verified this result from a re-analysis of their data. These results indicate that, until further timings are available, the cubic result should not be discarded. In the event that the $\ddot{P}$ term is indeed non-zero, as in FO Aqr, the implications are either that BG CMi is undergoing fluctuations in mass accretion rate on a timescale of years, or that a third body is gravitationally bound to the BG CMi binary system.

ADDENDUM 3

1. On page 89, second paragraph, line 8, after '$\sqrt{\chi^2_\nu}$.', add: 'In other words, the errors on the $O-C$ values are scaled by $\sqrt{\chi^2_\nu}$. This has the same effect as assigning each point an uncertainty equal to the standard deviation of the data about the best fit.'

2. On page 95, on the end of the first paragraph, add: 'In general, the white dwarfs in intermediate polars show no preference in the sign of their spin period derivative. For example, as mentioned above, whilst the white dwarfs in EX Hya, BG CMi, and DQ Her are spinning up, in others they are spinning down (e.g., V1223 Sgr; van Amerongen, Augusteijn & van Paradijs 1987), and at least one (FO Aqr; Osborne & Mukai 1989) has shown signs of doing both!'

4. BG CANIS MINORIS: IS THE TRUE SPIN PERIOD 847 SECONDS?

Say not, 'I have found the truth,' but rather, 'I have found a truth'.

Kahlil Gibran
The Prophet (1923)

4.1 INTRODUCTION

Until recently, the spin period of BG CMi was taken to be the 913 s period discovered in *EXOSAT* data (McHardy et al. 1982, 1984, 1987). However, this has been thrown into doubt following the detection of an 847 s X-ray period in *Ginga* observations of the star (Norton et al. 1992b, hereafter NMLW). Associating the 913 s period with the spin period suggests that the 847 s period is the positive orbital sideband and implies retrograde rotation. This is a theoretically unlikely situation which NMLW attempted to resolve by proposing a predominantly discless scenario in which 847 s is the spin period, making 913 s the usual (negative sideband) beat period. This claim of NMLW is difficult to refute on the assumption that the 847 s period is real.

To determine the true value of the spin period, I present an analysis of high time-resolved optical spectroscopy of BG CMi. To the best of my knowledge, data such as these have not been published on this system prior to this work. The primary aim is to search for evidence of periodic line modulation at the proposed 847 s period. In particular, a radial velocity modulation at this period is expected

if it represents the spin cycle. Thus, an 847 s period is expected to be manifest in the V/R ratio (i.e., the ratio of the blue and red intensities on either side of the rest wavelength) of the emission lines. These data also provide an opportunity to search for a modulation at the $\sim$1100 s period which has recently been noted in optical photometry of this system (T. Augusteijn, private communication; see also chapter 3).

4.2 OBSERVATIONS

4.2.1 ACQUIRING THE DATA

The data presented in this chapter were obtained at La Palma using the two-arm Intermediate-dispersion Spectroscopic Imaging System on the William Herschel Telescope. BG CMi was observed in 1991 on December 14–15 and 16–17. On both nights, a 316R grating was used on the red arm, covering the wavelength range 6600–8250 Å at a reciprocal dispersion of 1.4 Å pixel^{-1}. For the blue arm a 300B grating was employed on the first night, covering 4000–5300 Å at a reciprocal dispersion of 1.3 Å pixel^{-1}. On the second night, however, a higher reciprocal dispersion (0.7 Å pixel^{-1}) 600B grating was employed instead, narrowing the wavelength range to 4050–4950 Å and avoiding further unwanted coverage of the region redward of Hβ. In total 217 useful spectra were secured, 108 blue and 109 red, covering approximately ten and eleven 913 s pulse cycles on the first and second nights respectively ($\sim$1.0 and 0.8 orbital cycles). The exposure time was 60 s for both arms except for the first two pairs of spectra, which were accumulated in integrations of first 90 s, and then 30 s, to establish the optimum integration period. Owing to the software setup it was not possible to start exposures on the red and blue arms simultaneously. Instead the red arm was exposed followed, typically 3 s later, by the blue. For speed of readout a region on each CCD (EEV5) measuring 1270 by 57 pixels was used, and on-chip binning by a factor of three was enabled in the spatial direction.

Flux standards were observed at the start and end of each night. These were used for the removal of the instrumental response function using the methods outlined in §A.4.3. Atmospheric Telluric band removal has not been possible as an appropriate (F8) standard was not observed. Table 4.1 summarises the observations.

		Red arm (316R)		**Blue arm**		
Date (1991)	Int (s)	λ range (Å)	No. of spectra	λ range (Å)	No. of spectra	Grating
December 14–15	90	6600–8250	1	4000–5300	1	300B
	30	6600–8250	1	4000–5300	1	300B
	60	6600–8250	34	4000–5300	34	300B
December 16–17	60	6600–8250	72	4050–4950	73	600B

TABLE 4.1: *BG CMi spectroscopy observing details.*

4.2.2 OBSERVING CONDITIONS

Figure 4.1 shows the mean red and blue continuum variation as a function of time and binary phase (the latter according to the orbital ephemeris of Patterson & Thomas 1993 [hereafter PT], used throughout this chapter). I have constructed this by summing the counts in line-free (and atmospheric band-free) regions from all red and blue spectra on both nights. Conditions were non-photometric for the duration of all observations, which made guiding rather difficult. Consequently, BG CMi moved outside the slit on the first night near Heliocentric Julian Date (HJD) 2448605.555, approximately halfway into the observation, as can be seen in figure 4.1. That this was caused by guiding difficulties, and not obscuring clouds, is confirmed by the fact that the emission lines in the sky spectrum are unaffected at

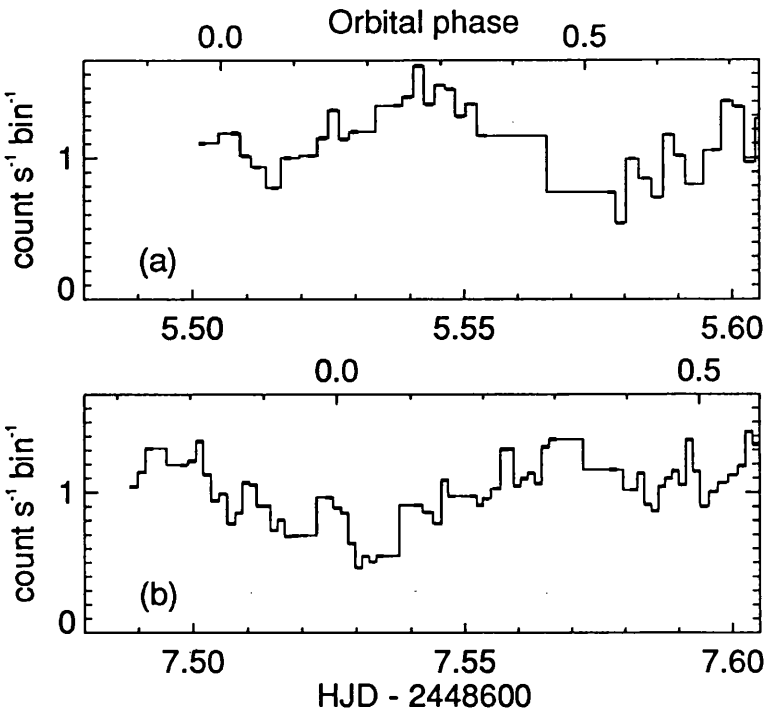

FIGURE 4.1: *The mean continuum level of BG CMi as a function of time (lower axes) and orbital phase (upper axes, using the ephemeris of Patterson & Thomas 1993) as observed on (a) the first night and on (b) the second night.*

this time. The rise in the lightcurve after HJD 2448605.958 is a result of the target gradually returning to the middle of the slit. Spectra between the aforementioned times have been excluded for all but the V/R ratio analysis (the decrease in line intensity does not affect their asymmetry).

The continuum variation on the second night more closely resembles the variability expected of an intermediate polar (cf. figure 3.3) than does the variation on the first night. The orbital phases of both observed spectroscopic minima are consistent with the orbital minima observed in the B and R band photometry of chapter 3, given the orbital ephemeris of PT.

4.3 Data analysis

4.3.1 Mean spectrum

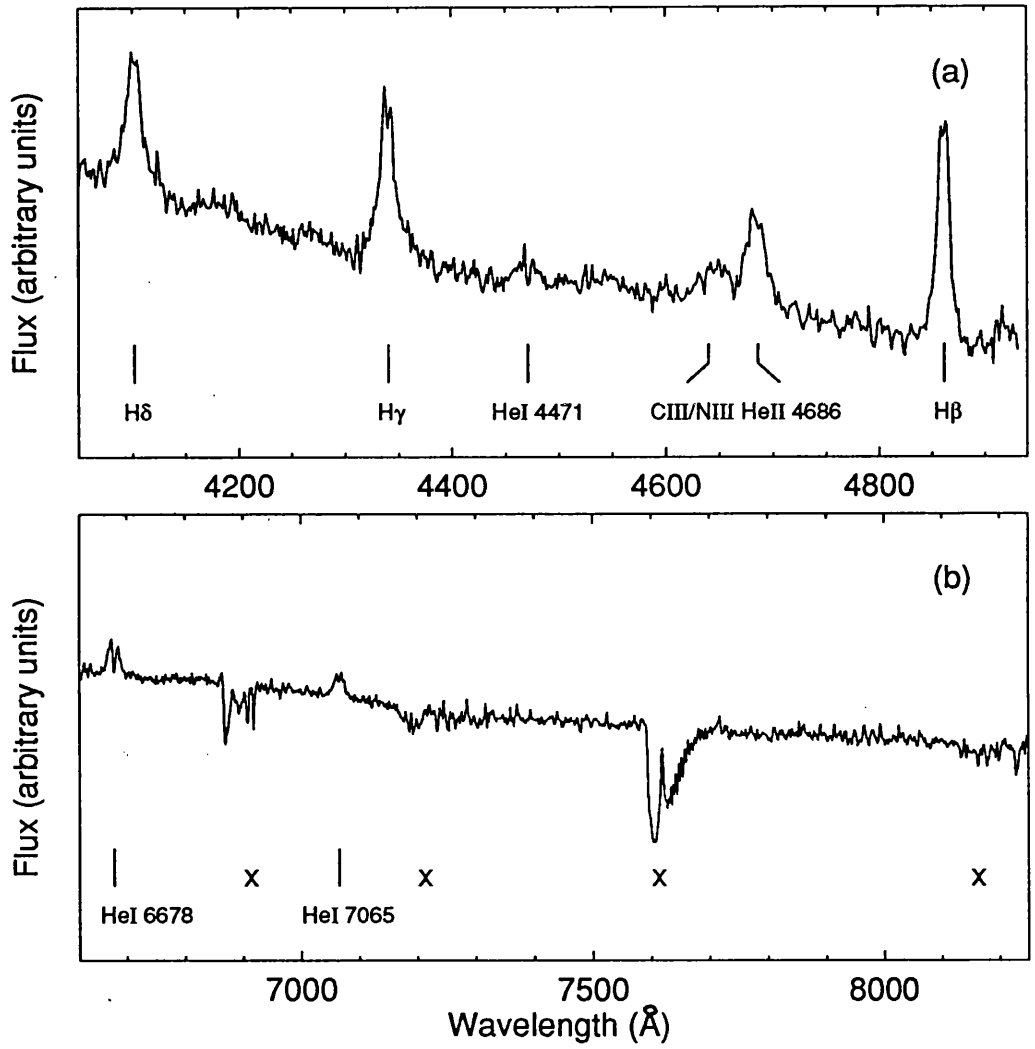

FIGURE 4.2: *Blue (a) and red (b) phase-averaged spectra of BG CMi, corrected for instrumental response. The vertical scales are the same in each case. The Xs indicate absorption features formed in the Earth's atmosphere.*

Figure 4.2 shows the co-added and corrected red and blue spectra. The slope of the blue continuum over its entire wavelength range is described fairly well by a power law, $F_\nu \propto \nu^{+0.29\pm0.05}$, whilst for the red continuum I obtain $F_\nu \propto \nu^{+0.36\pm0.05}$. These are in fair agreement with the result of McHardy et al. (1987), who derive the index $\alpha \simeq +0.4$ for the blue continuum (they do not give an error).

The broad emission lines which are present in the spectrum have full-width at zero intensity (FWZI) $\sim 2800\,\mathrm{km\,s^{-1}}$, and are typical of intermediate polars. These include the hydrogen Balmer series (Hβ, Hγ, and Hδ), He II λ4686, the C III/N III λ4640 blend, He I λ6678, He I λ7065, and, less prominently, He I λ4471. The Balmer and He I lines are double-peaked, with evidence of self-reversal in He I λ4471 and in He I λ6678. The He II λ4686 line, though not obviously similar in profile to the other lines, is also complex. Note that the non-photometric conditions do not affect *relative* line intensities; thus, the integrated fluxes of the strongest lines relative to Hβ (i.e., total area in the line above the continuum) are listed in table 4.2. These are fully consistent with the values derived by McHardy et al. (1987). However, the equivalent widths (the mean of all the spectra), also listed in table 4.2, are consistently smaller than those given by McHardy et al. in all lines except He II λ4686.

Line	Strength (Hβ = 1)	Equivalent width (Å)
Hβ	1.00	13.1 ± 0.2
Hγ	0.86 ± 0.20	9.6 ± 0.1
Hδ	0.63 ± 0.22	6.5 ± 0.1
He II λ4686	0.65 ± 0.23	9.4 ± 0.2

TABLE 4.2: *Emission line equivalent widths in BG CMi, and strengths relative to Hβ.*

The poor spectral resolution and low signal-to-noise prevents one from examining the line structures in any detail; it does not permit, for example, radial velocity measurements of individual components (e.g., as in Hellier, Cropper & Mason 1991). It is nevertheless possible to infer the gross motion of bodies of material in the system by examining the V/R ratio—the ratio of the intensities of

the blue and red sides of a given spectral line. Moreover, any variation of the line fluxes and of the equivalent widths may also yield clues to the location of the sites of line emission. In subsequent sections I examine these quantities and investigate the possibility of variability at the 913 s pulsational period (McHardy et al. 1982, 1984, 1987), the 847 s period (NMLW), and the orbital period (PT). Note that I have included only the He II λ4686 line and the three Balmer lines (Hβ, Hγ, and Hδ) in this analysis as all other lines are too weak.

Before discussing further results, I outline a period-searching routine that I have devised for the analysis of these data.

4.3.2 PERIOD-SEARCHING

The non-photometric conditions and the use of a narrow slit (0.74″) have produced spectra with a high noise level in some cases, and often the emission lines are not discernable in individual spectra. As a result the values obtained when calculating V/R ratios and equivalent widths, as well as their associated errors, are observed to fluctuate between spectra by as much as an order of magnitude. In these circumstances it was found that a Fourier analysis could not reliably locate any periodicities in these data. Thus, I have devised a technique for period-searching which takes account of non-uniform errors.

The stages used in the period-search are as follows. First, the frequency range to be searched is defined by specifying the start and stop frequencies and a frequency step (typically $\sim$5000 frequency steps between start and stop). The data to be searched are then folded on the period corresponding to the first frequency in the defined range, and rebinned into a pre-defined number of bins. However, as many of the datapoints have large errors, simply binning the data by taking the mean of the datapoints in each phase bin is not satisfactory. Instead I take account of errors by performing a *weighted mean*, defined as

$$\bar{S}_n = \sum_{i=1}^{n} \frac{x_i}{(\Delta x_i)^2} \left(\sum_{i=1}^{n} (\Delta x_i)^{-2} \right)^{-1}; \qquad (4.1)$$

$$\Delta\bar{S}_n = \left(\sum_{i=1}^{n}(\Delta x_i)^{-2}\right)^{-1/2}, \tag{4.2}$$

where n is the number of datapoints, $x_i \pm \Delta x_i$, to be summed over in a particular bin. The folded data are then fitted, using χ^2 minimisation, with a sinusoid of the form

$$y = c + a\sin(2\pi[x - \phi]), \tag{4.3}$$

where x is the phase of the folded data and c, a, and ϕ are the mean offset, semi-amplitude, and phase of the fitted sinusoid respectively.

This process is then repeated for each frequency step in the defined range—using the same folding epoch and number of folding bins each time—yielding a set of best-fit sinewave parameters for each test frequency.

For a given folded dataset, the ratio of the amplitude, a, of the best-fitting sinusoid to the error, Δa, on that amplitude will be larger the better the fit. Thus, this ratio provides a useful diagnostic for testing the quality of the fit and, therefore, for investigating which periods are actually present in the timeseries. When the ratio $a/\Delta a$ is plotted as a function of frequency, it therefore yields a 'frequencygram', not unlike a Fourier power spectrum in appearance, with the frequency most likely to be present in the data identified as that which maximises this ratio.

Figure 4.3 displays the typical result obtained when the searching routine is run on a test dataset, compared with the result of a Fourier analysis on the same dataset. The test dataset comprises twenty cycles of a sinusoid of frequency 1.0, semi-amplitude 0.25, and offset 1.0, plus randomly generated numbers between -0.5 and $+0.5$ to simulate noise. The sampling rate is random with approximately three points per cycle. In addition, 10% of the datapoints in the test dataset have been set to very large numbers (a factor $\sim$3–10 times larger than the maximum value of the sinewave), and the corresponding errors set proportionately. This simulates a typical dataset obtained from the BG CMi spectroscopy. Clearly a Fourier analysis is unable to locate the test frequency convincingly as it cannot

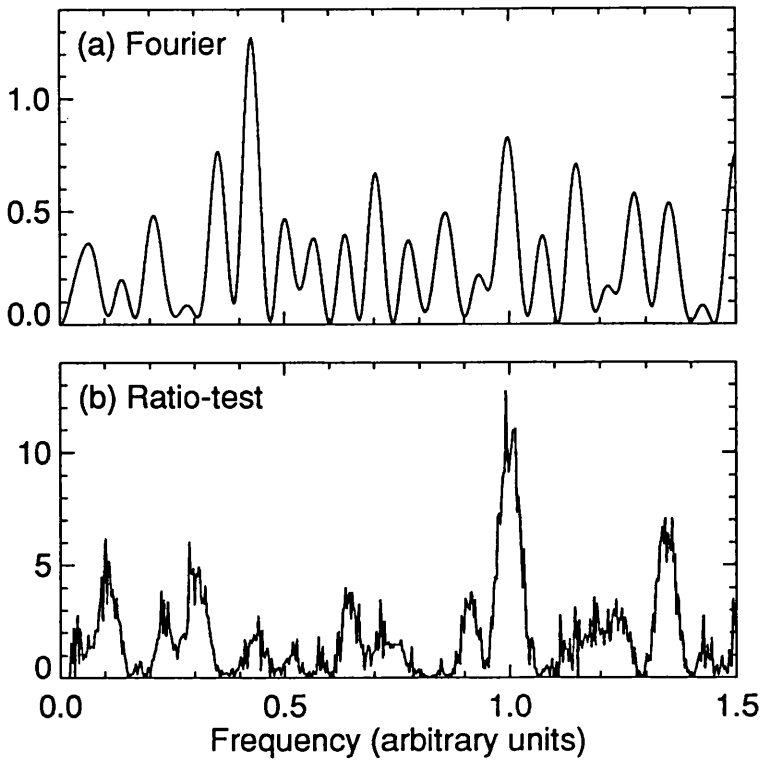

FIGURE 4.3: *Comparison of the output from two period-searching routines. (a) shows the Fourier spectrum obtained from a test dataset containing a sinusoid of frequency 1.0 and noise characteristics typical of those exhibited by the V/R ratio and equivalent width timeseries in this chapter. (b) shows the frequencygram obtained from the same test data, but using the ratio-test described in §4.3.2.*

'handle' the datapoints which depart significantly from the trend of the sinewave. The ratio-test however, effectively ignores these points because of the very low weight associated with them, and identifies the period successfully.

It is, of course, permissible to use the parameter c, or $|\phi|$, or even χ^2_ν as the period-searching 'statistic'. However, I found that these quantities were not able to provide as sensitive a test as the semi-amplitude, a. Chi-squared, in particular, is not suitable because the errors on the binned datapoints (whether they be V/R ratio or equivalent width measurements) are large, so that χ^2_ν changes very little over the frequency space.

A final point is that this method searches for sinusoidal trends in a dataset. In

general, however, it will find a period successfully if there is only one maximum and minimum per cycle at that period. For example, this method is able to locate triangular or square-wave modulations.

4.3.3 THE PULSATIONAL MODULATION

4.3.3.1 V/R ratio

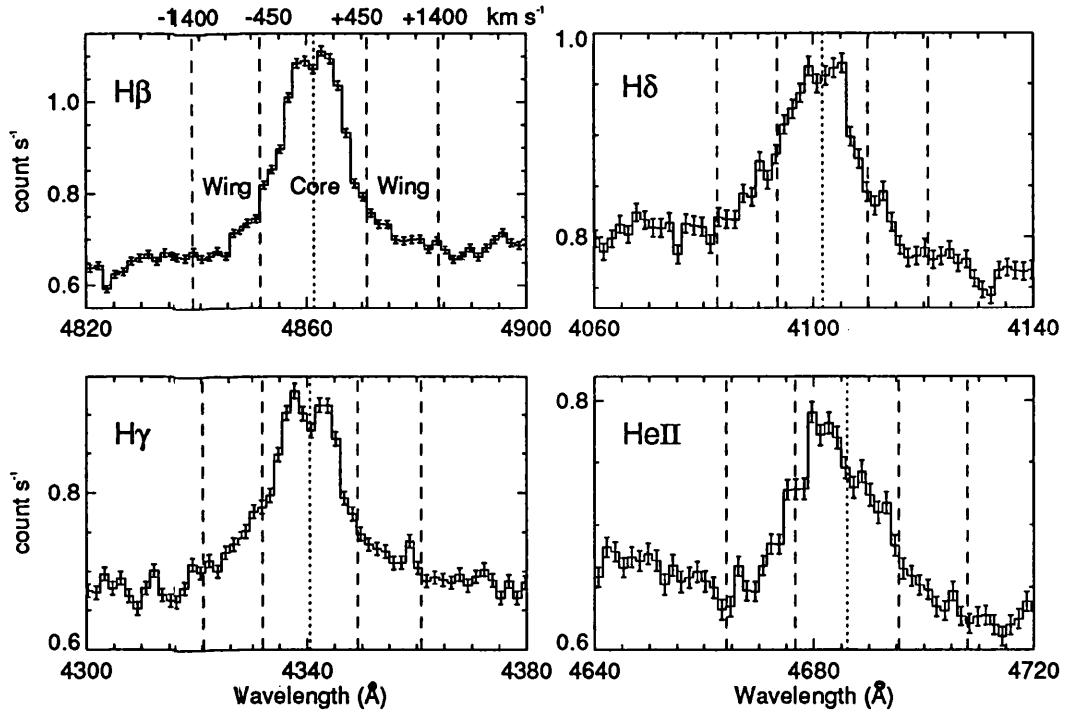

FIGURE 4.4: *The average Balmer and He II λ 4686 line profiles in BG CMi, showing the extent of each line defined, for V/R ratio measurements, as the 'core' and the 'wing'. Dotted lines indicate the laboratory rest wavelengths.*

Spin-modulated emission is expected to have a high velocity and thus be confined to the line wings. Thus, I initially excluded the line cores from the V/R ratio analysis and concentrated on their wings. The velocity where the line wings blend into the continuum was estimated for each line by eye from the average spectrum and then a mean was calculated to yield a value of $\pm 1400\,\mathrm{km\,s^{-1}}$ (FWZI $= 2880\,\mathrm{km\,s^{-1}}$). The position of the core/wing boundary is, however, more arbitrary; a value of

$\pm 450\,\mathrm{km\,s^{-1}}$ was arrived at because in searching for a modulation in the V/R ratio of the line wings at the pulsation period(s), the maximum modulation fraction was found for this particular value. I thus define absolute velocities in the range 450–$1400\,\mathrm{km\,s^{-1}}$ as belonging to the wings of the lines, and absolute velocities less than $450\,\mathrm{km\,s^{-1}}$ as belonging to the core. These velocities are indicated by the dashed lines in figure 4.4, showing the average profiles of the emission lines of He II λ4686 and the three Balmer lines Hβ, Hγ, and Hδ. See §A.4.6 for an explanation of the V/R ratio calculation in general.

Prior to a period-search I generated a mean V/R ratio timeseries for the Balmer lines by adding together the violet (V) contributions from the three lines, repeating for the red (R) contributions, and then dividing the former by the latter. I have not included the He II λ4686 line in this mean because it may originate in a spatially distinct region. Figure 4.5 shows the results of a period-search of the V/R ratio data from the wings of the three Balmer lines and from the He II λ4686 line, using the ratio-test outlined in §4.3.2. (Note that the aliasing in this diagram is due to a 1.9 d gap in the data). There is a similarity between the results for the Balmer lines and the 913 s sinusoidal test dataset. The latter timeseries was created by setting the V/R ratio datapoints to unity (and therefore has the same sampling pattern as the data) and adding a sinewave of period 913.49 s and semi-amplitude 0.25, as well as randomly generated numbers between -0.5 and $+0.5$ to represent noise. The similarity between the Balmer results and the test data results suggests that the V/R ratio from the wings of the Balmer lines contains a period consistent with 913 s. No evidence for an 847 s period is observed in the V/R ratio Balmer line data. If such a period *were* present this would broaden the peak and shift it to a frequency at some point between the two periods, depending on the relative amplitudes of the modulation at each period. The He II λ4686 results are far more noisy, but the indications are that the 913 s period is probably present here as well.

The noise levels in figure 4.5 are rather high. Therefore, to investigate further the presence of a periodicity in the V/R ratio data I have multiplied together the

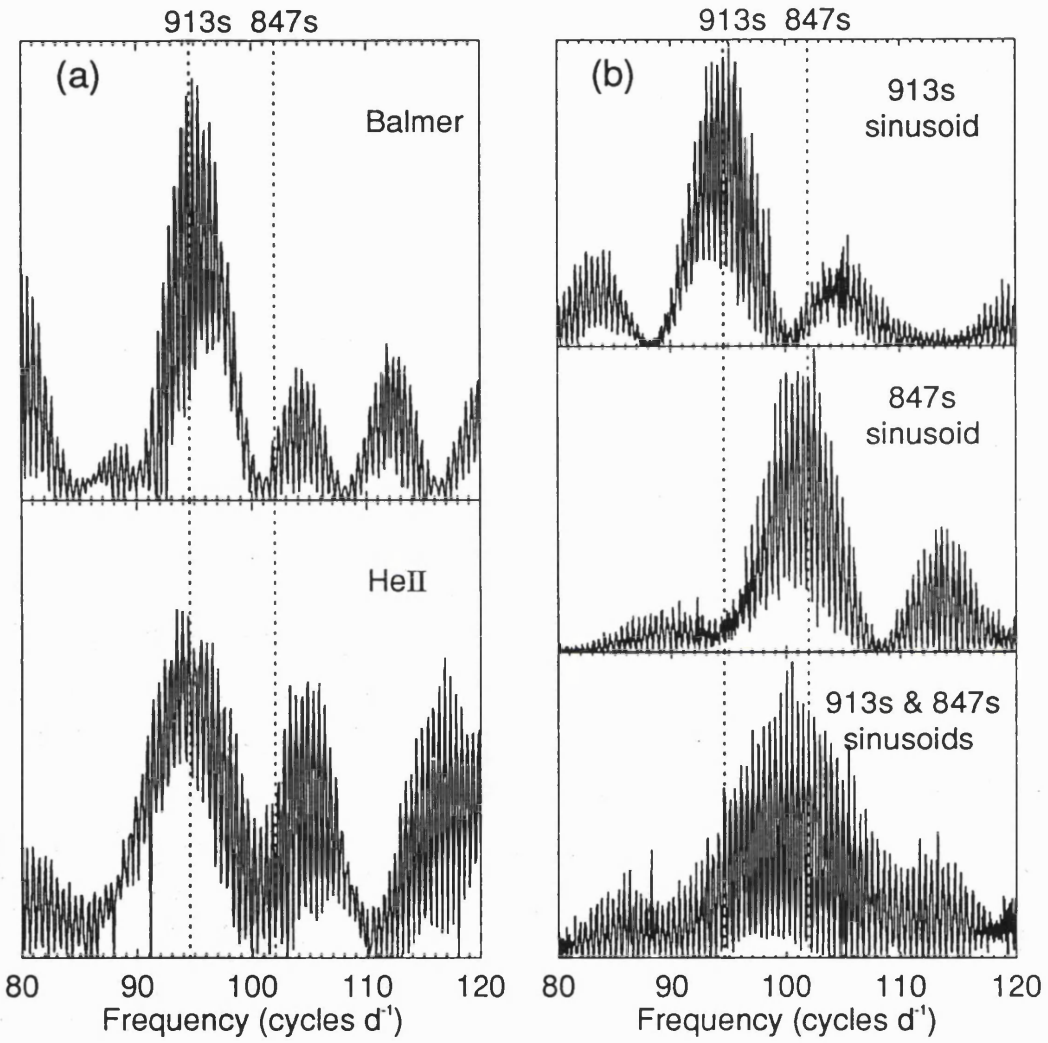

FIGURE 4.5: *The results of (a) period-searching the V/R ratio measured in the line wings of BG CMi using the ratio-test, compared to the results of (b) period-searching three sets of sinusoidal test data whose periods are indicated in the panels. In that test dataset which contains two sinusoids (lower right), their amplitudes are equal.*

'power' axes of the two V/R ratio frequencygrams shown in figure 4.5(a). This is purely an arbitrary procedure which enhances those peaks that are present in both frequencygrams, and 'cancels out' any features which are due to noise. The result of this process, covering periods in the range 346–8640 s, is shown in figure 4.6. This diagram readily confirms that a periodicity indeed exists in the V/R ratio from the wings of the emission lines, that it is consistent with the known 913 s period, and that an 847 s period is not present. Moreover, no period is detected at 1693 s (twice 847 s) or 1827 s (twice 913 s), both of which have recently been tentatively suggested as alternative candidate spin periods (PT).

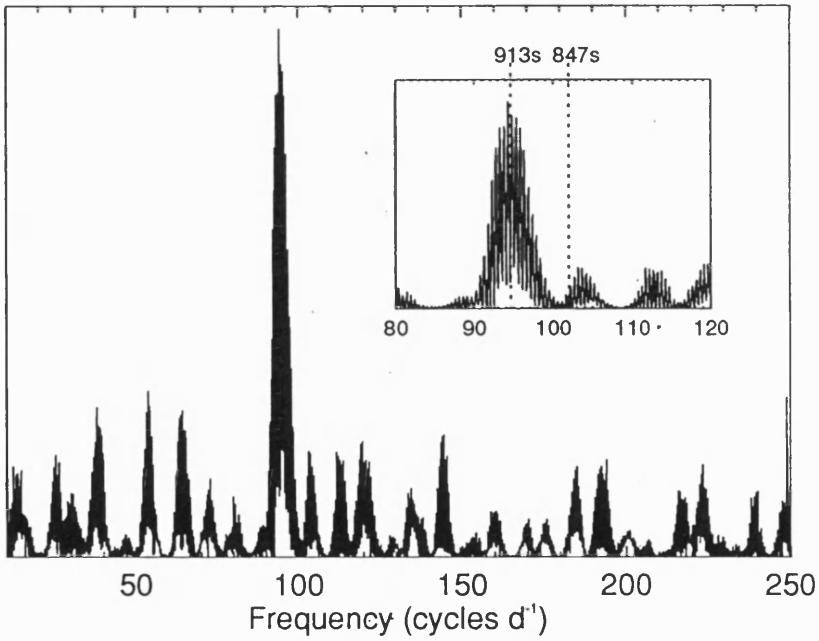

FIGURE 4.6: *The result of multiplying together the y-axes of the Balmer line and He II λ 4686 ratio/frequency datasets shown in figure 4.5(a), illustrating the presence of a 913 s periodicity in the V/R ratio from the wings of the emission lines.*

These results are further illustrated in figure 4.7, showing the V/R ratio data folded on the two candidate pulsation periods; the 847 s period is taken from NMLW and the folding epoch is arbitrary, whilst for the 913 s folds I have used the newly derived cubic ephemeris from chapter 3 (table 3.5). I have also included, for com-

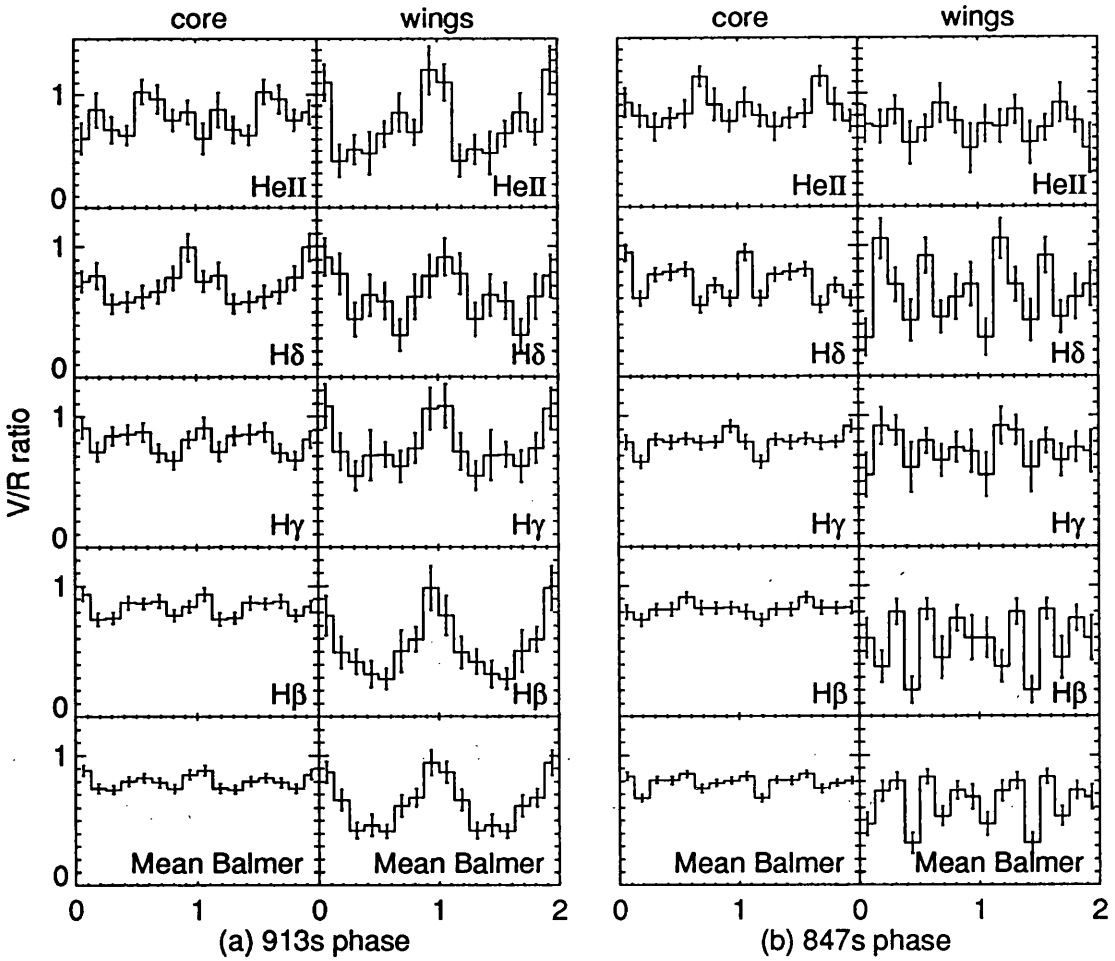

FIGURE 4.7: *The V/R ratio data folded on (a) 913 s using the cubic ephemeris in chapter 3, and (b) 847 s using the period of Norton et al. 1992b. The lowest panels in each block show the mean Balmer line V/R ratio data.*

parison, the V/R contributions from the line cores. The modulation in the line *wings* is obvious and quasi-sinusoidal at the 913 s period, but, as expected, there is no coherent evidence for such a modulation in the core at this period. The maximum of the V/R ratio at this period lies at phase zero, defined as maximum optical 913 s intensity. Maximum V/R ratio at maximum optical spin intensity is seen in AO Psc (Hellier, Cropper & Mason 1991), FO Aqr (Hellier, Mason & Cropper 1990), and EX Hya (Hellier et al. 1987), so these initial results for BG CMi suggests that 913 s is the real spin period. The 847 s period folds are erratic, and no coherent variability is seen in the wings or the core.

The V/R ratio shown in figure 4.7 is less than unity at almost all phases. Figure 5 of Penning (1985) shows the systemic velocity of BG CMi to be $\sim +50\,\mathrm{km\,s^{-1}}$. I have performed tests which show that if the central wavelength in the V/R ratio calculation is varied by as much as $\pm 50\,\mathrm{km\,s^{-1}}$ this does not significantly alter the values obtained. Therefore, the observed red offset of the V/R ratio is probably not due to systemic motion, and may indicate a phase-independent excess of redshifted material.

4.3.3.2 Equivalent widths, line intensities, and continuum

As in the manner of the V/R ratio data, I have created mean timelines from the Balmer line intensity and equivalent width data (the former being the area under the lines but above the continuum). In figures 4.8(a) and (b) I show the results of a period-search of these data, and of similar data from the He II λ4686 line. The line intensities (figure 4.8[a]) show variation at both periods 847 s and 913 s. This is indicated by the fact that the peaks in these plots are broad, asymmetric, and not centred on any of these periods (cf. the sinusoidal test datasets in figure 4.5). Of the periods present in the intensity of the He II λ4686 line, that at 847 s appears to be more dominant; in the Balmer lines the 913 s period is stronger.

It is not immediately clear which period (if any) is actually present in the equivalent width data (figure 4.8[b]). The frequencygrams have distinct peaks at *both* periods, a behaviour which I have been unable to duplicate using test data comprising combinations of 913 s and 847 s sinusoids. As stated earlier, this instead produces a broad or asymmetric peak. As the peak at 847 s is stronger I suggest that this is the true period on which the equivalent width varies. Figure 4.9 shows the results of multiplying together (a) the He II λ4686 and Balmer line intensity frequencygrams shown in figure 4.8(a), and (b) the He II λ4686 and Balmer line equivalent width frequencygrams shown in figure 4.8(b). The latter confirms that the dominant period in the equivalent width is 847 s.

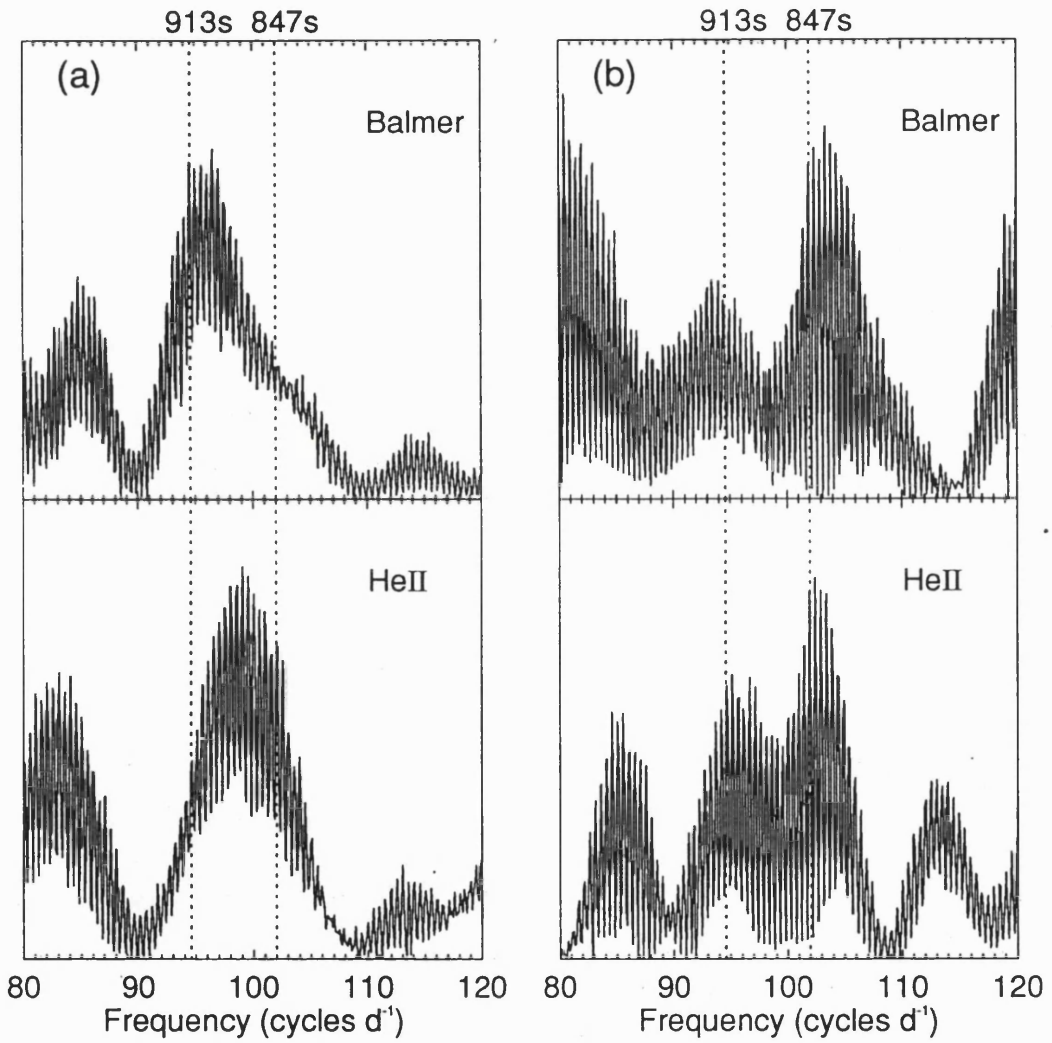

FIGURE 4.8: *Frequencygrams of (a) the line intensities and (b) the equivalent widths in BG CMi. See the discussion in §4.3.3.2.*

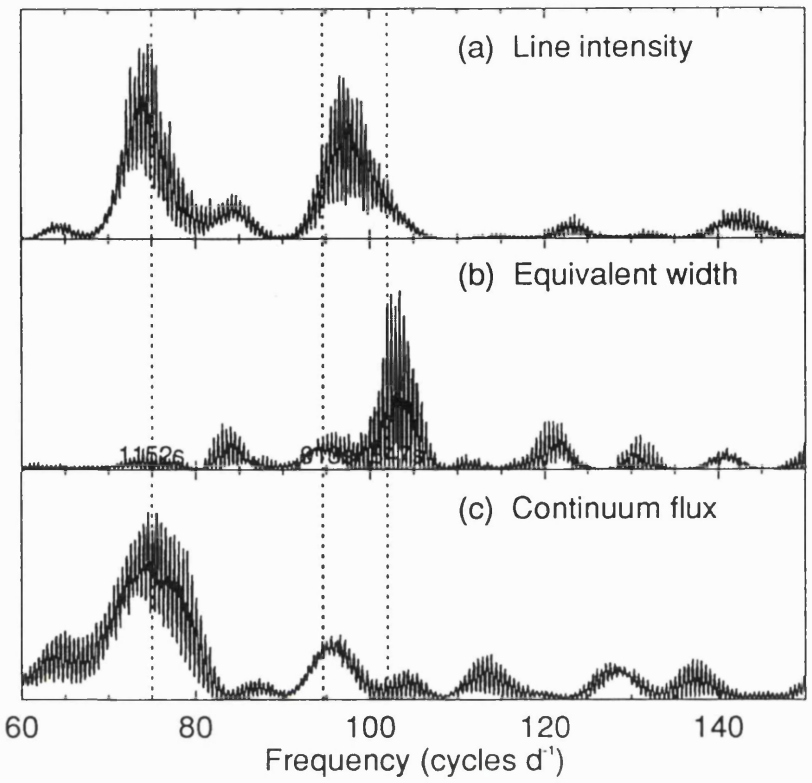

FIGURE 4.9: *(a) The result of multiplying together the 'power' axes of the He II λ 4686 and Balmer line intensity frequencygrams shown previously (figure 4.8[a]). (b) The same as (a), but showing the equivalent width. (c) The frequencygram obtained from the mean continuum lightcurve.*

A frequencygram obtained from the continuum data is shown in figure 4.9(c). Periods present include 913 s and one at ∼ 1152 s. The ∼ 1152 s continuum period is seen clearly in the line intensity data as well (figure 4.9[α]). This period is interesting because, although it has has not been previously published, there are indications of a similar period in the B and R band optical photometry of chapter 3 (see figure 3.5), and in independent but unpublished photometry of BG CMi (T. Augusteijn, private communication; D. De Martino, private communication). The line intensity and continuum data are shown folded on this period in figure 4.10. The modulation is quasi-sinusoidal, and the line intensity varies in phase with the continuum. I will discuss this period in §4.4.2.

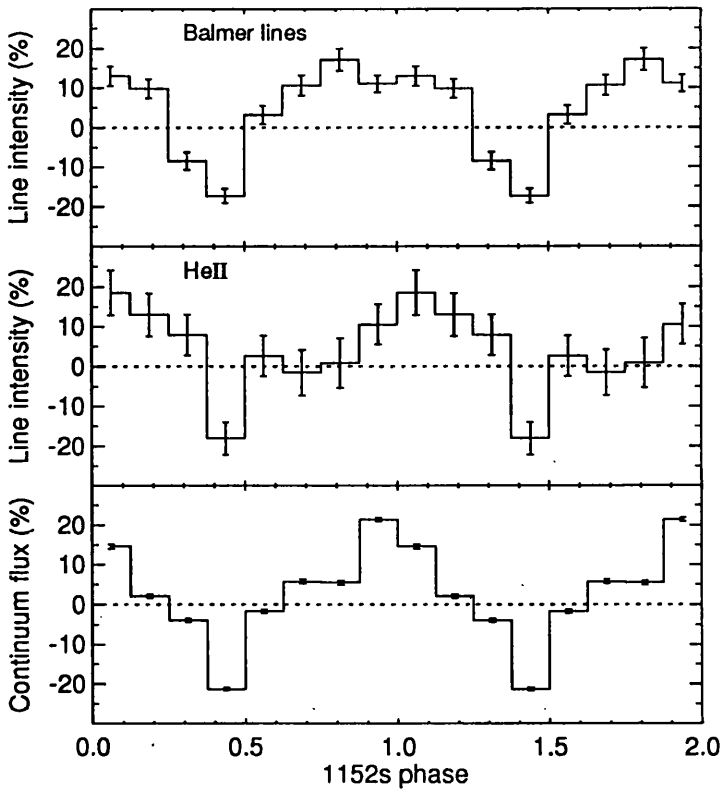

FIGURE 4.10: *Line intensities and continuum flux folded, with arbitrary phasing, on a period of 1152 s. Two cycles are shown for clarity.*

Finally, figures 4.11(a) and (b) show the equivalent widths, line intensities, and continuum folded on the two candidate spin periods, 913 s and 847 s respectively. I have used the same ephemerides as for the V/R ratio data in figure 4.7. Figure 4.11(a) shows that the equivalent width is at most weakly modulated at the 913 s period. The line intensity and continuum 913 s pulsations are therefore expected to have similar percentage amplitudes and occur in phase, as is indeed observed. Figure 4.11(b) shows, as indicated above, that an 847 s period appears to be present only in the equivalent widths and line intensities. The line intensity and equivalent width 847 s modulations are in phase. As no 847 s period is seen in the continuum or in optical photometry, this suggests that the equivalent width period is due entirely to the line intensity varying at 847 s. This interpretation is in agreement with the observed percentage variations in equivalent width and

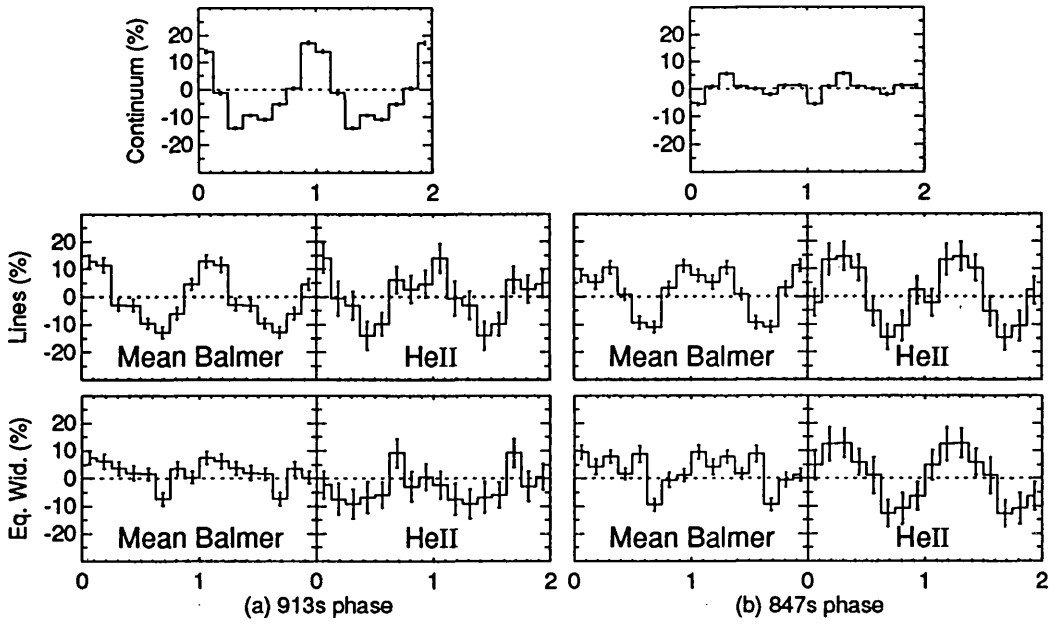

FIGURE 4.11: *Continuum data, line intensities and equivalent widths folded on (a) 913s, and (b) 847s. The flux and intensity units are arbitrary, so the percentage variation is shown instead.*

intensity at this period.

4.3.4 ORBITAL-CYCLE LINE VARIABILITY

The orbital variability is not easy to examine using these data because less than two orbital cycles were covered, and no obvious repetition with orbital phase is observed. Figure 4.12 (left panel) shows the Hβ line profile plotted as a function of orbital phase. Other lines are too weak, and significant changes in their profiles are not evident. Note that each profile shown in this figure is a mean of exactly ten sampled from a wide range of pulse phases; thus, any pulsational variations have been effectively smeared out. Two aspects of this diagram are of interest. Firstly, there is no orbital 'S-wave', in contrast to the more usual behavior of intermediate polars (see §1.5.4.3 for an explanation of the S-wave). Secondly, there is a strong, extended blue wing which appears quite abruptly (within 0.12 orbital cycles) near orbital phase 0.8. The latter behaviour is also evident in figure 4.12(b), showing

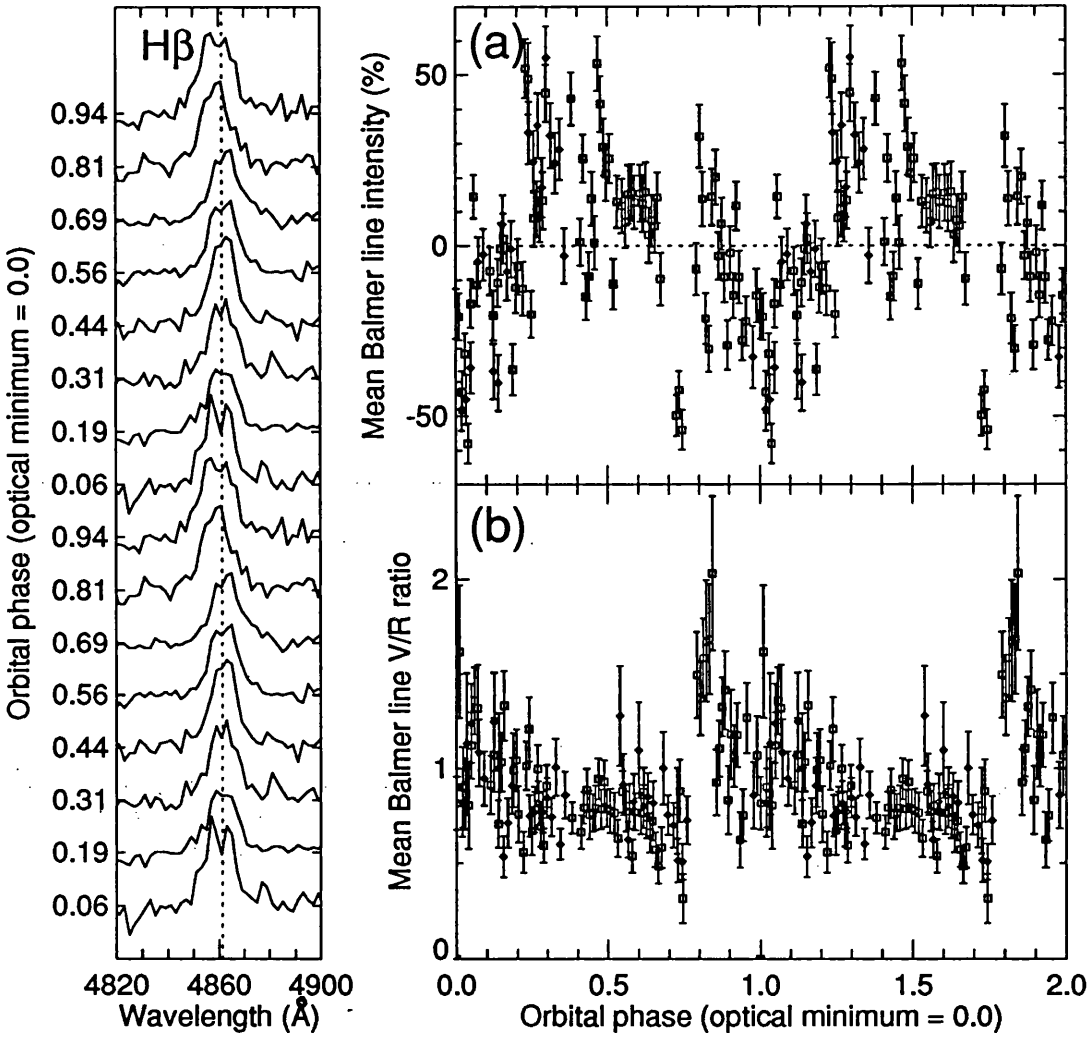

FIGURE 4.12: *Balmer line orbital variation in BG CMi. The panel on the left shows the Hβ profile as a function of orbital phase. These data are repeated: two cycles are shown. The panels on the right show (a) the mean Balmer line intensity, and (b) the mean Balmer line V/R ratio, plotted as a function of orbital phase. Again, two cycles are shown for clarity. The open squares are data obtained on day 1 (1991 Dec 14–15); the filled diamonds are from day 2 (1991 Dec 16–17). The dotted lines indicate the laboratory (rest) wavelengths. Note that some intensity data has been excluded from (a) because the star moved outside the slit on day 1 (see §4.2.2).*

the mean Balmer line V/R ratio timeseries folded (not rebinned) on the binary period (note that this is an average over the entire widths of the lines, not just the wings or core). Near phase 0.75 there is a reduction in the V/R ratio, accompanied by a narrow dip in the mean line intensity (figure 4.12[a]). Then at phase ~ 0.8 the line intensity increases and the V/R ratio jumps to ~ 2. The line intensity variation is otherwise quasi-sinusoidal, showing a minimum at orbital phase zero, corresponding to photometric minimum.

Orbital phase 0.8 was only observed on the second night, so it is not known if the variability seen around this phase repeats itself. However, it should be remembered that although the line flux reduction at phase 0.75 could conceivably be due to poor observing conditions, the fact that a substantial change in the V/R ratio is also seen near this phase indicates that these changes are probably intrinsic, as atmospheric conditions will not have affected the lines' asymmetry.

The He II λ4686 line data are poor, but they can be seen folded on the binary cycle and rebinned in figure 4.13. The mean Balmer line data from figure 4.12 are also rebinned in figure 4.13 for comparison purposes. No obvious trend is noticed in the He II λ4686 V/R ratio. The He II λ4686 line intensity is also erratic, but note the presence of a minimum at orbital phase ~ 0.05, consistent with that seen in Hβ.

4.3.5 Summary of results

My main findings are as follows.

(i) The V/R ratio in the wings of all Balmer lines and in the wings of He II λ4686 is modulated in a quasi-sinusoidal fashion at a period of 913 s, *not* 847 s. As has been seen in other intermediate polars, the maximum of the V/R ratio occurs at the maximum of the optical pulse cycle.

(ii) The mean Balmer line intensity varies at periods of *both* 847 s and 913 s. Similar modulation is seen in He II λ4686 with the same relative phasing. The

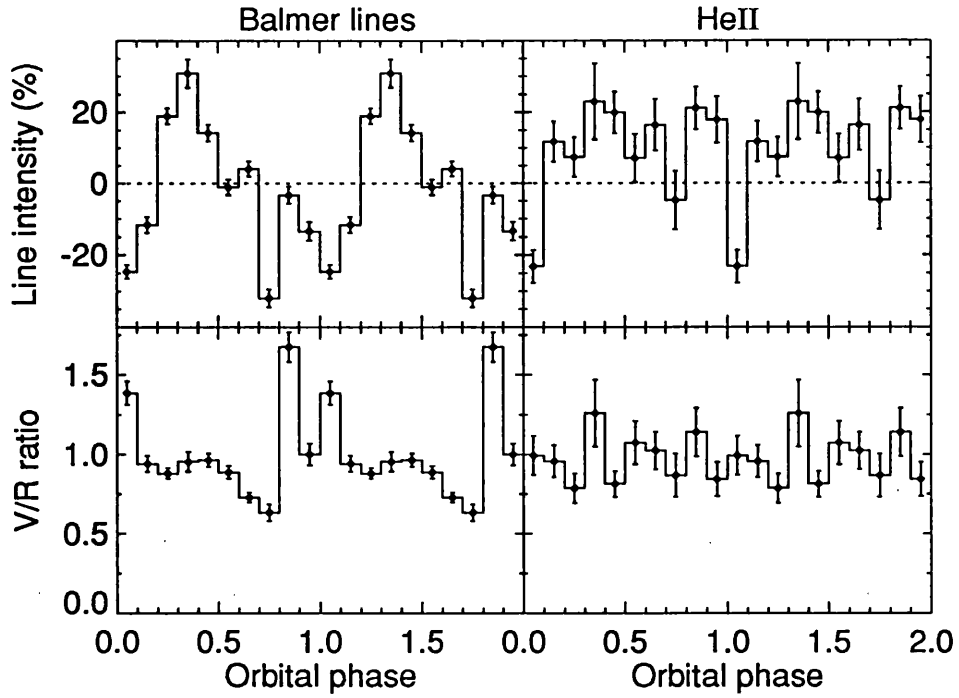

FIGURE 4.13: *Balmer and He II λ 4686 line orbital variation in BG CMi. The panels on the left contain the same data as in figure 4.12, but rebinned. For comparison, the panels on the right show the He II λ 4686 line intensity and V/R ratio.*

continuum varies at 913 s, not 847 s. Therefore, the equivalent widths of all lines vary at 847 s, in phase with and to the same extent (±15%) as the line intensities. As the 913 s continuum pulsation is in phase with the line intensity variation at this period, little or no equivalent width modulation is observed at 913 s.

(iii) The intensities of He II λ 4686 and the Balmer lines are also modulated with a period near ∼ 1152 s, in phase with a continuum modulation at the same period.

(iv) Orbital modulations in intensity and V/R ratio are observed in the Balmer lines, but no S-wave is apparent. The He II λ 4686 line shows only a weak variation in its intensity on the binary cycle, but the He II λ 4686 V/R ratio data are of insufficient quality to enable an analysis.

4.4 Discussion

4.4.1 Orbital effects

In §4.3.4 I showed that the Balmer lines suffer a redshift and a reduction in intensity near orbital phase 0.75 followed by a substantial blueshift ~ 0.05 orbital cycles later (see figure 4.12). These results resemble those expected from a partial eclipse of circulating material—a so-called 'rotational disturbance'. First the blueshifted side of a disc or ring is obscured by the secondary, resulting in a diminished line intensity and a reduced V/R ratio. Then, when the redshifted side begins to be eclipsed, the V/R ratio increases through unity, falling back to 'normal' after the eclipse. However, an eclipse of a disc or ring at this orbital phase (~ 0.75) makes it difficult to understand how optical photometric minimum arises at phase zero, a quarter of a cycle later. The photometric modulation is generally attributed to the varying aspect of a disc 'bright-spot' or the heated face of the red dwarf. If there is an eclipse at orbital phase 0.75, then at phase zero the line joining the two stars will be nearly perpendicular to the line-of-sight, and the secondary will be moving away almost with maximum radial velocity. Thus, no minimum would be expected at this phase from the standard varying aspect interpretation.

An optical and X-ray orbital modulation with this phasing *might* arise if the accretion stream skips over a disc to impact directly on the surface of the white dwarf in the form of discrete blobs (a similar situation was proposed by McHardy et al. 1987, but without any accretion disc at all). The optical photometric, line intensity, and X-ray orbital modulations are then caused by the varying aspect of this region of enhanced emission—fixed in the binary frame—on the white dwarf's surface. However, two X-ray dips are observed per orbital cycle in BG CMi (NMLW), separated by 0.5 in phase. More importantly, the X-ray dips are energy dependent, and are therefore inconsistent solely with a simple occultation (see chapter 2). Therefore, the phasing suggested by an eclipse interpretation cannot be correct because it does not account for the X-ray orbital modulation. A further interpretation must

be sought.

In intermediate polars which *do* exhibit eclipses it is generally found that the X-ray dips occur 0.0–0.2 binary cycles prior to inferior conjunction of the secondary (see chapter 2). If one assumes a similar phasing for the dips in BG CMi, then the secondary is expected to be at inferior conjunction near orbital phase 0.0–0.2. This favours the usual interpretation that the optical orbital modulation is caused by the varying aspect of a disc bright-spot or the heated face of the red dwarf. In the case of a disc bright-spot an orbital S-wave would be expected in BG CMi, as is seen in other systems. An S-wave might arise alternatively from the varying aspect of a magnetospheric impact region. Indeed, an orbital S-wave is observed in unpublished data from BG CMi (C. Hellier, private communication); however, the latter results obviously differ from those in this thesis, where no such S-wave is observed. A similar null result is found by Mouchet (private communication). These discrepancies are not understood. In any case a phasing of inferior conjunction at orbital phase 0.0–0.2 cannot account for the apparent rotational disturbance at orbital phase 0.75 exhibited by the current data if the disturbance is caused by an eclipse of a ring or disc by the secondary.

The key to understanding the orbital modulation of the emission lines in any system is a knowledge of the presence or absence of an accretion disc. However, the presence of a disc has been mooted since McHardy et al. (1987) proposed a discless model following their analysis of *EXOSAT* data. The question is still open because the clues that do exist have ambiguous interpretations. For example, the He I and H I lines are double-peaked: this may be taken as evidence for circulating material, but could also be caused by absorption in the line centres.

In summary, I can find no explanation for the inconsistency of the current data with previously published and unpublished data, and merely reiterate that the data in figure 4.12 do contain a phenomenon which resembles a, probably transient, rotational disturbance.

4.4.2 On the nature of the $\sim$1152 s period

Both the photometry (chapter 3) and spectroscopy of this system exhibit a phase-correlated modulation at a period near 1152 s. An independent detection of this period has been made with optical photometry (T. Augusteijn, private communication). This pulsation is probably transient, or at least unstable, as it is not observed in all photometric data which have been published on BG CMi. PT have indicated that a period of 1083.5 s might be expected in the event that the spin period (frequency ω) is 913 s: a 1083.5 s period then arises from the natural couple $\omega - 2\Omega$ (where Ω is the orbital frequency). A formal error on the 1152 s period cannot be estimated using the ratio-test period-search. However, figure 4.8(c) shows that the period near 1152 s is likely to be too far away to be comfortably associated with 1083.5 s. The exact value of the 1152 s period has to be determined before this or any other interpretation can be considered in detail. Until then, the nature of the $\sim$1152 s period remains a mystery.

4.4.3 Which is the true spin period?

4.4.3.1 A 913 s spin period?

The analysis I have presented has clearly demonstrated a V/R ratio modulation in the emission line wings of BG CMi at a period consistent only with the known 913 s variation. This provides strong evidence that the spin period of the white dwarf (P_{spin}) is 913 s and, indeed, further evidence in favour of this interpretation exists. For example, the V/R ratio 913 s-profile (see figure 4.7) is quasi-sinusoidal and has its maximum at maximum photometric 913 s pulse flux. This, in turn, is in phase with the line intensity variation (figure 4.11), and is approximately[1] in phase with the X-ray pulsation at the same period (NMLW). In other words, the behaviour of the 913 s pulse in BG CMi is reminiscent of the *spin*-pulse behaviour in other intermediate polars where spin phase-resolved spectroscopy has so far been

[1]The X-ray pulse is complex rather than a simple sinusoid (Norton et al. 1992b).

obtained (e.g., EX Hya [Hellier et al. 1987], FO Aqr [Hellier, Mason & Cropper 1990], and AO Psc [Hellier, Cropper & Mason 1991]; GK Per is an exception—see chapter 5). Thus, the V/R ratio data imply that a significant fraction of the accreting, radiating material is locked to the rotating magnetic field, compatible with, for example, the curtain-type flows of Rosen, Mason & Córdova (1988, hereafter RMC), and strongly suggest that 913 s is the true spin period.

However, the situation is not this simple. The data here support the presence in this system of the 847 s period seen in medium-energy X-rays: it is present in the line intensities, and in their equivalent widths (see figure 4.11[b]). The 847 s period is not, however, observed in the V/R ratio and, because it is manifest purely as an intensity variation, it probably cannot be caused by inflowing or circulating material. Thus, under the assumption that 913 s is the spin period, as the V/R ratio data imply by comparison with other intermediate polars, the most obvious way to generate the 847 s period is by invoking retrograde rotation of the white dwarf. This period then becomes a positive orbital sideband, caused by reprocessing and reflection off structures fixed in the binary frame, such as the secondary or a disc bulge (if present). The problems with this interpretation, as pointed out by NMLW, are obvious. It is not known how or why the white dwarf might rotate against the orbital motion. Moreover, the white dwarf in BG CMi is spinning up (see chapter 3). Thus, not only is the primary required to be spinning in the 'wrong' direction, but some agent must act to increase its angular velocity. The two torques acting here which will influence the spin period are a 'matter' torque exerted by the accreting material as it attaches to magnetic field lines, and a drag torque due to the magnetic stress which the field exerts on the accretion stream or disc (see Ghosh & Lamb 1978, 1979a, 1979b; see also Ghosh, Lamb & Pethick 1977). If the white dwarf is spinning in a retrograde manner, both of these torques will be negative, leading to a spin-*down*. Furthermore, as already commented (e.g., NMLW, Wynn & King 1992), it is likely that the combination of a 30% X-ray albedo, and the low solid angle subtended at the white dwarf by a candidate

reflection site, will produce much less power in the reflected signal than is actually observed. Obviously, therefore, the retrograde rotation and reflection/reprocessing scenario is not an acceptable interpretation.

Clearly if 913 s is the spin period, the only alternative is to generate the 847 s period in some other way. However, it is very difficult to imagine geometries, other than the above, which will produce a positive sideband period. A 913 s spin period in a system with *no* disc would give rise to a 991 s X-ray and optical period according to the model of NMLW (see §1.5.4.2 and §4.4.3.3). This period has not been seen in BG CMi.

4.4.3.2 A 1827 s spin period (twice 913 s)?

The proposition that P_{spin} = 1827 s was advanced by PT as the 'minimum novelty' interpretation of their power spectra (from optical photometry). The authors suggested that accretion was occuring equally onto both magnetic poles (i.e., disc-fed accretion), both of which were visible. What the authors neglected to state, however, is that this only gives rise to an X-ray period at 913 s if the system inclination, and the co-latitude of the poles, are both high (Wynn & King 1992). In this situation, illustrated in figure 4.14, maximum flux is seen when the observer's line-of-sight is perpendicular to both curtains simultaneously (i.e., when viewing perpendicularly to the diagram). This occurs twice every spin period (once every 913 s). The intensity when the poles are aligned with the observer's line-of-sight will depend on the structure and visibility of the accretion shocks near the white dwarf's surface, but it is likely that a minimum will be observed when the upper pole points towards the observer.

Interestingly enough, this model might actually be capable of producing an apparent V/R ratio modulation at 913 s, and its associated 'redness' (see figure 4.7). The latter arises because when the poles are aligned with the observer's line-of-sight, the accreting material is always seen to be moving away, towards the poles, almost parallel to the line-of-sight. A quarter of a spin cycle later, when the sides

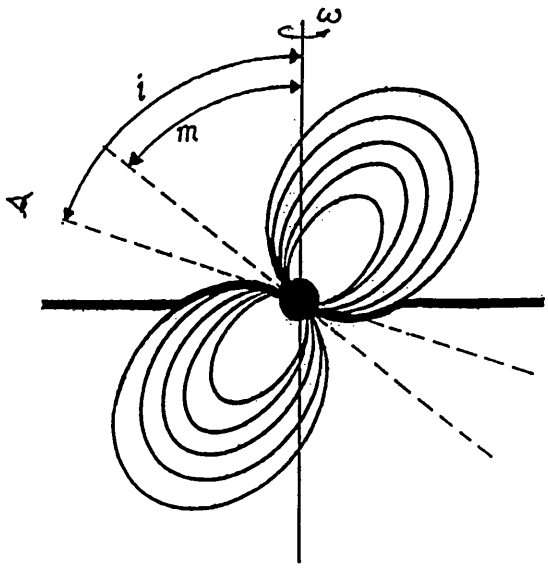

FIGURE 4.14: *Schematic representation of a disc-fed accretion scenario in an intermediate polar of high inclination, i, and high magnetic pole co-latitude, m. When viewing perpendicularly to the page maximum X-ray and optical flux is observed along with a low radial velocity. This will occur twice every spin cycle.*

of the curtains are exposed, the redshift vanishes, and the V/R ratio retains a value near unity. Thus, this situation is expected to produce two maxima (V/R ratio $\simeq 1$) in the V/R ratio every spin cycle (i.e., one every 913 s), coinciding with maximum X-ray and optical intensity. This describes the modulation seen in figure 4.7 very well.

The problem with this interpretation is again the 847 s period. In fact, it is even harder to generate this period in the current scenario than it is with the model in §4.4.3.1.

4.4.3.3 An 847s spin period?

The values of the X-ray periods in BG CMi, 913 s and 847 s, and their relationship with the orbital period clearly shows that one must be a beat period. Yet, Norton (1993) has generated simple simulated X-ray lightcurves of intermediate polars

and concludes, as had been stated previously (Hellier 1991; King & Lasota 1991), that purely disc-fed systems do not permit X-ray modulation at *any* beat period (except by reprocessing). As discussed is §4.4.3.1, if there is a disc in BG CMi, it is indeed very difficult to produce a positive sideband period without invoking retrograde rotation. This led NMLW to propose a discless accretion model for BG CMi, in which the spin period is actually 847 s, with 913 s being the usual negative orbital sideband. I have discussed this model in §1.5.4.2 (see also Norton et al. 1992a, and Wynn & King 1992). In brief, that magnetic pole which is nearer to the inner Lagrangian point will preferentially accrete. This will switch over, so that the opposite pole becomes active, half a beat cycle later. The switching mechanism is likely to be gradual rather than instantaneous, and it is possible that two poles will be simultaneously active for at least part of the beat cycle. This is an intriguing possibility, but, like the accretion curtain models, this picture faces difficulties when confronted with the data presented here.

(i) NMLW suggested that a residual accretion curtain might be present in BG CMi which may explain the 847 s X-ray period. Therefore, if the spin period is 847 s, and if there is a curtain-type flow, a V/R ratio variation at this period should be, but is not, observed.

(ii) If 913 s is the beat period, it is not understood how the V/R ratio behaviour at this period, and its phasing with respect to the optical and X-ray pulses, is identical to that seen in other intermediate polars at their *spin* periods. In fact, it is difficult to imagine what V/R ratio *beat* modulation, if any, would result from the discless model of NMLW; depending on the orbital phase, the radial velocity of material on the field lines can be either positive or negative at the same beat phase (see figure 1.4). However, it is conceivable that a V/R ratio modulation at the beat period will be observed on a timescale of a few spin/beat cycles. The behaviour of the radial velocity in this model is crucial to the complete understanding of this scenario, and needs to be investigated in simulations before one may state unequivocally that no V/R ratio modulation at the beat period is expected. This

work is beyond the scope of this thesis. Until then, this second point must be regarded with caution.

(iii) One final point concerns the *Ginga* BG CMi data (NMLW). NMLW's figure 3, showing the X-ray data folded on the proposed beat period (913 s), demonstrates that the pulse is not a simple sinusoid. It has at least two maxima and minima per cycle. However, the simulations of Norton (1993), wherein theoretical beat-pulse and spin-pulse profiles are investigated for various accretion scenarios, do not predict a complex beat-pulse profile for the model of NMLW. The simulations often show a complex spin-pulse, but the beat-pulse is nearly quasi-sinusoidal, or at least single-peaked, *in all cases shown*. It may be possible to produce the required non-sinusoidal X-ray beat-pulse in the event that the properties of the magnetic poles differ from each other, for example, in size, shape, or emission rate, or if the poles are not separated by exactly 180° (A. Norton, private communication). Obviously, it is very likely that many, if not all, of these effects will indeed contribute to the modulation pattern produced.

4.4.3.4 A 1693 s spin period (twice 847 s)?

This final possible interpretation was also proposed by PT because it is able to explain various peaks in their photometry power spectra. For example, their peak at 1714 ± 20 s is consistent with a period of 1693 s. In addition, if the system contains a disc, then reprocessing at a structure which is stationary in the binary frame produces a signal at a period of 1981 s, in agreement with one seen in their data at 1975 ± 7 s. However, this picture fails to explain the current data for much the same reason as the previous model: for example, the lack of a V/R ratio modulation at 1693 s.

4.5 SUMMARY OF CONCLUSIONS

To conclude, I summarise my findings as follows.

(i) An S-wave is not at all obvious from these data. However, substantial orbital modulation in the lines is observed; if an S-wave were present at the time of observation, it seems likely that it would have been detected. The line orbital modulation seems to imply a partial obscuration of circulating material, such as in a disc or ring, but the phasing of this phenomenon relative to the secondary cannot currently be determined.

(ii) The V/R ratio modulation and its phasing with respect to the line intensities and the continuum pulsations strongly implies that the true spin period of the white dwarf in this system is 913 s, and that the accretion occurs via the curtain-type flows of RMC. However, a disc-fed scenario such as this cannot account for the presence of the positive (therefore) orbital sideband at 847 s.

(iii) An 847 s spin period at first seems excluded for two reasons. Firstly, there is no detection of a V/R ratio modulation at this period. Secondly, a 913 s V/R modulation like the one observed probably would not arise in the discless scenario proposed by NMLW. However, until the exact velocity pattern expected according to that model is investigated, it would be unwise (considering the inability of a curtain-type model to otherwise explain the results) to dismiss the possibility that 847 s is the true spin period.

Overall, these results are somewhat paradoxical: a 913 s modulation which suggests the presence of a disc; and an 847 s period, proving that a beat period exists thus favouring a discless scenario. The uncertainty over the spin period and the geometry in BG CMi therefore still looms, and will not be removed until further analysis is undertaken. For example, a more detailed set of spin-resolved spectroscopy would help establish whether the 847 s period—present in the line intensities and equivalent widths—is confined to the core, the wings, or both, narrowing down the possible causes of such modulation. Similarly for the 913 s intensity variation. Another useful exercise would be to model the radial velocity variation in a discless scenario such as that of NMLW. A simulation for line emission in the

curtain-type flows of RMC has already been published (Ferrario, Wickramasinghe & King 1993), but in the discless model, where the behaviour of the radial velocity (or V/R ratio) as a function of spin/beat/orbital phase is not intuitively obvious, this has yet to be attempted.

5. GK PERSEI: THE ACCRETION GEOMETRY

There is no 'royal road' to geometry.

Euclid
Comment by Proclus (c. 300 B.C.)

5.1 INTRODUCTION

GK Per is one of the more obscure members of the cataclysmic variable class of objects. Since this object first announced its presence as Nova Per 1901, it has continued to provide a wealth of interesting surprises.

The first oddity which stood GK Per apart from other classical novae was its peculiar spectrum, which exhibits strong absorption features as well as the usual emission lines which were known at that time to characterise such objects. After the 1901 eruption the visual magnitude suffered irregular, low-amplitude (± 0.5 mag) fluctuations (Kim, Wheeler & Mineshige 1992, hereafter KWM). Then in 1948 GK Per unexpectedly flared-up again; however, this time the system underwent a dwarf nova outburst (Bianchini, Sabbadin & Dalmeri 1986). Since that time, approximately 20 dwarf nova-type outbursts have been recorded from this system, with variable duration and amplitude (Sabbadin & Bianchini 1983).

In 1979 the *Ariel V Sky Survey Instrument* (Cooke et al. 1978) detected an outburst in X-rays from GK Per (King, Ricketts & Warwick 1979). Subsequent X-ray observations have been reported (e.g., Córdova, Mason & Nelson 1981, Becker &

Marshall 1981), but to date the most significant of these remains the 1983 *EXOSAT* observation whilst the system was in outburst; during this observation a coherent, hard (> 2 keV) X-ray pulsation with a period of 351 s was discovered (Watson, King & Osborne 1985). This established GK Per as a member of the intermediate polar subclass of magnetic cataclysmic variables. Further X-ray observations in quiescence (Norton, Watson & King 1988; Eracleous, Patterson & Halpern 1991; Ishida et al. 1992, hereafter I92) have since confirmed this discovery.

A further remarkable feature of GK Per is its orbital period, which is atypically long amongst cataclysmic variables. Originally, Kraft (1964) suggested a binary period of 1.904 d and a high orbital eccentricity (0.4). However, this very lengthy orbital period was extremely controversial, and a circular orbit with a period of 0.685 d, calculated by Paczynski (1965) from a re-analysis of Kraft's data, was most favoured at the time. This issue was not resolved until Bianchini, Hamzaoglu & Sabbadin (1981) established from radial velocity measurements of the Hα line that Kraft's original result was in fact closer to the true orbital period, and that Paczynski's determination was incorrect. The most recent estimate is a 1.996803 ± 0.000007 d period with a circular orbit (Crampton, Cowley & Fisher 1986, hereafter CCF). This orbital period is almost unrivalled in duration by that of any other cataclysmic variable. The exceptions are U Sco with a period of 1.23 d (Ritter 1990), and possibly the remnant of Nova Sgr 1919 with a 5.7 d orbit (Sekiguchi 1992).

Classical nova, dwarf nova, intermediate polar—despite this interesting mix of characteristics, GK Per remains ill-studied in at least one important respect: to date, high time-resolution spectroscopy has not been published on this system. Hutchings & Cote (1986) did report spin phase-resolved spectroscopy, but their data were so limited, and the time resolution so coarse, that very little information was obtained. Hutchings & Cote's paper did establish, however, that radial velocity and equivalent width spin modulations were evident in GK Per. To examine this more closely, I present the first detailed analysis of spin phase-resolved opti-

cal spectroscopy of this system. Similar studies of other intermediate polars (e.g., Hellier, Mason & Cropper 1990, Hellier, Cropper & Mason 1991, and Hellier et al. 1987) have proven invaluable in probing the accretion geometry in this subclass. GK Per is particularly interesting in this regard because its long orbital period means that it is the only intermediate polar where the presence of an accretion disc is essentially incontestable. GK Per is therefore an ideal testing ground for the accretion curtain model of Rosen, Mason & Córdova (1988, hereafter RMC; see §1.5.4.1). The analysis of the present data confirms that the spectrum is indeed spin-modulated; but—as is perhaps to be expected of a system as unique as GK Per—the results are not typical of those observed in other intermediate polars.

5.2 Observations

The data were obtained at La Palma using the two-arm Intermediate-dispersion Spectroscopic Imaging System on the William Herschel Telescope. GK Per (a secondary target) was observed in 1991 on December 15 and 16. A 316R grating was used on the red arm (giving a reciprocal dispersion of 1.4 Å pixel^{-1}), and 600B was used in the blue (0.7 Å pixel^{-1}). The spectral ranges covered were not the same on both nights owing to an error in the grating angles that were used. On the first night the ranges 6600–8300 Å and 4000–4900 Å were observed with the red and blue arms respectively. On the second night the ranges observed were primarily 5600–7300 Å and 3340–4240 Å, covering the Hα line and the region bluewards of the Balmer limit; however, for the last 16 blue spectra the grating angle was reset to cover the same range as on the first night. Most of the spectra (a total of 99 from each arm) were acquired with a 30 s integration period; however, for the first pair of spectra taken on December 15 the integration time was 120 s on each arm. In total, approximately 12 and 24 spin cycles were observed on the first and second nights respectively. These observations are summarised in table 5.1.

As in the case of BG CMi (chapter 4) the CCD detectors (EEV5) were 'windowed' such that a region on each measuring 1270 by 57 pixels was used, and

Date (1991)	Red arm (316R) λ range (Å)	No. of spectra	Int. (s)	Blue arm (600B) λ range (Å)	No. of spectra	Int. (s)
December 15	6600–8300	1	120	4000–4900	1	120
	6600–8300	34	30	4000–4900	34	30
December 16	5600–7300	64	30	3340–4240	48	30
				4000–4900	16	30

TABLE 5.1: *GK Per spectroscopy observing details.*

on-chip binning by a factor of three was enabled in the spatial direction for speed of readout. Flux standards were also observed on both nights; however, conditions were non-photometric, so I have used the standard star observations purely to facilitate the instrumental response correction.

5.3 DATA ANALYSIS

5.3.1 EMISSION LINE SPECTRUM

Figures 5.1(a)–(d) show the co-added spectra from both nights in all wavelength regions observed. Atmospheric standards were not observed, so I was unable to remove the atmospheric absorption bands from the red spectra. Owing to the very small range of orbital phase sampled on each night (~ 0.023 orbital cycles on the first night and ~ 0.007 on the second), orbital phase-related changes between spectra observed on any one particular night are negligible, and no correction for the orbital motion of the individual spectra was necessary before co-adding them. However, only the first night's blue spectrum is shown in figure 5.1(b) because the orbital phase is 0.5 cycles different on the second night.

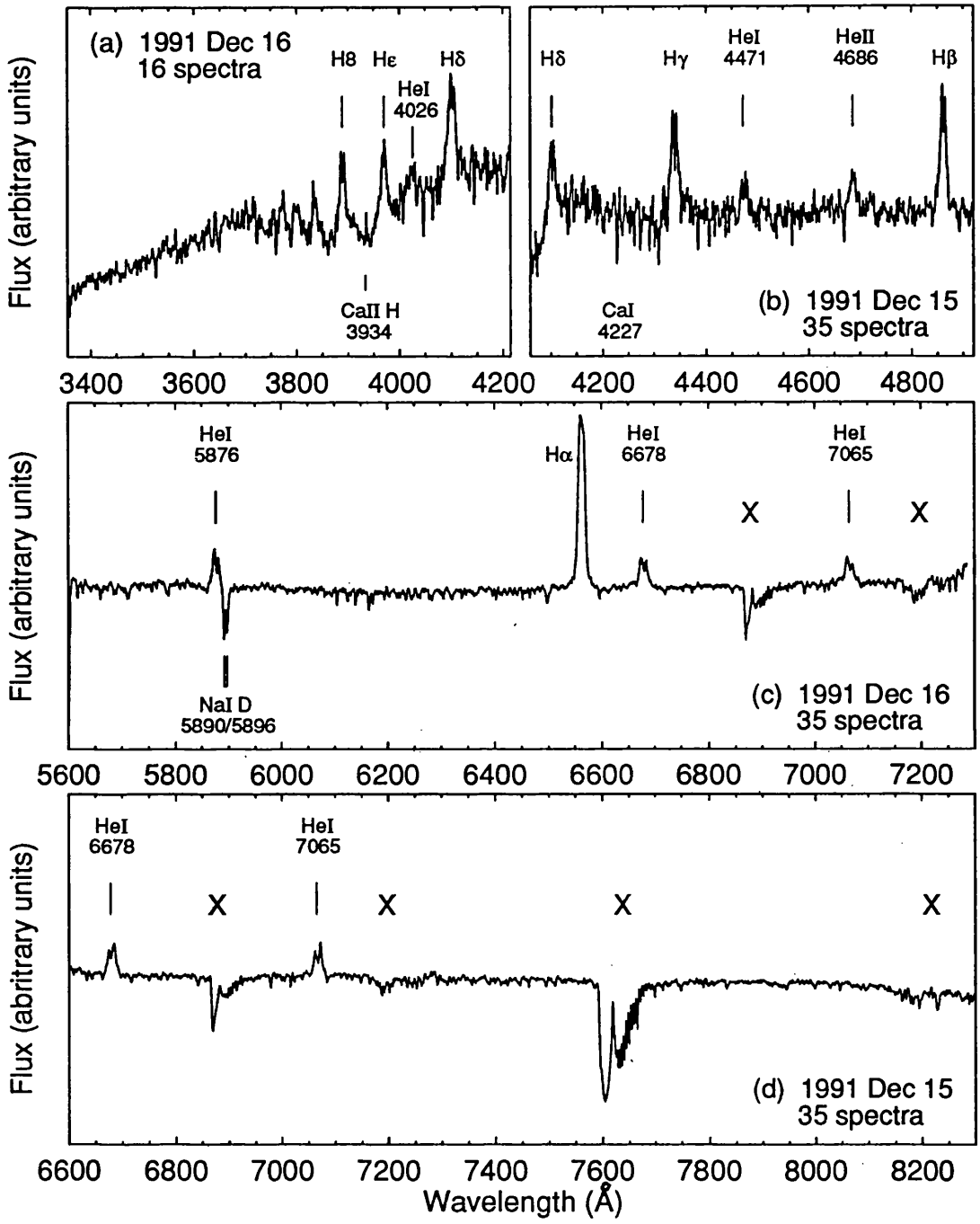

FIGURE 5.1: *The mean spectrum of GK Per as observed on both nights (1991 Dec 15 and 16). All spectra have been corrected for instrumental response except (a); no flux standard was observed in this wavelength region. Flux units are arbitrary because the observing conditions were non-photometric. The Xs indicate absorption features formed in the Earth's atmosphere.*

The spectrum contains the usual wide (full-width at zero intensity [FWZI] $\sim$ 1800 km s^{-1}) neutral helium, singly ionised helium, and hydrogen Balmer emission lines. It also shows narrow Ca II λ 3934 (Ca II H) emission (first noted by Gallagher & Oinas 1974). Interestingly, the Hα line does not have a double-peaked profile, whereas all other Balmer lines observed do. This is not likely to be an orbital phase-related phenomenon because the other Balmer lines (Hβ–Hδ, hereafter referred to as the blue Balmer lines) exhibit a double-peaked structure on *both* nights. The mean velocity-separation of the H I line peaks—which does not change noticeably from one night to the next—is 402 ± 54 km s^{-1} (1σ standard deviation), consistent with the result (~ 350 km s^{-1}) of CCF. The He I lines exhibit double peaks separated by 409 ± 33 km s^{-1}. This is somewhat less than the ~ 550 km s^{-1} reported by CCF, but is in excellent agreement with the separation of the H I peaks. Thus, H I and He I may originate in the same region. In contrast to the He I and the blue H I emission lines, He II λ 4686 does not have a double-peaked profile. This has been noted in previous non-outburst spectra (e.g., CCF, Hutchings & Cote 1986).

	Orbital phase $\simeq 0.7$ (day 1)	Orbital phase $\simeq 0.2$ (day 2)
I(Hα)/I(Hβ)	—	1.70 ± 0.30
I(Hγ)/I(Hβ)	0.97 ± 0.16	1.13 ± 0.22
I(Hδ)/I(Hβ)	0.69 ± 0.20	0.90 ± 0.22

TABLE 5.2: *Emission line strengths, relative to Hβ, in GK Per.*

In table 5.2 I show the mean intensities of the Balmer lines normalised to Hβ on each night. Note that *relative* line fluxes are not affected by the non-photometric observing conditions. The line intensities in all spectra on each night were calculated by summing the area under each line (above the continuum), assuming a

FWZI of 1800 km s^{-1}. Then I obtained the mean intensity of each line for each night, enabling the ratios in table 5.2 to be calculated. The results on both nights are in agreement within the quoted errors (1σ standard deviations). As is usual for intermediate polars, the Balmer decrement is flatter than that expected from pure Case A (optically thin in all lines) or Case B (optically thin to all except Lyman photons) radiative recombination (e.g., Brocklehurst 1971). This suggests that the line emission region is bathed in a dense photon field (Elitzur et al. 1983), and/or, as proposed by Anupama & Prabhu (1993), that inelastic electron-atom collisions are important (see Adams & Petrosian 1974). These issues will be discussed in §5.4.1.1.

5.3.2 Secondary star spectrum

In addition to the emission features, the spectrum of GK Per contains absorption lines characteristic of a late-type star near spectral type K. Lines present in the absorption spectrum include those of Ti II, Sr II, Cr I, and Ca I, as well as numerous lines of Fe I. According to the ephemeris of CCF, the orbital phase ranges covered by the spectra in this chapter are 0.681–0.704 on the first night and 0.198–0.205 on the second night ($\pm$0.019). These are close to the inferior and superior conjunctions of the secondary star (0.75 and 0.25 respectively), and are similar to those phases observed by CCF (0.8 and 0.3). As CCF's orbital ephemeris is based upon radial velocity measurements taken between seven and thirteen years ago, I have investigated its correctness at the epoch of the current data. This was achieved by measuring the radial velocities of the strongest absorption lines seen in the spectrum and plotting these, along with the mean absorption line velocities tabulated by CCF, folded according to their ephemeris. The observed velocities are given in table 5.3, along with the 1σ standard errors, and the folded radial velocity data are shown in figure 5.2. As can be seen from the latter figure, the newly calculated radial velocities are fully consistent with the ephemeris. Note that given the scatter in figure 5.2, the velocity of the Ca II H emission line which is visible at orbital

Line	December 15 Wavelength (Å)	December 15 Velocity ($km\,s^{-1}$)	December 16 Wavelength (Å)	December 16 Velocity ($km\,s^{-1}$)
Fe I λ4198.30	4198.4	−7.1	4199.7	+100.0
Fe I λ4202.03	4201.9	−9.3	4203.3	+90.6
Sr II λ4215.52	4215.7	−12.8	4216.6	+76.8
Ca I λ4226.73	4226.5	−16.3	4227.6	+61.7
Fe I λ4260.47	4260.4	−4.9	4261.9	+100.6
Fe I λ4271.76	4271.6	−11.2	4273.2	+101.1
Fe I λ4404.75	4404.6	−10.6	4405.9	+78.3
Fe I λ4415.12	4415.0	−8.1	4416.5	+93.7
Fe I λ4891.49	4891.2	−17.8	4892.9	+86.4
Na I λ5889.95	Not observed		5891.5	+78.9
Na I λ5895.93	Not observed		5897.5	+80.1
Mean		-11 ± 4		$+86 \pm 12$

TABLE 5.3: *Velocities of absorption lines from the secondary.*

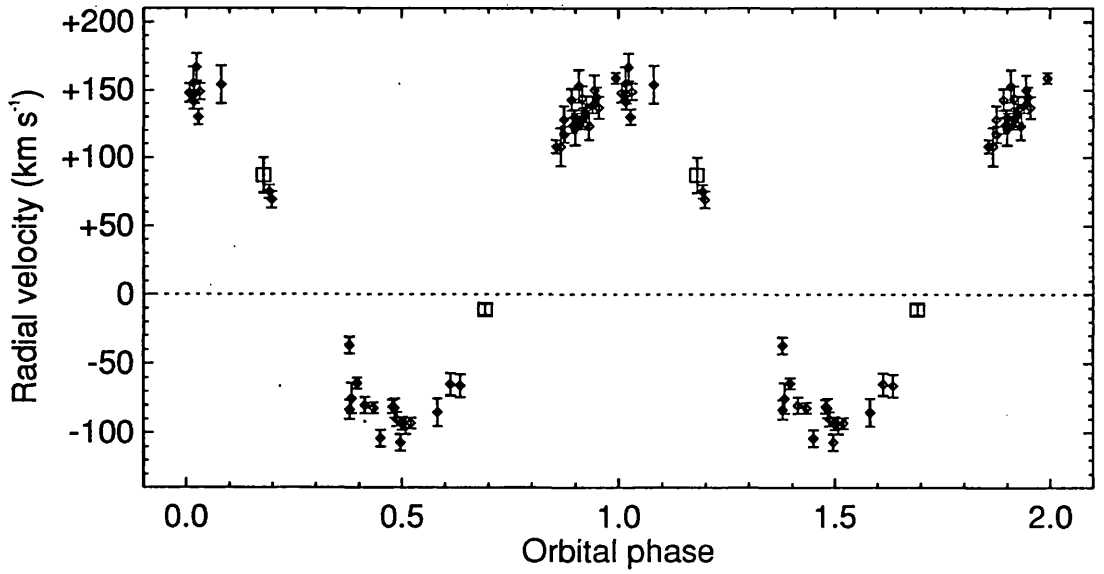

FIGURE 5.2: *Absorption line radial velocity curve of GK Per, showing two new radial velocity measurements (squares), and the radial velocity data of Crampton, Cowley & Fisher (1986), folded according to their ephemeris. Two cycles are shown for clarity.*

phase 0.2—measured as $\sim +100\,\mathrm{km\,s^{-1}}$—indicates that this line might arise in the atmosphere of the secondary star.

Figure 5.3(a) shows a close-up of the mean spectrum observed on both nights. The secondary in GK Per is known to be a K-star, but its precise spectral type and luminosity classification is uncertain. Kraft (1964) measured the luminosity class to be between V and III, and observed conflicting features consistent with a spectral type between G8 and K5; he adopted K2 IV p as an average. Similarly, Gallagher & Oinas (1974) found that some of their spectra indicated a G8-type star, whilst others were consistent with a star of type K1–K2. The luminosity class, based on the strength of the Sr II λ 4216 line, was estimated as being between IV and V, and an average classification of K2 V–IV p was adopted. More recently, CCF suggested K0 V p. To obtain a further estimate of the classification of the secondary star, I have obtained a series of G-star and K-star spectra of varying luminosity type from the DIPSO database of ATLAS spectra (Kurutz 1979) for use as comparisons. These are displayed in figures 5.3(b) and (c), at the same reciprocal dispersion ($1.4\,\mathrm{\AA\,pixel^{-1}}$) as the GK Per spectra in figure 5.3(a).

5.3.2.1 Spectral type

From figure 5.3(b) it is clear that the depth of the Ti II λ 4290 line becomes comparable to that of the G band of the CH molecule towards later spectral type. Taken on its own, this simple diagnostic suggests that the spectrum of GK Per is approximately K2 at both orbital phases observed here. A further indication of the spectral type is given by the relative depths of Fe I λ 4260 and Fe I λ 4250, with the latter being strongest in stars of spectral type later than K0. However, Fe I λ 4260—*not* Fe I λ 4250—is strongest at *both* orbital phases in GK Per. This is obviously in conflict with the result of the previous test. As a compromise I adopt a spectral type of K0.

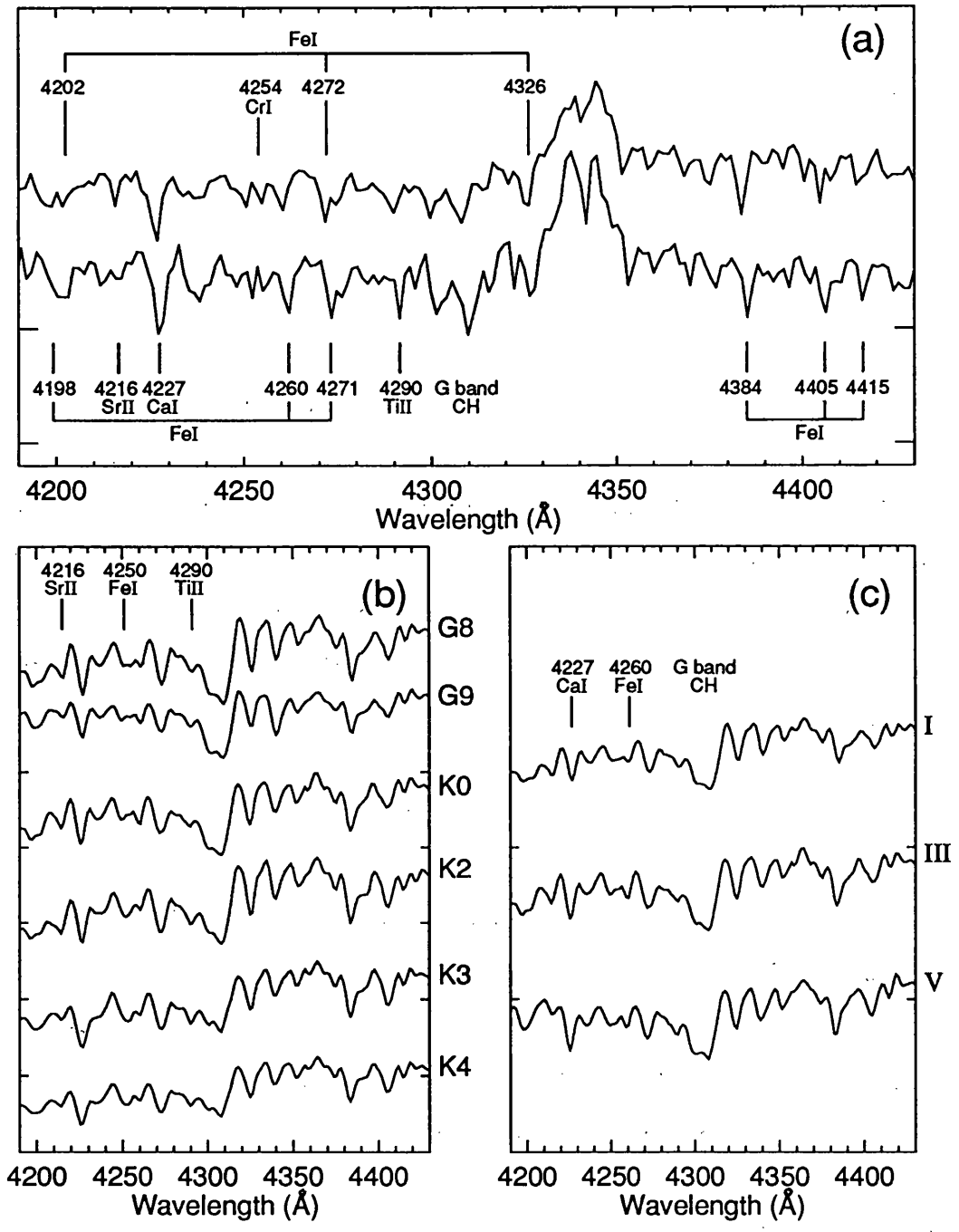

FIGURE 5.3: *(a) Close-up of the mean spectrum of GK Per observed at orbital phases 0.7 (upper spectrum) and 0.2 (lower spectrum). (b) The change in spectrum of a late-type star of luminosity class III as a function of spectral type. (c) The change in spectrum of a star of type K0 as a function of luminosity class. Tick marks on the y-axes indicate the zero levels for each spectrum.*

5.3.2.2 Luminosity class

To determine the luminosity class I have investigated the strength of Sr II λ4216 relative to Ca I λ4227, and Sr II λ4077 relative to Fe I λ4063 (Jaschek & Jaschek 1990). In the top spectrum of figure 5.3(a), the depth of Sr II λ4216 relative to Ca I λ4227 indicates a luminosity class close to III for the secondary in GK Per. However, in the lowest spectrum the Sr II line is weaker, suggesting a luminosity nearer to V. A similar trend is indicated by the relative strengths of Sr II λ4077 and Fe I λ4063 (not shown in this plot). Note that this is in contrast to the results of CCF where the Sr II lines were weak or absent at *both* orbital phases they observed. However, it should be observed that the spectra in figure 5.3(a) are comprised of a different number of individual observations (35 in the upper spectrum compared with 16 in the lower), so their signal-to-noise ratios (S/N) differ from each other. In accordance with Kraft (1964), Gallagher & Oinas (1974), and CCF, the luminosity class is therefore judged to be between III and V.

5.3.3 The pulsational modulation

The emission lines of GK Per have been shown to vary in intensity, equivalent width, and radial velocity at the rotation period of the white dwarf (Hutchings & Cote 1986). Unfortunately, the very coarse time resolution of Hutchings & Cote's data precluded a detailed analysis, and little useful information was gleaned from the results. The work was further hampered by the lack then of a precise knowledge of the value of the white dwarf rotation period, so much so that even though the authors obtained two datasets only one day apart, the relative phase uncertainty of the spin-pulse between the two nights was $\pm$0.23. However, the spin period of GK Per is now known accurately from X-ray observations made using *Ginga* (I92), and the data reported here are of sufficient quality to enable a spin phase-resolved analysis of the Balmer lines of this star (the He I lines being too weak to permit a detailed analysis).

5.3.3.1 Equivalent width

I estimated, by eye, the velocity where the lines blend into the continuum as $\pm 900\,\mathrm{km\,s^{-1}}$ (FWZI $= 1800\,\mathrm{km\,s^{-1}}$), and used this throughout for the equivalent width calculations (see §A.4.5 for the techniques employed in this process). Figure 5.4(a) shows the results of a Fourier analysis of the Hα equivalent width data.

As the S/N in the other three Balmer lines is not as high as in Hα, I have constructed a timeseries from the mean equivalent widths of these lines, and the Fourier spectrum obtained from this dataset is shown in figure 5.4(b). Note that this latter Fourier spectrum was obtained only from the Balmer line data from the first night, to avoid the effects of aliasing (the inclusion of the second night's blue spectra does not significantly alter the Fourier spectrum).

Although containing large peaks due to noise and poor observing conditions, figures 5.4(a) and (b) each demonstrate the presence of power near the X-ray period, $351.3410(\pm 1)\,\mathrm{s}$ (from I92). In figure 5.4(c) I show the average of the two previous Fourier spectra. This diagram readily demonstrates the presence of the pulsational modulation in the equivalent width of the Balmer lines. A Fourier analysis of the He II λ 4686 line (not shown), in contrast, shows no equivalent width spin modulation, with a full amplitude upper-limit of 0.16 Å. This limit was obtained by adding sinusoidal tracers of varying amplitude to the He II λ 4686 equivalent width timeseries and observing at which amplitude the corresponding peak in the power spectrum is comparable to the power seen at the 351 s period.

To examine the morphology and phasing of the equivalent width modulation, I have folded the equivalent width Balmer line datasets according to the spin ephemeris of I92. Figures 5.5(a) and (b) indicate that a quasi-sinusoidal modulation is present in Hα, with similar variation in the blue Balmer lines. Note that (b) shows only the Balmer line data from the first night, so that their phasing may be compared with the Hα line data (second night). The phase difference between the best-fitting sinusoids on each night, 0.05 ± 0.06 cycles, is not significant, indicating that the spin period of I92 is probably correct. I henceforth take the X-ray

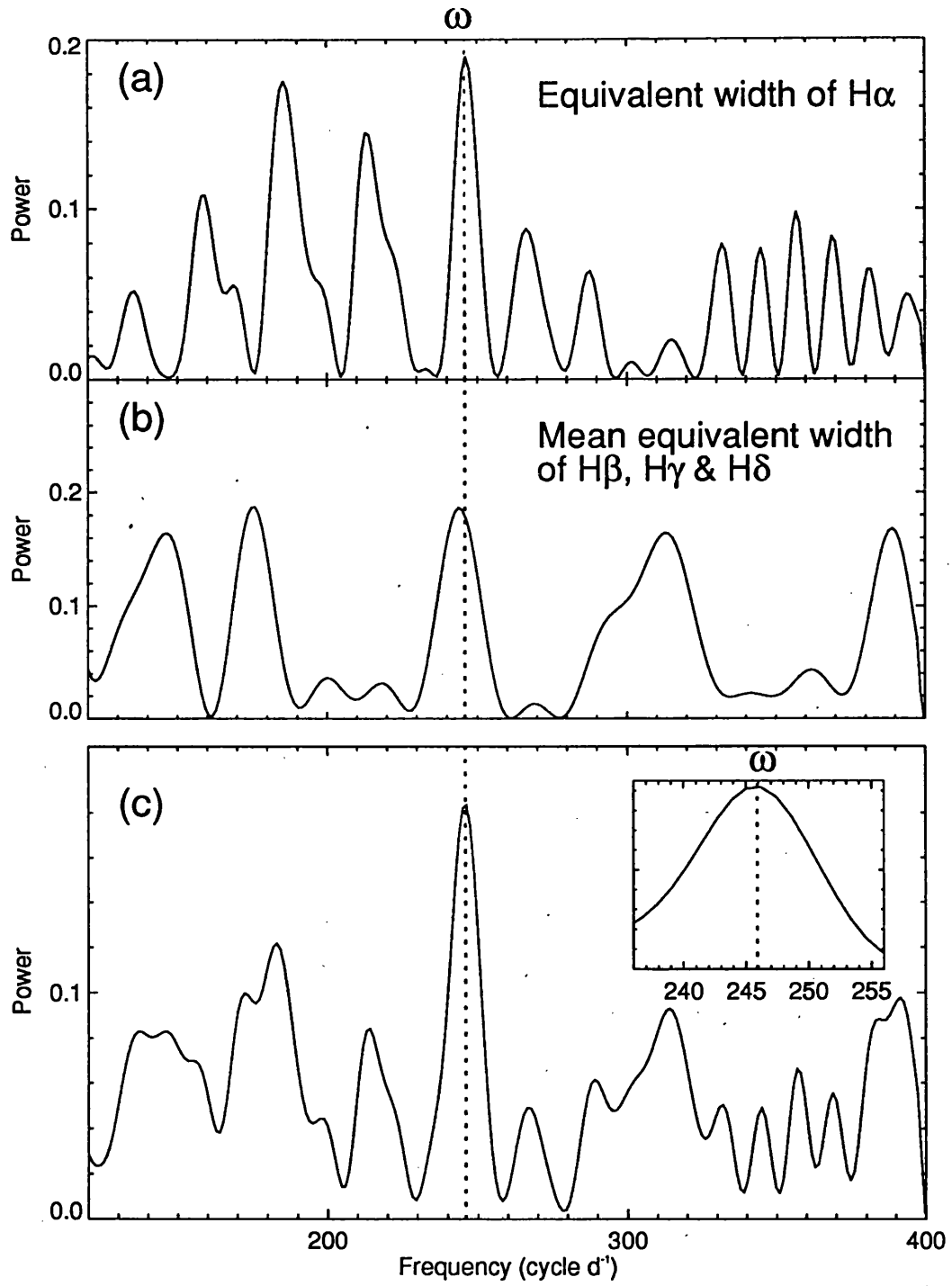

FIGURE 5.4: *A Fourier analysis of the Balmer line equivalent widths in GK Per. (a) shows the Fourier spectrum of the Hα equivalent width time-series, (b) shows the result obtained from the other three Balmer lines (first night only), and (c) shows the mean of (a) and (b).*

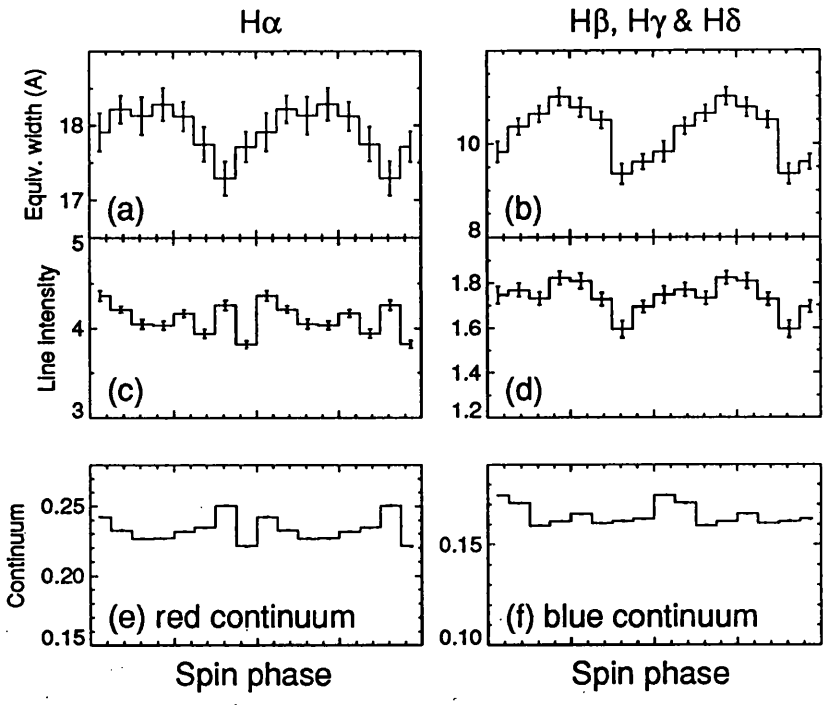

FIGURE 5.5: *The Balmer line equivalent width and line intensity, and the continuum level data, folded and rebinned according to the spin ephemeris of Ishida et al. (1992). Panels on the left contain data from the second night, and panels on the right contain data from the first night only. The units of the line intensities and continuum levels are arbitrary. Two cycles are shown for clarity.*

and equivalent width periods to be identical. The modulation of the Hα line equivalent width has a pulse-fraction (the ratio of the full amplitude of the best-fitting sinusoid to maximum intensity of that sinusoid) of $4 \pm 2\%$, compared to $13 \pm 2\%$ for the mean of the blue Balmer lines.

5.3.3.2 Line intensities and continuum level

By summing the counts in line-free (and atmospheric band-free) regions, the red continuum around Hα is seen to exhibit variations of up to 38% about its mean value, whilst the blue continuum shows similar correlated variability, but to a lesser degree ($\sim 20\%$). This variability is very erratic in both the blue and red spectra, and is ascribed to the presence of clouds during the observations. Figure 5.6(a), showing the continuum variation in the red region of the spectrum on the second

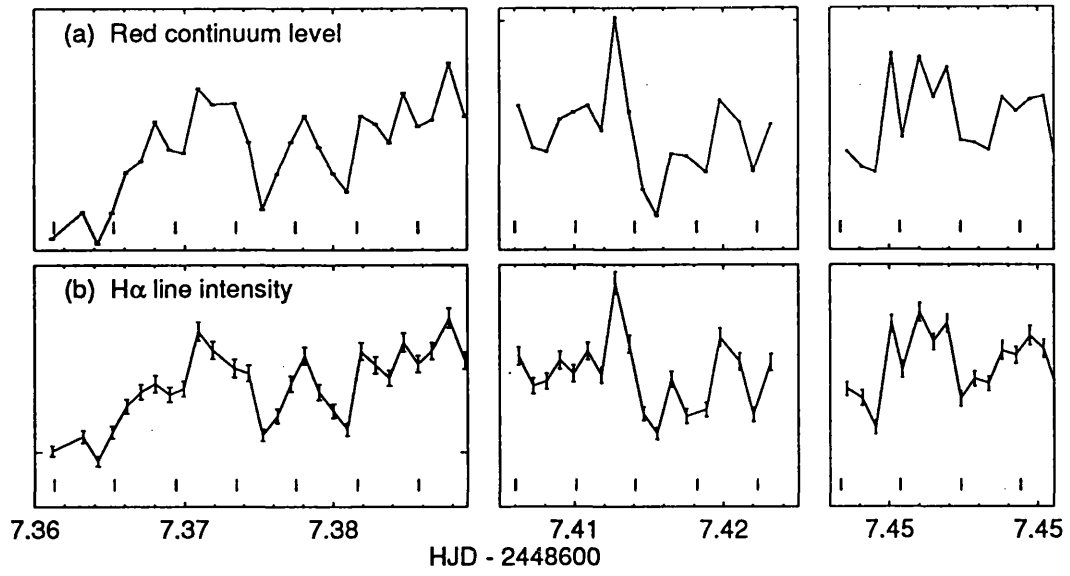

FIGURE 5.6: *Variations in the red continuum (second night) and the Hα line intensity. The ordinate scales are arbitrary. Tick marks indicate the times of minimum X-ray flux according to the spin ephemeris of Ishida et al. (1992). Error bars are included.*

night, demonstrates the variability. In addition, the continuum data are shown folded on the spin period in figures 5.5(e) and (f). No correlated variability is apparent: a Fourier analysis detects no significant power at a period of 351 s, with an upper-limit on the pulse-fraction of $\sim 7\%$ in both blue and red continua.

Figure 5.6(b) shows the variation of the Hα line intensity (i.e., the total area of the line above the continuum) as a function of time. Clearly the line intensity and continuum level exhibit correlated variations. Again, this is due to the non-photometric conditions. A similar result is obtained for the intensity of the other Balmer lines. The line intensity data are shown folded on the spin period in figures 5.5(c) and (d). A quasi-sinusoidal variation in the blue Balmer lines is apparent, with a pulse-fraction of $\sim 7\%$, in phase with the modulation of the equivalent width. The Hα line, by contrast, shows no evidence for a spin-modulation.

The fact that the mean blue Balmer line intensity pulse-fraction ($\sim 7\%$) is less than that of the mean equivalent widths of these lines ($\sim 13\%$), implies that the line intensity modulation cannot be the sole cause of the equivalent width variation, and

that the continuum must therefore contribute. This would appear inconsistent with the lack of a significant periodic continuum pulsation, but the calculated upper-limit on the latter of $\sim 7\%$ is just enough, when combined with the line intensity modulation, to produce the observed equivalent width pulsation. However, the continuum variation would have to be antiphased with respect to the line intensity variation, thus having maximum intensity near spin phase zero. As the ephemeris of I92 has minimum X-ray flux at phase zero, this implies that the X-ray pulsation may not be in phase with the optical one—in contrast to the behaviour usually seen in other intermediate polars—but this result cannot be tested owing to the lack of simultaneous X-ray and optical observations.

5.3.3.3 V/R ratio

To minimise the contribution of unmodulated line regions, I masked off regions of the lines between $\pm 200\,\mathrm{km\,s^{-1}}$ prior to calculating the V/R ratio, and thus considered only the wings (out to $\pm 900\,\mathrm{km\,s^{-1}}$). The data do not allow one to establish the limits of the modulated line components, so $\pm 200\,\mathrm{km\,s^{-1}}$ was arbitrarily chosen as a reasonable estimate. The appendix (§A.4.6) describes the techniques used for the V/R ratio calculation. Figure 5.7(a) shows the results of a Fourier analysis of the Hα V/R ratio data.

As the S/N in the blue Balmer lines is not as high as in Hα, I have added the blue contributions of each of these lines together, then repeated for the red components, before dividing the former by the latter to yield a mean V/R ratio timeseries. The same procedure was used in chapter 4. The Fourier spectrum obtained from this dataset (from the first night only, to avoid aliasing) is shown in figure 5.7(b).

Owing to the presence of noise in the data, these power spectra contain peaks at periods other than the spin period. However, figure 5.7(c), showing the mean of those power spectra in (a) and (b), does demonstrate the presence of the spin period in the V/R ratio of the line wings.

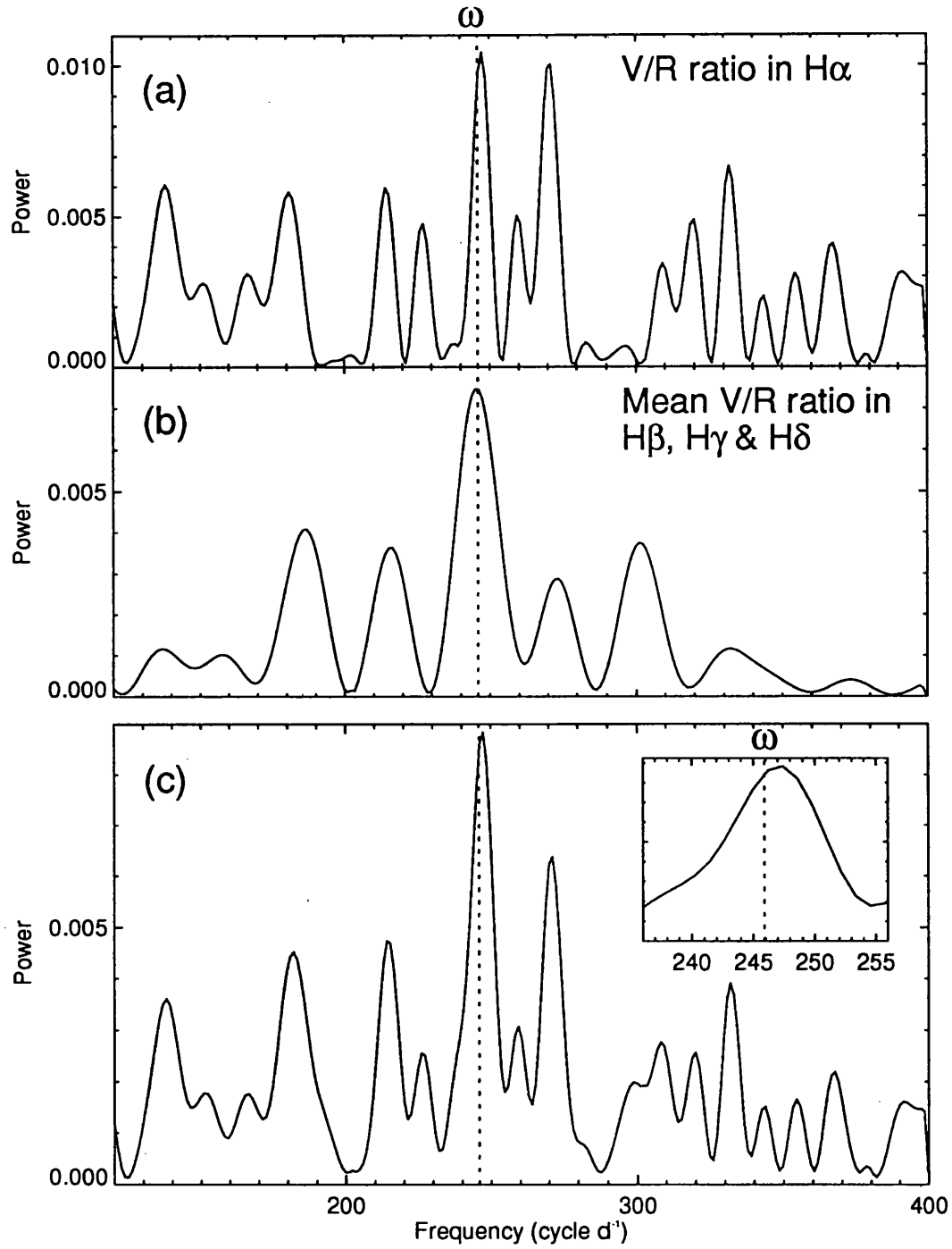

FIGURE 5.7: *Fourier spectra of the V/R ratio in the wings of the Balmer lines of GK Per. (a) shows the result of a Fourier analysis of the Hα V/R ratio dataset, (b) shows the result of a similar analysis of the blue Balmer lines (first night only), and (c) shows the mean of (a) and (b).*

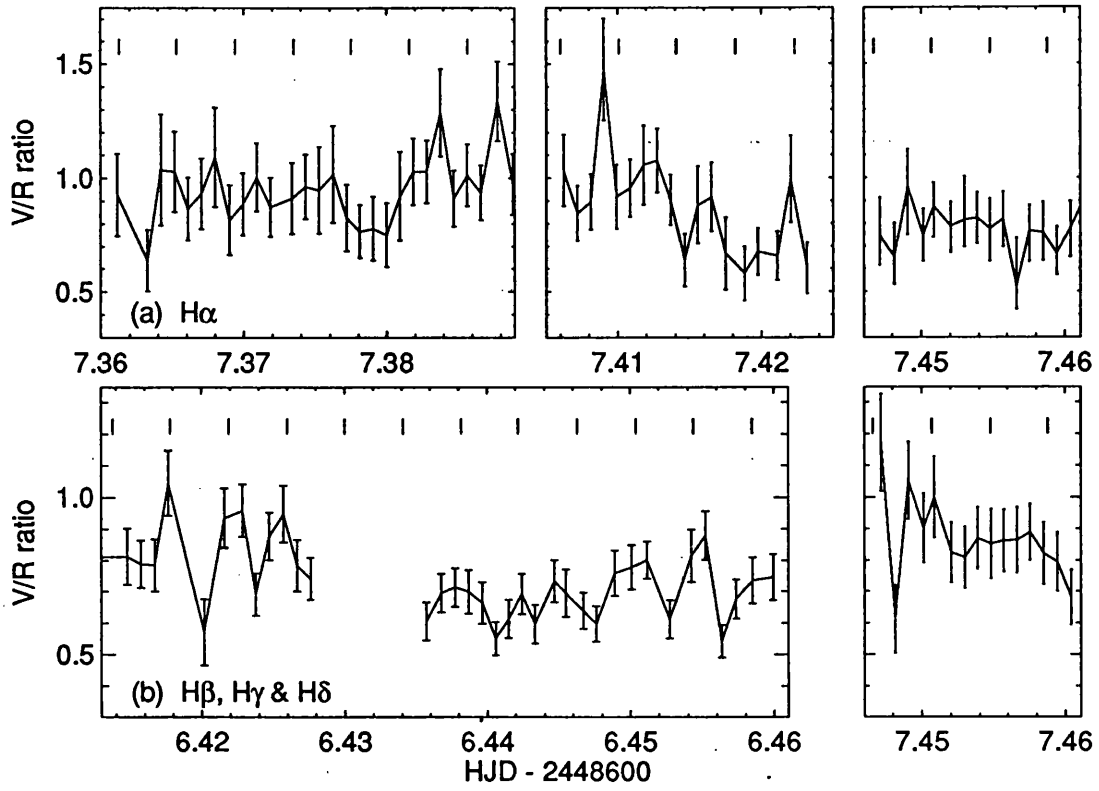

FIGURE 5.8: *V/R ratio timeseries obtained from the Balmer lines of GK Per. (a) shows the result for Hα, and (b) shows the mean result for the blue Balmer lines. The tick marks indicate minimum X-ray intensity according to the X-ray spin ephemeris of Ishida et al. (1992).*

The spin modulation in the V/R ratio can be seen in both timeseries displayed in figure 5.8. Whereas in the blue Balmer lines this modulation has its maximum near the phase of X-ray spin minimum according to the ephemeris of I92 (phase zero, as indicated by the tick marks), there is evidence that in Hα (observed half an orbital cycle later) a different phasing exists. This is illustrated more clearly in figure 5.9, showing the data folded according to the same ephemeris. The first night's data show a quasi-sinusoidal V/R ratio modulation with a maximum at spin phase zero in both the blue Balmer lines (figure 5.9[b]) and He II λ4686 (figure 5.9[a]). However, in the second night's data (figures 5.9[c] and [d]), whilst a modulation with a similar morphology is observed, the phasing has indeed shifted with respect to that of first night. Sinusoidal fits establish that the V/R ratio spin variation

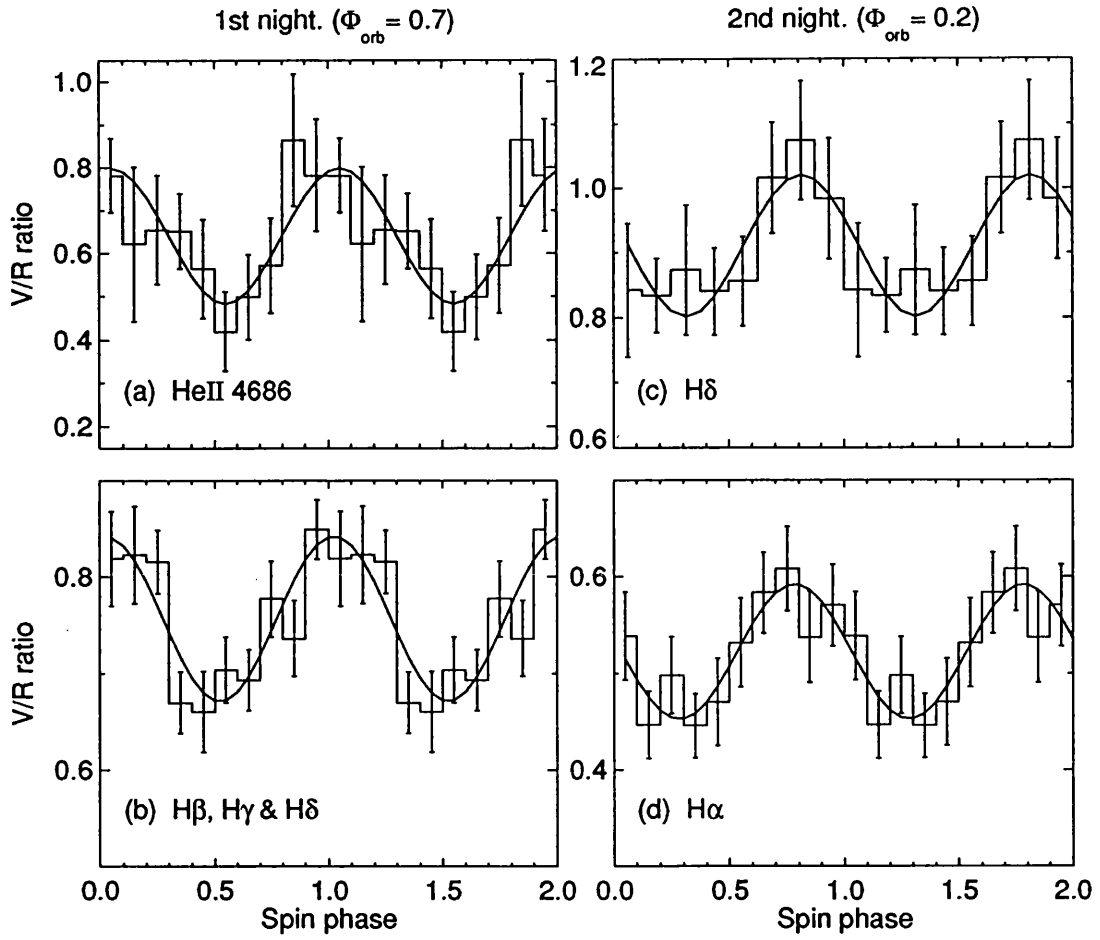

FIGURE 5.9: *The V/R ratio data folded according to the ephemeris of Ishida et al. (1992) and rebinned. The best-fitting sinusoids are also shown. Note the phase shift of the modulation on the first night (a and b) compared to that on the second night (c and d).*

on the second night is 0.24 ± 0.05 cycles out of phase with the modulation on the previous night. (Note that the same lines were not observed on both nights, so I am unable to compare 'like with like' in figure 5.9).

The fact that no such phase shift is seen in the equivalent width data (see figure 5.5) suggests that the timings are not in error and that the spin ephemeris of I92 is correct. A possible explanation for the V/R ratio phase shift is that the V/R ratio may vary on a period which is very close to, but nonetheless differs from, the equivalent width period. Although the V/R ratio in intermediate polars is not

generally observed to vary at a sideband period, the orbital sidebands of the X-ray period must be considered as possible candidates for the V/R ratio period. GK Per has such a long orbital period that the orbital sidebands of the X-ray spin-pulse are very close to the spin frequency itself. The sideband periods, calculated from the orbital and pulsation periods in CCF and I92 respectively, are 350.6270 s and 352.0580 s ($\pm$0.0001 s). Given the quality of the current data, a Fourier spectrum cannot be used to differentiate between a variation at the spin period or either of the sidebands, so a different technique is needed to test this possibility.

I have compared the phasing of the V/R ratio modulation on the first night with that on the second night as follows. I folded the blue Balmer line V/R ratio data (first night only) on a series of test frequencies in the range 245–247 d^{-1} (P = 349.80–352.65 s, covering all previously published values of the spin period), rebinned the result at each stage, fitted a least-squares sinusoid, and measured the phase parameter of the best-fitting curve. I then repeated this for the Hα V/R ratio data observed on the second night. This process yielded the sinusoid phase versus folding period for each of the two V/R ratio datasets. I obtained the relative phase of the fitted sinusoids as a function of period by subtracting one from the other. One expects a relative phase of zero (i.e., with the folded datasets in phase) when each dataset is folded on the correct period, if the pulsation in both datasets has a common ephemeris. Note that a non-zero relative phase may arise in this analysis in the event that the modulation is not sinusoidal. However, figure 5.9 shows that the V/R ratio variation is described well by a sinusoid at both orbital phases observed.

Figure 5.10(a) displays the result of this analysis. This diagram illustrates that at the known period of rotation of the white dwarf (ω), the phasing of the V/R modulation in Hα differs from that in the other Balmer lines by $\sim$0.25 cycles (cf. figure 5.9). Two periods where the relative phase is zero are apparent in figure 5.10(a) (351.0 $\pm$ 0.2 s and 352.4 $\pm$ 0.2 s, estimated from the diagram), but neither of these periods corresponds to the sideband periods which I have calculated

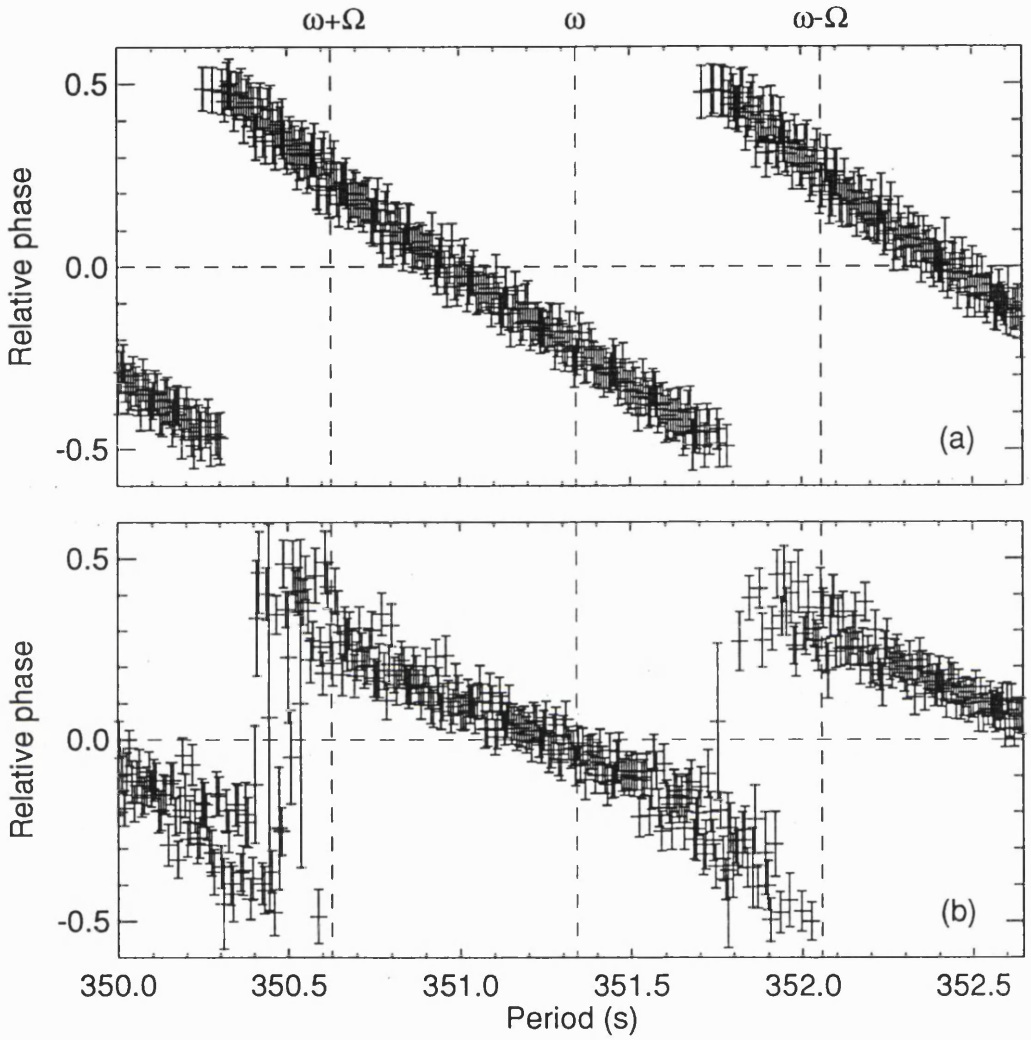

FIGURE 5.10: *The two V/R ratio datasets (from the blue Balmer lines [first night] and from Hα [second night]) were folded on a series of test periods and fitted with sinusoids at each stage. (a) shows the difference in phase between the sinusoids fitted to each dataset at each period. At the known period of rotation of the white dwarf (ω, Ishida et al. 1992), the V/R ratio spin modulation in Hα is ∼ 0.25 cycles out of phase with the V/R ratio spin variation in the blue Balmer lines, measured a day earlier. (b) shows the results of a similar analysis of the equivalent width data. In the latter case the period which gives a relative phase of zero is consistent with ω.*

above. The orbital period would have to be, but is not, in error by some 20% for the sideband periods to be compatible with those periods where the relative phase is zero. In addition, the X-ray pulse period is known accurately from several X-ray satellite observations; all measurements so far made have indicated the X-ray period to be in the narrow range 351.335–351.347 s (Watson, King & Osborne 1985; Norton, Watson & King 1988; I92). These considerations suggest, therefore, that the values of the sideband periods in figure 5.10 are accurate. Thus, as no such phase shift is apparent in the equivalent width data (see figure 5.10[b]) the indications are that the ephemeris of I92 is likely to be correct (the only other period candidates suggested by figure 5.10[b] are too far outside the measured range mentioned above to be likely), and that the V/R ratio has indeed undergone a true 'glitch' in phase between nights.

Figure 5.10(a) leads to an ambiguity as to which period is present in the V/R ratio data. As a glitch is present in the phasing of the V/R ratio modulation, there is no way of telling whether the modulation is at the X-ray period, or an orbital sideband. However, as all well-studied intermediate polars with well-determined spin periods show V/R ratio modulation at the spin period, and not at a sideband period, it is likely that the V/R ratio in GK Per also varies at the spin (X-ray) period. In accordance with Hutchings & Cote (1986), I therefore interpret the V/R ratio variation as a radial velocity spin modulation.

5.3.4 ORBITAL-CYCLE LINE VARIABILITY

Figure 5.11 shows the spin-averaged blue Balmer lines as observed at orbital phases 0.7 and 0.2. Their double-peaked profiles, possibly caused by an accretion disc, can clearly be seen. Note that in the top panels there is evidence of an emission component in each of the lines which blends into the red peaks at a velocity near $+100\,\mathrm{km\,s^{-1}}$. This component is probably also present in all three lines on the second night; however, in this latter case its central velocity is $\sim 0\,\mathrm{km\,s^{-1}}$, and the component has merged with the *blue* peaks. Owing to the low velocities and

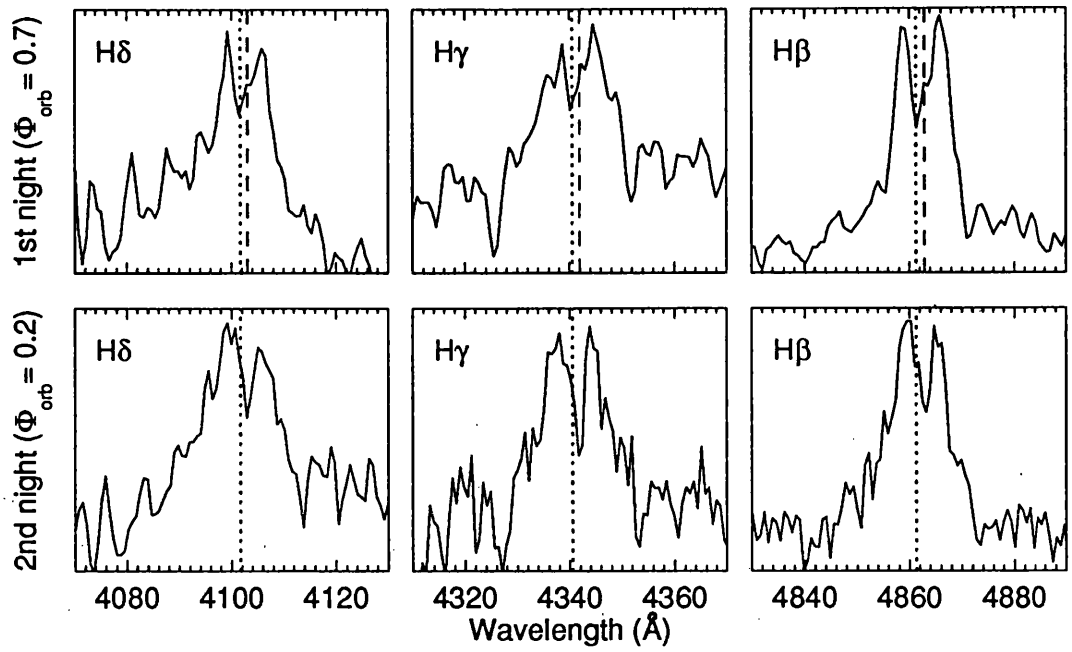

FIGURE 5.11: *The mean profiles of the blue Balmer lines as observed on the first night (top) and on the second night (bottom). Intensity units are arbitrary, and the dotted lines indicate the laboratory (rest) wavelength. Note the apparent component situated near a velocity of +100 km s^{-1} (dashed lines) in the top panels, which is partially blended with the red peaks. On the second night, the same component may also be present, but with a lower velocity (close to zero), blended with the blue peaks.*

narrow width involved, this orbitally modulated component probably emanates far from the white dwarf, and may therefore represent the 'S-wave' component which arises from the impact of the accretion stream on the edge of a disc (see §1.5.4.3 for an explanation of the S-wave).

5.3.5 SUMMARY OF RESULTS

My main findings are as follows.

(i) The spectral classification and luminosity class of the secondary is judged to be K0 V–III p.

(ii) The V/R ratio is modulated at the spin period in the wings of both He II λ4686 and the H I lines, but shows a glitch in its phasing. The equivalent

width, also modulated at this period (H I lines only), shows no such phenomenon. The phase shift makes it very difficult to realise how the V/R ratio modulation might be caused by material which is entrained, as in other systems, in a rotating magnetic field.

(iii) The Hα line is clearly single-peaked, whereas the other Balmer lines, and the He I lines—all of which were observed simultaneously with Hα—exhibit a double-peaked profile.

(iv) Finally, though the result is unconfirmed (owing to a lack of *direct* detection), the optical continuum may vary at the spin period in antiphase with the line emission and X-ray pulsation (see §5.3.3.2). This behaviour is not generally seen in intermediate polars, but Pietsch et al. (1984) showed that the spin-pulse in AO Psc underwent a 180° phase shift at some juncture. This suggests that that system, too, once had antiphased X-ray and optical pulsations.

5.4 DISCUSSION

5.4.1 THE LINE EMISSION REGIONS

5.4.1.1 The Balmer series and neutral helium lines

The double-peaked emission lines may originate in an accretion disc, but Hα, in contrast, is *single*-peaked. A single-peaked profile might arise in an accretion disc in the event of Stark broadening (Lin, Williams & Stover 1988), but this would affect *all* the Balmer lines. Indeed, in the calculations performed by these authors the Balmer lines are either all double-peaked or all single-peaked. The Hα line appears not to have been studied as extensively in intermediate polars as the blue Balmer lines have, so it is not known if the GK Per result is unique. Previous publications containing spectra from intermediate polars either do not include Hα, or are of insufficient spectral resolution to determine whether the lines are double-peaked. For example, an optical spectrum of GK Per which contains both Hα

and Hβ has been presented by Anupama & Prabhu (1993), but the reciprocal dispersion (5.5 Å pixel^{-1}) is insufficient to determine the structure of these lines. However, where sufficiently high-resolution observations of Hα have been made in other systems (e.g., in EX Hya [Hellier et al. 1989] and FO Aqr [K. Mukai, private communication]), the line clearly has a similar profile to the other Balmer lines (all lines being double-peaked in these two cases), in contrast to the GK Per observations.

A possible explanation for the single-peaked Hα profile is that its centre may be filled in by a component which is not present in the other lines. This conclusion is arrived at by considering the line ratios in GK Per as follows.

There is an inverted decrement in this system (table 5.2; cf. Anupama & Prabhu 1993), which implies that the high-order Balmer emission is not consistent with simple optically thin radiative recombination (e.g., Brocklehurst 1971). At least two possibilities exist which yield Balmer decrements that differ significantly from the Case A and Case B values.

(i) The emission region may be of low density, and immersed in a strong radiation field, so that stimulated emission is important. However, calculations by Elitzur et al. (1983) show that if this regime is operating, the Hα line ought to be weaker, relative to the other Balmer lines, than is observed here. For example, the observed strengths of Hγ and Hδ relative to Hβ (see table 5.2) imply an ionisation parameter[1] $U1 \sim 10^{2.5}$ (see figure 5.12[a]); however, at this value of $U1$, the expected ratio I(Hα)/I(Hβ) is ~ 0.7, whilst the observed value is 1.7 ± 0.3. Therefore, if this regime is operating in the line emission region, a second emission site is required to increase the intensity of Hα to the level observed.

(ii) The line emission region may have a *high* electron density, so that electron-atom collisions are non-negligible (Adams & Petrosian 1974). This has been sug-

[1]Elitzur et al. (1983) define the ionisation parameter, which parameterises the continuum flux, via $U1 = 4\pi I_0/hcN_e$, where I_0 is the external radiation intensity at the ionisation edge, N_e is the electron density, c is the speed of light in a vacuum, and h is Planck's constant.

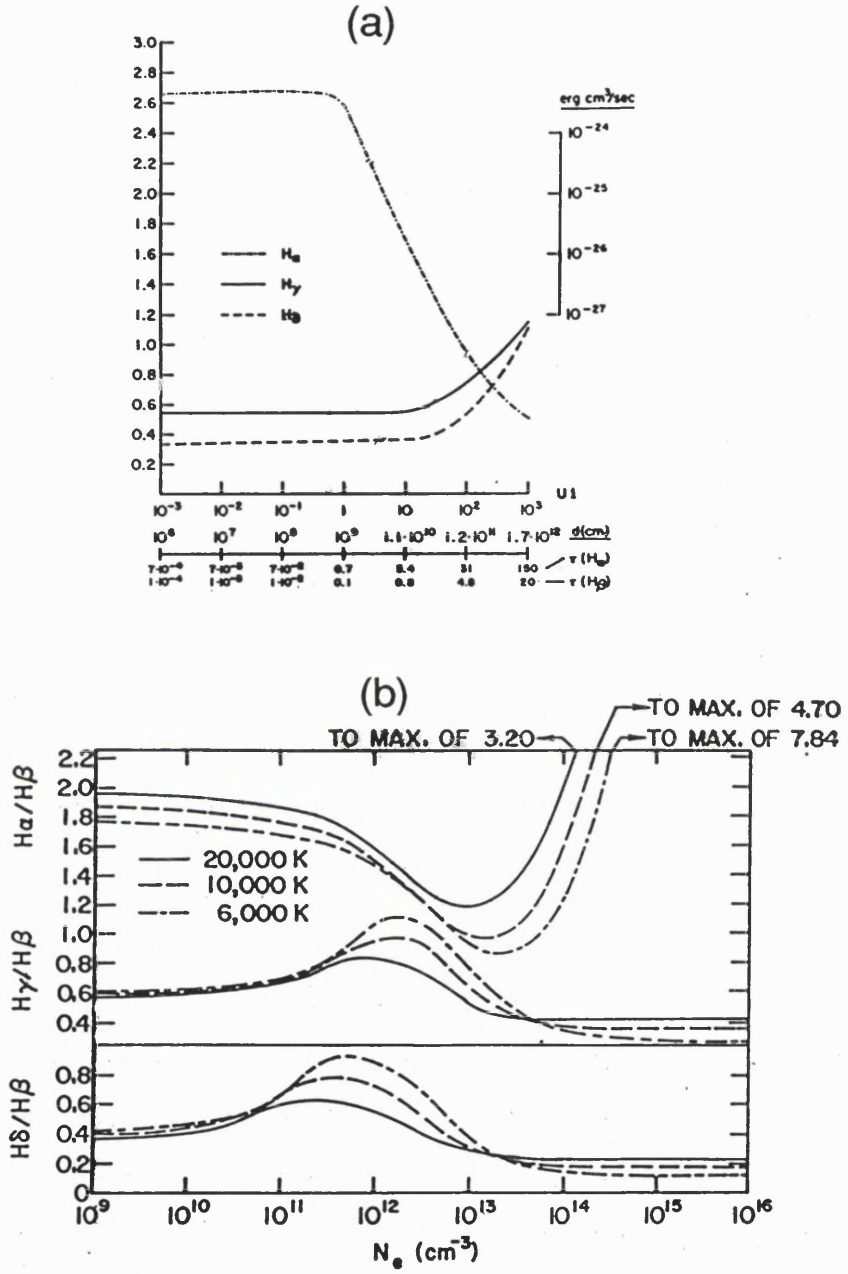

FIGURE 5.12: *(a) Intensities of the Balmer series emission lines as a function of ionisation parameter, for $T = 10^4$ K and $N_e = 10^{11}$ cm^{-3}. The optical depths of Hα and Hβ are marked on the abscissa. Adapted from Elitzur et al. (1983). (b) Graph of Case A Balmer decrement versus electron density, including the effects of inelastic electron-atom collisions, for various temperatures. From Adams & Petrosian (1974).*

gested by Anupama & Prabhu (1993) to explain the ratio $I(H\alpha)/I(H\beta) \simeq 1.9$ which they observed for GK Per. At the lowest densities, the Balmer decrement does not differ significantly from that expected by radiative recombination; however, as the density increases, collisional excitation becomes more important, and the energy level above which collisional excitation dominates decreases. Figure 5.12(b) shows the Case A calculations of Adams & Petrosian (1974). On the assumption that the high-density regime is operating, it can be seen from this graph that the line ratios in table 5.2 are consistent with those expected when the electron density in the line emission source is in the range $10^{11.5}$–$10^{12.5}$ cm^{-3}. However, the UV spectrum of GK Per, both in outburst and in quiescence, contains semi-forbidden lines (Wu et al. 1989), and the observed N IV] λ1486 line in particular has a critical density for collisional deactivation of $10^{10.5}$ cm^{-3} (Elitzur et al. 1983). This is at least an order of magnitude lower than the value allowed by the Balmer decrement in the high-density regime according to Adams & Petrosian (1974), and suggests that a lower density emission region is present, in addition to the primary source.

Thus, there exist two possible scenarios: either the electron density in the emission site is low and there is a second Balmer line emission region, or the electron density in the emission site is high and there is a second region which emits the UV lines. In either case, at least two emission regions must be present in this system. With this in mind, it may be possible to attribute the single-peaked appearance of Hα to a secondary emission component which fills in the centre of the (otherwise double-peaked) profile, as suggested above. If a Balmer component indeed emanates from a secondary emission region, such emission must exhibit a fairly steep Balmer decrement, otherwise the fill-in effect would be present in some other Balmer lines as well as in Hα. One mechanism which may therefore be operating in the secondary emission region is radiative recombination in an optically thin gas, where decrements such as $I(H\alpha)/I(H\beta) \simeq 3$ are expected (Brocklehurst 1971). As the secondary Balmer region is required to be of low density, it may also be responsible for the UV emission lines. Alternatively, these may originate in a

third region.

Owing to a lack of structure in, and orbital coverage of, Hα, the location of this secondary emission region cannot reliably be estimated from this line. Interestingly, however, the blue Balmer lines exhibit a narrow, orbitally modulated emission component (see figure 5.11). It at first seems plausible that this may also represent the optically thin fill-in component from the secondary region, but that the intensity is not as strong as in Hα and so it does not completely fill the blue Balmer lines in. However, judging from the velocity of this narrow component (near $+100\,\mathrm{km\,s^{-1}}$ at orbital phase 0.7, and $< 0\,\mathrm{km\,s^{-1}}$ at orbital phase 0.2), the only plausible location for this emission region is in the vicinity of an accretion disc bulge, caused by the impact of the accretion stream from the companion. Such a region is unlikely to have a low enough electron density to emit optically thin Balmer lines via radiative recombination, or semi-forbidden UV lines. Thus, the narrow component near the centres of the blue Balmer lines may be an S-wave component, but cannot be the required secondary emission source.

Further possibilities for the secondary source include an accretion disc corona or an accretion disc wind. In general, a disc atmosphere will become hydrostatically unstable, leading to the formation of a vertically directed wind, if there is some heating mechanism (e.g., viscosity in the disc, or X-ray heating; Czerny & King 1989a, 1989b) which does not balance the rate at which the disc cools (e.g., by Comptonisation of the disc flux; Czerny & King 1989a, 1989b). If an optically thin wind, nearly perpendicular to the disc, is present in this system, and is responsible for the UV emission lines (as well as the fill-in Balmer component), one requires a fairly high inclination because the UV emission lines in GK Per do not exhibit strong P Cygni profiles (Wu et al. 1989). It is interesting to note, therefore, that a high inclination (82–86°) has been proposed for GK Per by KWM, based on their modelling of the amplitude of the optical outbursts. As I will discuss in §5.4.2, this inclination is likely to be an overestimate, but an inclination near 70° may not be unreasonable for GK Per.

5.4.1.2 The He II λ 4686 line

The He II λ 4686 line is not double-peaked, which indicates that the *majority* of its emission arises in a region more localised than that producing the He I and H I lines. A possible location is the 'bright-spot' where the accretion stream interfaces with the disc (Williams 1980). However, as the width of this line is comparable to the widths of the H I and He I lines, and as the V/R ratio in its wings is spin-modulated, some He II must also be produced in material which is entrained in the white dwarf's magnetic field.

5.4.2 THE INCLINATION OF GK PERSEI

It has been almost a century since the discovery of GK Per as a nova (1901). Despite this timespan the inclination of the system is still unknown. The orbital period is so long that any eclipse would last for approximately 4 hr and be difficult to observe. The most recent suggestion for the inclination is 82–86°, for a white dwarf mass of 0.7–0.8 $M_\odot$ (KWM). This is likely to be an overestimate, for reasons which I now discuss.

(i) On the assumption that the double-peaked H I and He I emission lines originate at the outer edge of an accretion disc (Williams 1980), the inclination and white dwarf mass given by KWM may be used to calculate the expected line-peak velocity-separation as follows.

From Kepler's third law, the separation, d, of two stars in a binary system is related to the system parameters via

$$d = 3.5 \times 10^{10} M_1^{1/3} \left(1 + \frac{M_2}{M_1}\right)^{1/3} P_{hr}^{2/3} \text{ cm} \qquad (5.1)$$

(e.g., Frank, King & Raine 1992), where M_1 and M_2 are the masses of the white dwarf and the secondary, respectively, in Solar units, and P_{hr} is the binary period in hours. Furthermore, Paczynski (1971) has shown that the radius, R_1, of the

white dwarf Roche lobe is given by

$$\frac{R_1}{d} = 0.38 + 0.20 \log\left(\frac{M_1}{M_2}\right) \tag{5.2}$$

(for $0.3 < M_1/M_2 < 20$). The radius of the primary Roche lobe in GK Per is calculated—using equations 5.1 and 5.2, and adopting $M_1 = 0.7$–$0.8\,M_\odot$ (KWM), $P_{hr} = 47.9$, and $M_2/M_1 = q = 0.28$ (both from CCF)—as $R_1 \simeq (2.18\text{–}2.29)\times10^{11}$ cm. The formula for the Keplerian orbital velocity at distance R from the white dwarf,

$$V_K = \left(\frac{GM_1}{R}\right)^{\frac{1}{2}}, \tag{5.3}$$

then implies $V_K \simeq 207$–$216\,\mathrm{km\,s^{-1}}$, evaluated at $R = R_1$. Finally, KWM's lowest inclination of 82° therefore gives a maximum observable line-peak velocity-separation in the range 410–428 $\mathrm{km\,s^{-1}}$, assuming the disc to fill the primary Roche lobe.

The observed line-peak velocity-separations ($402 \pm 54\,\mathrm{km\,s^{-1}}$ in the Balmer lines and $409 \pm 33\,\mathrm{km\,s^{-1}}$ in He I) are in excellent agreement with the values calculated above (410–428 $\mathrm{km\,s^{-1}}$) using KWM's mass and inclination estimates and *assuming that the disc radius equals that of the primary Roche lobe.* However, it is unlikely that a disc will fill the Roche lobe to this extent because of, for example, tidal interaction of the disc edge with the secondary. A smaller disc would result in a larger velocity-separation than is observed for the same inclination. Therefore, a smaller inclination is needed to fit the observed line-peak velocity-separation.

(ii) If the inclination calculated by KWM is indeed correct, then the disc in GK Per will have been in partial eclipse on the first night I observed the system (orbital phase 0.7). Figure 5.13 shows the expected views of the system at orbital phases 0.2 and 0.7, assuming CCF's mass ratio (M_2/M_1) of 0.28, inclinations of 82° and 70°, and assuming the disc to extend to the edge of the white dwarf Roche lobe. Obviously at the higher inclination (lower diagrams) the blue-shifted portions of the disc are obscured at orbital phase 0.7, so strongly asymmetric emission line profiles are expected. This does not fit the observations because the blue Balmer lines clearly exhibit double-peaks at both orbital phases I observed. This shows

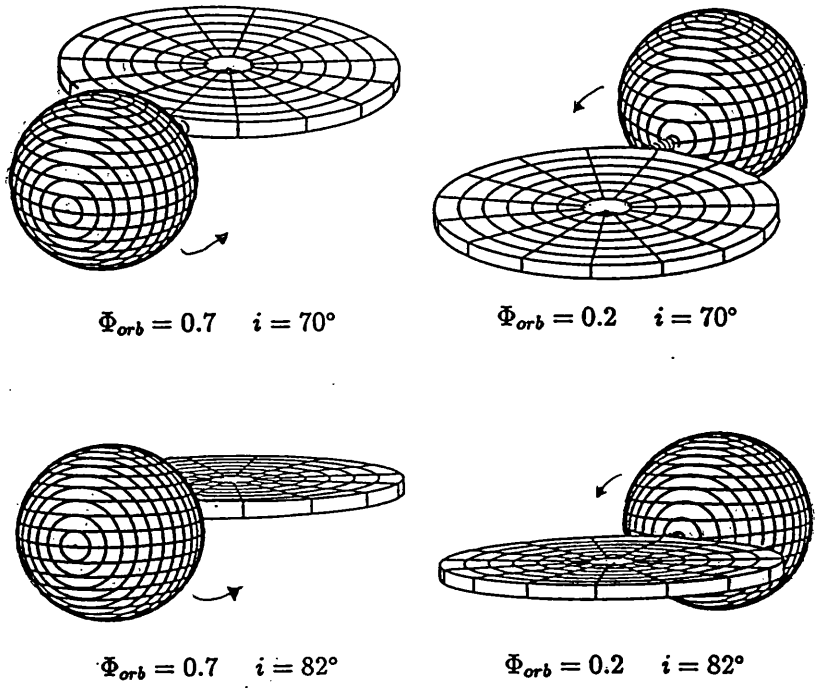

FIGURE 5.13: *Views of GK Per as expected at inclinations of 70° (top) and 82°. The pictures show the system at orbital phases 0.7 (left) and 0.2. I have assumed an inner disc radius of* 3×10^{10} *cm (from Kim, Wheeler & Mineshige 1992), white dwarf mass* $0.7 M_{\odot}$ *(also from Kim, Wheeler & Mineshige 1992), and a mass ratio of 0.28 (from Crampton, Cowley & Fisher 1986). The disc is assumed to extend to* R_1*. Diagrams courtesy of S. Rosen.*

that an eclipse of the blue edge of the disc may be discounted if the lines are produced at the edge of a disc which fills its Roche lobe. If, however, the Balmer lines are emitted closer to the *centre* of the disc, or if the disc is smaller than the primary Roche lobe radius (as it probably should be), then, as in (i), the velocity-separation of the line peaks will be larger, for a high inclination, than is observed. Hence, a lower inclination is required to avoid a substantial line eclipse.

(iii) Finally, figure 5.13 shows that for an inclination of 82°, approximately a quarter of the surface of the secondary is eclipsed by the disc at orbital phase 0.2. At

this orbital phase, I calculate that the strongest absorption lines observed from the secondary in the current data (Ca I λ4227 and Fe I λ4384) exhibit only a small ($\sim$ 9%) reduction in fractional depth compared to phase 0.7. This suggests, assuming for simplicity a uniform surface brightness in the K-star, that the inclination may be high enough for the disc to eclipse the secondary, but not by a substantial fraction.

The above considerations indicate that KWM's estimate of the inclination of GK Per is probably incorrect. An inclination of $\sim 70°$, shown in figure 5.13, seems more suitable. This inclination is still high enough to account for the observed velocity-separation of the Balmer line peaks if the disc does not extend the full radius of the primary Roche lobe.

5.4.3 THE SPIN MODULATION

It should be noted that the orbit of GK Per is so large that the presence of an accretion disc is essentially incontestable. Indeed, KWM have shown that the outbursts in this system may be modelled in terms of an accretion disc outburst model. It seems plausible, therefore, that accretion in this system occurs over a large range of azimuth onto both magnetic poles of the white dwarf, via the curtain-type flows of RMC (see §1.5.4.1). The simplest version of such a model predicts that the X-ray and V/R ratio spin modulations will occur in phase. However, the V/R ratio data of GK Per exhibit a phase shift overnight: on the first night, maximum V/R ratio occurs at *minimum* X-ray flux, and on the second night the V/R ratio has its maximum 0.25 cycles before this. It is difficult to refute this result on the basis of an incorrect spin period or an error in the analysis, because the equivalent widths and line intensities show no such phase shift.

This phase shift means that there is a serious difficulty in producing the V/R ratio spin modulation by radiating material entrained in the primary's magnetic field as required by the model of RMC. No such phenomenon has to date been witnessed in other intermediate polars. Interestingly, however, fluctuations in phase

and amplitude are also exhibited by the X-ray spin-pulse in this system in quiescence (Norton, Watson & King 1988). The phase shifts may indicate that the accretion in GK Per is unstable. This is particularly interesting in the light of the result of KWM that the inner disc radius in this system exceeds the corotation radius (r_c, where the Keplerian speed in the disc equals the rotation speed of the star) by a factor of four. This situation would indeed promote unstable accretion, but it is not understood in this event why the equivalent width and line intensity modulation appears, in contrast, to be stable in phase.

A possible explanation for the observed line spin modulation is that two components may contribute to the spin variation in GK Per, one from a curtain-type flow, and one from material circulating at the corotation radius, r_c. As it is unlikely that any corotating blobs producing a radial velocity modulation will survive indefinitely, their eventual disappearance when the material is finally accreted or dispersed means that the V/R ratio modulation will be seen only from the curtain at these times. This will produce a phase shift in the V/R ratio. Furthermore, circulating blobs which are optically thin in the lines, or are roughly spherical and optically thick in the lines, will not contribute to the line intensity modulation. The latter will therefore be stable in phase as is observed, as it will result entirely from the curtain.

In chapter 2, I suggested that the X-ray quasi-periodicity observed in GK Per primarily in outburst might be caused by photoelectric absorption of the white dwarf flux by material orbiting near the centre of the disc. The timescale for this obscuration is such that the radius at which this material is expected to exist is 3–$5r_c$—consistent with the inner disc radius calculated by KWM assuming Keplerian rotation (see chapter 2). If this interpretation of the X-ray quasi-periodicity is correct, it is evidence that clumps of material are orbiting the white dwarf at a distance on the order of $4r_c$. However, if the inner disc radius in GK Per is, as KWM deduce, larger than r_c, then the presence of additional material orbiting at r_c, necessary to account for the V/R ratio behavior, is unexplained. It might

be possible for the rapidly rotating magnetosphere to induce corotation in at least some of the material near the inner edge of the disc, but unstable flow onto an accreting compact object has not been investigated and the mechanics are unclear. As a first estimate, it seems likely that the majority of the material will be tangentially expelled, but Ghosh & Lamb's (1978, 1979a, 1979b) accretion torque theory (summarised in §3.4.2.1) does not account for effects such as a non-dipole field, or a field which is tilted relative to the spin axis, or which is offset from the centre of the star. Perhaps under more physically realistic situations such as these, accretion onto the white dwarf may not encounter such an extreme centrifugal expulsion and may occur in a stable manner. Alternatively, an *un*stable flow may itself account, in some way, for the presence of the material at r_c. This is a problem for future investigation, and is beyond the scope of this thesis.

5.5 SUMMARY OF CONCLUSIONS

I have presented spin cycle-resolved optical spectroscopy of the intermediate polar GK Per. The results further add to this system's repertoire of atypical characteristics. I summarise my conclusions as follows:

(i) The secondary in GK Per exhibits a variable spectral type and luminosity class. These observations indicate K0 V–III p, consistent with previously published results. A narrow Ca II H emission line may originate in the atmosphere of the secondary.

(ii) The H I and He I emission lines exhibit double-peaks separated in velocity by $\sim 400\,\mathrm{km\,s^{-1}}$. With a very high inclination (82–86°, KWM), this value is consistent with line formation in the outer regions of an accretion disc which fills the primary Roche lobe. However, the change in fractional depth of the K-star's absorption lines between the two nights, and the fact that no substantial line eclipse is observed, point to a lower inclination, closer to $\sim 70°$. The FWZI of the lines ($1800\,\mathrm{km\,s^{-1}}$) indicates the presence of additional emission in more central regions

of the disc, and/or in material entrained in the primary magnetic field. The latter is confirmed by the fact that the equivalent widths, intensities, and V/R ratio of the line emission is modulated at the X-ray spin period. Semi-forbidden UV lines support the presence of a low-density emission region, such as an accretion disc corona/wind. As the Hα line is not double-peaked, its centre is probably filled in by an optically thin emission component which may also originate in an accretion disc corona/wind.

(iii) The He II λ4686 line, in contrast to the He I lines and the majority of the H I lines, is single-peaked. Much of the He II λ4686 line flux may arise in an accretion disc bright-spot. However, this line is also spin-modulated (in radial velocity only), implying the presence of weaker He II emission entrained in the primary magnetic field.

(iv) The most fascinating result to come out of the GK Per analysis is the glitch in the phasing of the V/R ratio spin modulation—no such behaviour is observed in the equivalent widths or line intensities. Line emission evidently is modulated at the white dwarf rotation period, but the V/R ratio variation is not consistent with an accretion curtain, even though the system probably contains a disc. The glitch might be attributed to the occasional appearance/disappearance of blobs orbiting in unstable orbits near the white dwarf corotation radius. These blobs might be associated with additional material, orbiting farther out, that produce the X-ray quasi-periodicity (see chapter 2). Clearly, however, further high-quality spin-resolved spectroscopy are needed to verify the existence of the phase shift before this picture, or other scenarios, can be considered. Until then, the result must probably be regarded with caution, although it should be remembered that the X-ray spin-pulse in GK Per has also shown instabilities in phase as well as in amplitude (Norton, Watson & King 1988).

ADDENDUM 5

1. On page 157, after 'Figure 5.9' on line 3, continue the parenthesis with: 'Note, however, that Hδ was fully covered on both nights, as it was present in both wavelength ranges of the blue spectra', then close the parenthesis.

APPENDIX: REDUCTION AND ANALYSIS

Everything has been discussed and analysed, or at least mentioned.

Jean d'Alembert
Elements of Philosophy (1759)

A.1 INTRODUCTION

A large body of this thesis deals with the analysis of CCD data, both photometric and spectroscopic. To avoid the repeated explanation of the reduction and analyses of such data in the previous chapters, this appendix contains a brief overview of the techniques used throughout for the reduction of the CCD images and the subsequent analysis. I also discuss the reduction of the *EXOSAT* timeline data, which are presented in chapter 2.

A.2 GENERAL CCD REDUCTION TECHNIQUES

A CCD image has to be 'cleaned' before the data contained within it are processed. Briefly, the reduction of CCD data comprises several steps: debiasing the frame, dark current compensation, the flatfield correction, and removing cosmic ray events.

The bias level is an electronic offset which is added to the CCD frame. Its purpose is to ensure that negative electron counts do not arise in the analogue-to-digital conversion process. The method I used for the data presented in this thesis

was to extrapolate the bias level determined from the overscan region at the edge of the chip, where the charge signal has already been measured, and subsequently to subtract this from the required image.

CCD detectors are not faultless. Small-scale pixel-to-pixel variations in the detector efficiency do occur, as well as large-scale fluctuations generated by the variation in thickness of the silicon substrate. In addition, foreign objects such as dust may accumulate on the chip, reducing the sensitivity in these locations. The purpose of the flatfield correction is to remove these effects from the image. To acquire a flatfield frame for the photometry, the CCD detector was exposed to a uniformly illuminated source. The morning and evening twilight skies were used for this purpose, whilst ensuring that the sky was sufficiently bright, and the integration period sufficiently short, that unwanted point sources such as faint stars were not recorded. For the spectroscopy, I obtained the flatfield by illuminating the chip with a tungsten lamp, which avoids the introduction of sky lines in the flatfield.

The flatfield correction procedure is not the same in the case of the photometry as for the spectroscopy. For the former, the CCD image to be corrected is divided by the normalised flatfield frame. In the spectroscopic case, however, a tungsten flat was used which has a different continuum to that of the sky. In this situation it is not permissible to simply divide the CCD images by the normalised flatfield. The procedure actually used involves several steps. First, the tungsten flatfield information is 'squashed' in the x-direction, effectively reducing the data to a one dimensional stream along the y-axis, to which a polynomial—usually of order four or less—was fitted to describe the mean variation. This process is then repeated for the y-direction. Finally, with the mean chip variation described by orthogonal polynomials, the flatfield correction is applied by dividing the debiased target frames by the polynomial 'surface'.

Dark currents, caused by thermally generated electrons, were negligible in all observations, owing to the short integration times used ($\sim 60\,\mathrm{s}$).

As well as the above effects, cosmic ray events had to be removed when they were inconveniently situated. For the photometry, cosmic rays were not so troublesome because the probability of a cosmic ray impact directly on top of a stellar image is relatively small. For the spectroscopy, however, cosmic rays proved a much more common occurrence. The procedure employed for the removal of cosmic rays was not the same for the photometry as for the spectroscopy. The processes used are outlined in the following two sections, which describe some of the specific analysis techniques used in chapters 3–5. Further procedures, used only in single chapters, are described in the individual chapters in which they occur.

A.3 PHOTOMETRY

The photometry (on BG CMi) reported in this dissertation were obtained with the Jacobus Kapteyn Telescope at La Palma. A CCD-GEC3 camera was situated at the f/15 Cassegrain focus and a coated GEC-P8603 CCD detector was employed. Johnson filters B, V, and R were used. Integration times, etc., are discussed at the beginning of chapter 3.

A typical frame consists of the target object and at least two comparison stars. The latter are sources relative to which the flux level of the target star may be determined and as such they must not contain any intrinsic variability of their own. I tested for intrinsic variability by taking the ratio of the counts in the comparison stars to calculate the magnitude difference as a function of time. An investigation by eye yielded no significant trends in the result, and this was confirmed by a Fourier analysis. As the comparison stars are on the same frame as the target object, the integration times and atmospheric conditions are identical in each case, and the magnitude of the target object can be determined if the magnitudes of the comparison stars are known. Thus, standard stars of known magnitude were also observed which, under photometric conditions, could be used to calculate the magnitude of the comparison stars (see §A.3.2). However, the count-rates measured for the standards and comparisons first had to be corrected for the effects

of atmospheric extinction (see §A.3.3).

A.3.1 OBTAINING THE COUNT-RATES

The entire process of cosmic ray identification and count-rate measurement is automatic. A source-searching algorithm (J. Mittaz, private communication) first locates the stellar images in a given frame by comparing single pixel counts with the local mean count level. If the count in a particular pixel is greater than twice the value in an adjacent pixel, a cosmic ray hit is assumed, and the pixel count is replaced with the local mean value. Once identified, a source is enclosed in an ellipse and the counts within summed. Then the background count is obtained by fitting an annulus around the source ellipse, and this is subtracted from the source-plus-background value.

A.3.2 ATMOSPHERIC EXTINCTION

The effect of atmospheric extinction is to modify the intrinsic (i.e., above the atmosphere) apparent magnitude m of an object by an amount

$$k_\nu \sec(z) = m_{obs} - m, \tag{A.1}$$

where m_{obs} is the observed apparent magnitude, z is the zenith distance at the mid-time of the integration (sec[z] is an approximation to the airmass) and k_ν is the atmospheric extinction coefficient for the frequency band ν. It is possible to calculate a mean value for k_ν from observations of a non-varying source, such as a comparison star. If the count-rate associated with the observed magnitude is C_{obs}, then the count-rate, C, one would expect in the absence of atmosphere will be given by the formula which defines the magnitude scale,

$$m_{obs} - m = 2.5 \log\left(\frac{C}{C_{obs}}\right). \tag{A.2}$$

Combining equations A.1 and A.2 and re-arranging, one arrives at

$$\log(C_{obs}) = \log(C) - 0.4\, k_\nu \sec(z). \tag{A.3}$$

Thus, for a sequence of observations of a constant source (a comparison star), a least-squares linear fit to a graph of $\log(C_{obs})$ against $-0.4\sec(z)$ may be used to calculate the average extinction coefficient throughout the observation from the gradient. It should be realised that although changes in extinction as a function of time are ignored in this calculation, observations made by the Cambridge Automatic Meridian Circle (CAMC) indicate that this variation was less than $0.005\,\mathrm{mag\,airmass^{-1}\,hr^{-1}}$ in the V band during the beginning of January 1992. For the relatively short length of the current observations (1–3 hr) this amounts to less than a 5% variation in extinction throughout each run.

If the range of airmass through which the observations are made is small, then extinctions calculated using the above method are unreliable, as the length of the abscissa may be too short to determine an accurate gradient. However, if it is assumed that the extinction is grey, so that any changes in k_V do not alter the coefficients in colours such as $B - V$ and $V - R$, then $k_B - k_V$ and $k_V - k_R$ will be constant. I have calculated the average values for the latter quantities from coefficients supplied by D. Jones (private communication), which are annual averages at La Palma. The mean colours are:

$$k_B - k_V = 0.11 \tag{A.4}$$

$$k_V - k_R = 0.07. \tag{A.5}$$

A.3.3 Magnitudes

To calculate the magnitude of the target object on each frame, I first determined the magnitudes of the comparison stars as follows. Under the assumption that a comparison star and a standard star are observed in similar atmospheric conditions and at the same airmass, the intrinsic (i.e., above the atmosphere) apparent magnitude, m_c, of the comparison star would usually be calculated from, again by definition of the magnitude scale,

$$m_c = 2.5\log\left(\frac{C_s}{C_c}\right) + m_s, \tag{A.6}$$

where C_c is the count-rate measured for the comparison star and C_s is the count-rate measured for the standard star whose apparent magnitude above the atmosphere, m_s, is already known. I addressed the requirement that the atmospheric conditions be similar for both stars by using only standard stars that were observed on the same night as the target observations. However, the condition that the comparison star and standard star be observed at the same airmass was not satisfied in most cases, so this equation could not be applied directly.

In these instances, I adjusted for the effects of extinction by correcting all observed count-rates to the values expected above the atmosphere, which are obtained from equation A.3 after some manipulation:

$$C = C_{obs}\, 10^{0.4\, k_\nu \sec(z)}. \tag{A.7}$$

Then, having corrected the count-rates observed for the comparison and standard stars to the values expected in the absence of extinction, I used equation A.6 to calculate the magnitude of the comparison stars (above the atmosphere) on each target frame. Having obtained the magnitudes of the comparison stars, equation A.6 could then be used also to calculate the magnitude of the target stars.

It is also possible to calculate the magnitude of the target stars simply by correcting *their* count-rates using equation A.7 and comparing them with the corrected standard star count-rates. However, this method yields only one estimate of the magnitude of each target star on a frame, whereas using the former method one obtains one estimate of the magnitude for each comparison star observed, which are then averaged to give the final result.

A.3.4 SUMMARY

To summarise, the steps which I used in magnitude calibration are:

1. Calculate the extinction coefficients (equations A.4 and A.5).

2. Exposure-correct and airmass-correct the standard star and comparison star count-rates (A.7).

3. Calculate the magnitudes of the comparison stars (A.6).

4. Calculate the instrumental magnitude of the target object (A.6).

A.4 SPECTROSCOPY

The spectroscopic data contained in this thesis were obtained on the William Herschel Telescope at La Palma using the Intermediate-dispersion Spectroscopic Imaging System. In brief, the system comprises two arms, enabling CCD images from two different spectral regions to be obtained, usually one 'red' and one 'blue'. Integration times and diffraction gratings used were not the same for BG CMi as for GK Per, so this information is discussed in the Observations sections of chapters 4 (§4.2, BG CMi) and 5 (§5.2, GK Per).

A.4.1 EXTRACTING THE DATA

The image of the stellar spectrum on the CCDs is a thin line, around 5–10 pixels wide, running the length of the chip. The chips were 'windowed', such that a region 58 by 1279 pixels was used, to minimise readout time. The sky spectrum is located either side of the stellar spectrum. Two possible methods of extracting the spectrum from the image are available.

In the simple method, adequate for bright sources, a cross-section of the spectrum along the spatial direction is obtained, which shows its profile. This enables one to locate easily which channels are 'sky' and which are 'stellar'. The spectrum is then extracted by summing the counts in the stellar spectrum channels and subtracting those measured in the sky portions on either side.

For the data here, however, an 'optimal' extraction method was adopted (Horne 1986), which maximises the signal-to-noise (S/N) of the extracted spectrum. This method assigns a higher weighting to the stellar counts at the centre of the spectrum than those counts measured in the wings of the stellar cross-section profile, where the sky becomes more and more important. In addition, the procedure involves

fitting polynomials in the spatial direction (a quadratic polynomial was used) to approximate the sky spectrum, and takes account of changes in the stellar spectrum profile along the CCD, also by fitting polynomials. As the spectrum profile is monitored along the entire CCD chip, contaminating cosmic rays events—characterised by changes in both profile structure and in count levels—are located easily. If a point is above the polynomial fit by an amount in excess of a pre-specified limit (usually a few sigma), the point is assumed to be a cosmic ray and is ignored.

A.4.2 WAVELENGTH CALIBRATION

Arc spectra (copper-argon) were taken regularly throughout the observations of BG CMi and GK Per, immediately before and after the telescope was moved; for example, when making an exposure of a flux standard. The arc lines were identified using wavelength tables, then the wavelength calibration for the first arc spectrum was obtained by fitting a low order (<4) polynomial to the wavelength/pixel number relationship. In the absence of movements in the optical system, for target spectra taken between arcs one would assign the nearest arc (in terms of time) as the appropriate calibration spectrum. However, small movements (less than one Ångstrom) in the telescope set-up (e.g., telescope flexure, the chip, the grating) are inevitable. Thus, for the target spectra the actual position of the corresponding arc calibration spectra was obtained by calculating the shift between the two nearest adjacent arcs and then interpolating the arc position at the target observation time assuming the wavelength shift to be linear with time.

To check the wavelength calibration, I compared the wavelengths of the arc lines in the self-calibrated arc spectra with their laboratory wavelengths. Also, where prominent sky spectral features were evident (in the red spectra only), their calculated wavelengths were monitored in a similar fashion. The variation was found to be less than 0.1Å throughout all observing runs. As any shifts in the set-up are likely to be mechanical and sudden rather than smooth and linear, the above arc interpolation method may yield velocity change errors in the calibrated

spectra. However, as the wavelengths of the arc lines were within ±0.1Å of their laboratory wavelengths, velocity errors were clearly not evident.

A.4.3 Flux calibration

Atmospheric conditions remained unsavoury throughout the spectroscopic observations. Thus, I applied the flux calibration purely to remove the effects of the instrumental response. Three flux standards were observed on numerous occasions each night: Hilter 600, HD19445, and HD84937. Each standard star observation was rebinned, typically into 50Å bins, and then a spline was fitted to the result to obtain the instrumental response function (IRF). Flux calibration requires a largely heuristic approach. In general, portions of the rebinned standard star spectra have to be ignored in the spline-fitting to prevent the spline from behaving in a very peculiar manner indeed! Another approach that I investigated was fitting multiple polynomials rather than a spline, but this invariably gave very unsatisfactory results.

The actual calibration itself is applied by dividing the target spectra by the IRF, but before doing this I investigated the correctness of the IRF by calibrating the flux standards themselves and comparing, by eye, the results with calibrated spectra which were known to be correct. The IRFs were found to be satisfactory in all cases.

A.4.4 Removal of atmospheric absorption features

The red spectra suffer strong atmospheric absorption features, the most prominent of which are due to the presence of water vapour in the Earth's atmosphere, producing the Telluric absorption bands centred on wavelengths 6900Å and 7600Å. To remove these features from the spectrum the usual procedure is to observe a star which is known to have a featureless red spectrum, such as an F8 star (the only intrinsic feature in such an object being Hα absorption). First the atmospheric standard spectrum is reduced to the stage of flux calibration following the steps

already outlined. Then a spline is fit to the F8 continuum, which the F8 star is then divided by, yielding a spectrum which essentially has a value of unity everywhere except where the absorption occurs—these features are of course now inverted. By setting all the non-absorbed regions to *exactly* unity, a correction spectrum is created which, when multiplied with the object spectrum, can then be used to remove the atmospheric absorption features.

Obviously, the degree of atmospheric absorption in a given spectrum depends on the airmass of the observation. Thus, the atmospheric standard has to be measured at an airmass similar to that of the target spectrum, and under similar observing conditions, if the absorption features are to be removed successfully. This means obtaining atmospheric standard spectra as often as possible throughout the observing run. However, as the object of the GK Per and BG CMi spectroscopy was to get as high a time resolution as possible, no atmospheric standards were observed because a substantial amount of target observation time would have been lost in this process (and the blue spectra, which contain no troublesome absorption features, took priority anyway). Thus, for the spectroscopy discussed in this thesis no correction for the atmospheric absorption in the red region was attempted.

A.4.5 CALCULATING EQUIVALENT WIDTHS

To measure the equivalent width, I first approximated the continuum under the line of interest by fitting a polynomial of order unity to regions either side of the line which were not contaminated by other emission (or absorption) features. Polynomials of order greater than unity were found not to be suitable for this because of the large continuum noise and the narrow range of continuum often suitable for fitting on either side of the line of interest. The area contained in the continuum below the line was then calculated, and this value then subtracted from the total area of line and continuum. Finally, the equivalent width was obtained by dividing the resultant area by the continuum level estimated, from the polynomial fit, at the line centre (defined as the laboratory rest wavelength). I repeated this

procedure for each line of interest in each spectrum, yielding equivalent width temporal information, which could then be investigated for evidence of periodicity.

A change in equivalent width might arise due to variations in either the line area or the continuum level or both. Intermediate polars often show periodic changes in photometric optical intensity, either at the spin, beat, or orbital periods, and such modulation is expected also to be present in the spectral continuum. Thus, in situations where periodic changes in continuum flux are slight and overlooked easily (e.g., perhaps because of the presence of flickering), but where a line intensity modulation is present, the equivalent width provides a useful and independent diagnostic in searching for line intensity variability, and for probing the geometric locations of such emissions.

A.4.6 Calculating V/R ratios

The V/R ratio is a measure of the asymmetry of a spectral line. The simplest measurement is obtained by dividing the spectral line about its centre (defined as the laboratory rest wavelength), subtracting the continuum, and calculating the ratio of the area of the blue portion of the line (above the continuum) to that of the red. However, if there is movement in the line wings but the line core is strong and unmodulated, it is possible that changes in the V/R ratio will go undetected with this method. Similarly, if the line *wings* are unmodulated but the line core moves (usually on the binary period) the stationary wings may dilute any V/R ratio variation observed, though to a lesser extent. Therefore, in searching for periodic changes in V/R ratio in BG CMi and GK Per, I excluded various fractions of the line to remove such contaminations. For example, material accreting along magnetic field lines, close to the rotating primary, will have a large radial velocity and this might be manifest as a spin modulation in the line wings. Thus, in searching for a V/R modulation at the rotation period I excluded the line core contribution contained in a narrow ($\sim 200\,\mathrm{km\,s^{-1}}$) section symmetrical about the line centre and measured the V/R ratio for the rest of the line, assuming the line

to terminate where it blended visually into the continuum. I approximated the continuum under the line of interest by fitting a polynomial of order unity to line-free regions on either side of the line, as in the equivalent width measurement. This procedure was repeated for each spectrum, yielding a V/R ratio timeline which could be searched for evidence of periodicity. In each case I incremented the width of the removed section in steps of $50\,\mathrm{km\,s^{-1}}$ and repeated the process to optimise any observed periodicity.

A.5 Reduction of X-ray temporal data

This section describes the reduction techniques used prior to the analysis of the *EXOSAT* data examined in chapter 2. A review of the satellite, its instruments, and the mission are given White & Peacock (1988).

A.5.1 Medium energy

The medium-energy (ME) temporal data obtained for chapter 2 has a time resolution of 10 s, and covers the energy range 1.4–8.5 keV. The ME experiment onboard *EXOSAT* consisted of an array of eight proportional counter detectors, arranged into two sets of four. During operations, one half of the array was aligned on-source, whilst the other half was offset, typically by $\sim 100'$, to monitor the background flux. The detectors would then be interchanged (usually), so that both background *and* source were monitored by each detector half. The background correction was therefore enabled by subtracting the mean count-rate measured in the offset configuration of a particular array from the counts measured when the same array was in the source-aligned configuration. The background count measured in one half of the array could also be subtracted from the source count measured simultaneously in the other array. However, this latter procedure was only adopted when no array swap was performed, because the detectors in each half had slightly different efficiencies. In the event that both detectors were aligned simultaneously (i.e., the background was not monitored), the background counts were estimated from those

times when the satellite was slewing between targets.

The ME detectors were sensitive to enhancements in Solar activity. However, for the ME data obtained in chapter 2 this problem was not encountered.

A.5.2 Low energy

The low-energy imaging telescopes (LE1 in particular) provided timeseries data in the energy range 0.05–2.0 keV, at the same time resolution (10 s) as the ME timeseries. I obtained the source-plus-background count-rate in a given image by fitting a circle around the object of interest, summing the counts contained therein, and dividing by the integration time (similar to the process of obtaining count-rates from CCD images; see §A.3.1). Two procedures were used for the removal of the background flux. The most common method involved fitting an annulus around the source circle, summing the counts contained between the two circles, and dividing by the exposure time to yield a mean count-rate which was then subtracted from the source-plus-count value. Again, this is similar to the method employed in reducing the CCD data. However, on occasions this process could not be performed due to the presence of 'hot-spots' on the image in the vicinity of the source of interest. Under these circumstances I measured the background count from three or four rectangles placed as close to the source as possible in a symmetrical pattern.

APPENDIX ADDENDUM

1. I wish to stress that I was personally involved in acquiring the spectroscopic and photometric data presented in chapters 3–5, and wrote the proposal for the spectroscopic time which we were successfully awarded on the WHT. The duties involved in acquiring the data included operating the telescope and instrument controls on the JKT, and the instrument controls on the WHT.

REFERENCES

I adopt the notation used in Monthly Notices of the Royal Astronomical Society.

Adams W. M., Petrosian V., 1974, ApJ, 192, 199

Anupama G. C., Prabhu T. P., 1993, MNRAS, 263, 335

Ashoka B. N., Seetha S., Marar T. M. K., Padmini V. N., Kasturirangan K., Rao U. R., Bhattacharyya J. C., Bhatt B. C., Paliwal D. C., Pandey A. K., 1990, in Mauche C. W., ed., Accretion-Powered Compact Binaries. Cambridge Univ. Press, Cambridge, p. 243

Augusteijn T., van Paradijs J., Schwarz H. E., 1991, A&A, 247, 54 (APS)

Barrett P., O'Donoghue D., Warner B., 1988, MNRAS, 233, 759

Bath G. T., Evans W. D., Pringle J. E., 1974, MNRAS, 166, 113

Becker R. H., Marshall F. E., 1981, ApJ, 244, L93

Berg R. A., Duthie J. G., 1977, ApJ, 211, 859

Beuermann K., Osborne J. P., 1988, A&AS, 189, 128

Bianchini A., Hamzaoglu E., Sabbadin F., 1981, A&A, 99, 232

Bianchini A., Sabbadin F., Dalmeri I., 1986, A&A, 160, 367

Brocklehurst M., 1971, MNRAS, 153, 471

Buckley D. A. H., Sullivan D. J., 1992, in Vogt N., ed., Proc. Viña del Mar Workshop on Cataclysmic Variable Stars. Astron. Soc. Pacif., San Francisco, p. 387

Buckley D., Tuohy I. R., 1989, ApJ, 344, 376

Buckley D., Tuohy I. R., 1990, ApJ, 349, 296

Cannale J. B. G., Opher R., 1991, A&AS, 251, 474

Chanmugam G., Frank J., King A. R., Lasota J.-P., 1990, ApJ, 350, L13

Charles P., Thorstensen J., Bowyer S., Middleditch J., 1979, ApJ, 231, L131

Chiappetti L., Belloni T., Bonnet-Bidaud J.-M., Del Gratta C., De Martino D., Maraschi L., Mouchet M., Mukai K., Osborne J. P., Corbet R. H. D., Tanzi E. G., Treves A., 1989a, ApJ, 342, 493

Chiappetti L., Maraschi L., Sambruna R. M., Treves A., 1989b, in Hunt J., Battrick B., eds, Proc. 23rd ESLAB Symp. on Two Topics in X-ray Astronomy. ESA Publications Division, Noordwijk, p. 349

Cooke B. A., Ricketts M. J., Maccacaro T., Pye J. P., Elvis M., Watson M. G., Griffiths R. E., Pounds K. A., McHardy I., Maccagni D., Seward F. D., Page C. G., Turner M. J. L., 1978, MNRAS, 182, 489

Córdova F. A., 1993, in Lewin W. H. G., van Paradijs J., van den Heuvel E. P. J., eds, X-ray Binaries. Cambridge Univ. Press, Cambridge, preprint

Córdova F. A., Mason K. O., Kahn S. M., 1985, MNRAS, 212, 447

Córdova F. A., Mason K. O., Nelson J. E., 1981, ApJ, 245, 609

Cowley A. P., Crampton D., 1977, ApJ, 212, L121

Crampton D., Cowley A. P., Fisher W. A., 1986, ApJ, 300, 788 (CCF)

Crawford J. A., Kraft R. P., 1956, ApJ, 123, 44

Cropper M., 1990, Space Sci. Rev., 54, 195

Czerny M., King A. R., 1989a, ApJ, 236, 854

Czerny M., King A. R., 1989b, ApJ, 241, 839

Davey S., Smith R. C., 1992, MNRAS, 257, 476

De Jager O. C., 1991, ApJ, 378, 286

Elitzur M., Ferland G. J., Mathews W. G., Shields G. A., 1983, ApJ, 272, L55

Elsner R. F., Lamb F. K., 1977, ApJ, 215, 897

Eracleous M., Patterson J., Halpern J., 1991, ApJ, 370, 330

Ferrario L., Wickramasinghe D. T., King A. R., 1993, MNRAS, 260, 149

Frank D., King A., Raine D., 1992, Accretion Power in Astrophysics. Cambridge

Univ. Press, Cambridge

Gallagher J. S., Oinas V., 1974, PASP, 86, 952

Ghosh P., Lamb F. K., 1978, ApJ, 223, L83 (GL)

Ghosh P., Lamb F. K., 1979a, ApJ, 232, 259 (GL)

Ghosh P., Lamb F. K., 1979b, ApJ, 234, 296 (GL)

Ghosh P., Lamb F. K., Pethick C. J., 1977, ApJ, 217, 578

Griffiths R. E., Lamb D. Q., Ward M. J., Wilson A. S., Charles P. A., Thorstensen J., McHardy I. M., Lawrence A., 1980, MNRAS, 193, 25P

Hameury J.-M., King A. R., Lasota J.-P., 1986, MNRAS, 218, 695

Hameury J.-M., King A. R., Lasota J.-P., Ritter H., 1988, MNRAS, 231, 535

Hearn D. R., Richardson J. A., Clark G. W., 1976, ApJ, 201, L23

Hellier C., 1991, MNRAS, 251, 693

Hellier C., 1992a, MNRAS, 258, 578

Hellier C., 1992b, in Vogt N., ed., Proc. Viña del Mar Workshop on Cataclysmic Variable Stars. Astron. Soc. Pacif., San Francisco, p. 246

Hellier C., Cropper M. S., Mason K. O., 1991, MNRAS, 248, 233

Hellier C., Mason K. O., 1989, MNRAS, 239, 715

Hellier C., Mason K. O., Cropper M. S., 1989, MNRAS, 237, 39P

Hellier C., Mason K. O., Cropper M., 1990, MNRAS, 242, 250

Hellier C., Mason K. O., Mittaz J. P. D., 1991, MNRAS, 248, 5P

Hellier C., Mason K. O., Rosen S. R., Córdova F. A., 1987, MNRAS, 228, 463

Hellier C., Mason K. O., Smale A. P., Corbet R. H. D., O'Donoghue D., Barrett P. E., Warner B., 1989, MNRAS, 238, 1107

Hellier C., Sproats L. N., 1992, Inf. Bull. Var. Stars No. 3724

Herbst W., Hesser J. E., Ostriker J. P., 1974, ApJ, 193, 679

Horne K., 1986, PASP, 98, 609

Hutchings J. B., Cote J., 1986, PASP, 98, 104

Ishida M., Sakao T., Makishima K., Ohashi T., Watson M. G., Norton A. J., Kawada M., Koyama K., 1992, MNRAS, 254, 647 (I92)

Jablonski F., Busko I. C., 1985, MNRAS, 214, 219

Jablonski F., Steiner J. E., 1987, ApJ, 323, 672

Jaschek C., Jaschek M., 1990, The Classification of Stars. Cambridge Univ. Press, Cambridge

Joy A. H., 1954, ApJ, 120, 377

Kaluzny J., Semeniuk I., 1988, Inf. Bull. Var. Stars No. 3145

Kamata Y., Tawara Y., Koyama K., 1991, ApJ, 379, L65

Kemp J. C., Swedlund J. B., Wolstencroft R. D., 1974, ApJ, 193, L15

Kim S.-W., Wheeler J. C., Mineshige S., 1992, ApJ, 348, 269 (KWM)

King A. R., Frank J., Ritter H., 1985, MNRAS, 213, 181

King A. R., Lasota J.-P., 1990, ApJ, 247, 214

King A. R., Lasota J.-P., 1991, ApJ, 378, 674

King A. R., Mouchet M., Lasota J.-P., 1991, in Bertout C., Collin-Souffrin S., Lasota J.-P., Tran Thanh Van J., eds, IAU Colloq. 129, Structure and Emission Properties of Accretion Discs. Editions Frontières, Gif-sur-Yvette, p. 213

King A. R., Ricketts M. J., Warwick R. S., 1979, MNRAS, 187, 77P

King A. R., Shaviv G., 1984, MNRAS, 211, 883 (KS)

Kraft R. P., 1963, Adv. Astron. Astrophys., 2, 43

Kraft R. P., 1964, ApJ, 139, 457

Krzemiński W., 1977, in Kippenhahn R., Rahe J., Strohmeier W., eds, IAU Colloq. 42, The Interaction of Variable Stars with their Environment. Remeis-Sternwarte, Bamberg, p. 238

Krzemiński W., Serkowski K., 1977, ApJ, 216, L45

Kubiak M., Krzemiński W., 1989, PASP, 101, 669

Kuiper G., 1941, ApJ, 93, 133

Kurutz R. L., 1979, ApJS, 40, 1

Lamb D. Q., 1974, ApJ, 192, L129

Lamb D. Q., Melia F., 1987, Ap&SS, 131, 511

Lamb D. Q., Patterson J., 1983, in Livio E., Shaviv G., eds, IAU Colloq. 72,

Cataclysmic Variables and Related Objects. Reidel, Dordrecht, p. 229

Lin D. N. C., Williams R. E., Stover R. J., 1988, ApJ, 327, 234

Livio M., 1993, preprint

Lubow S. H., 1989, ApJ, 340, 1064

Mason K. O., 1989, in Hunt J., Battrick B., eds, Proc. 23rd ESLAB Symp. on Two Topics in X-ray Astronomy. ESA Publications Division, Noordwijk, p. 113

Mason K. O., Córdova F. A., Watson M. G., King A. R., 1988, MNRAS, 232, 779

Mason K. O., Watson M. G., Ponman T. J., Charles P. A., Duck S. R., Hassall B. J. M., Howell S. B., Ishida M., Jones D. H. P., Mittaz J. P. D., 1992, MNRAS, 258, 749

Mateo M., Szkody P., Garnavich P., 1991, ApJ, 370, 370

McHardy I. M., Pye J. P., Fairall A. P., Warner B., Allen S., Cropper M., Ward M. J., 1982, IAU Circ. 3687

McHardy I. M., Pye J. P., Fairall A. P., Warner B., Cropper M., Allen S., 1984, MNRAS, 210, 663

McHardy I. M., Pye J. P., Fairall A. P., Menzies J. W., 1987, MNRAS, 225, 355

Motch C., 1981, A&AS, 100, 277

Motch C., Pakull M. W., 1981, A&AS, 101, L9

Motz, L., 1952, ApJ, 115, 562

Mukai K., Corbet R. H. D., 1991, ApJ, 378, 701

Nauenberg M., 1972, ApJ, 175, 417

Norton A. J., 1993, MNRAS, preprint No. OU-PD-93-04

Norton A. J., McHardy I. M., Lehto H. J., Watson M. G., 1992b, MNRAS, 258, 697 (NMLW)

Norton A. J., Watson M. G., 1989, MNRAS, 237, 853

Norton A. J., Watson M. G., King A. R., 1988, MNRAS, 231, 783

Norton A. J., Watson M. G., King A. R., Lehto H. J., McHardy I. M., 1992a, MNRAS, 254, 705

Osborne J. P., 1988, Mem. Soc. Astron. Ital., 59, 117

Osborne J. P., 1990, in Mauche C. W., ed., Accretion-Powered Compact Binaries. Cambridge Univ. Press, Cambridge, p. 215

Osborne J. P., Mukai K., 1989, MNRAS, 238, 1233

Osborne J. P., Rosen R., Mason K. O., Beuermann K., 1985, Space Sci. Rev., 40, 143

Paczynski B., 1965, Acta Astr., 15, 197

Paczynski B., 1971, ARA&A, 9, 183

Parmar A. N., White N. E., Giommi P., Gottwald M., 1986, ApJ, 308, 199

Patterson J., 1978, IAU Circ. 3283

Patterson J., 1979a, ApJ, 233, L13

Patterson J., 1979b, ApJ, 234, 978

Patterson J., 1984, ApJS, 54, 443

Patterson J., 1990, in Mauche C. W., ed., Accretion-Powered Compact Binaries. Cambridge Univ. Press, Cambridge, p. 203

Patterson J., Branch D., Chincarini G., Robinson E., 1980, ApJ, 240, L133

Patterson J., Garcia M., 1980, IAU Circ. 3514

Patterson J., Halpern J. P., 1990, ApJ, 361, 173

Patterson J., Price C. M., 1981, ApJ, 243, L83

Patterson J., Robinson E. L., Nather R. E., 1978, ApJ, 224, 570

Patterson J., Schwartz D. A., Pye J. P., Blair W. P., Williams G. A., Caillault J.-P., 1992, ApJ, 392, 233

Patterson J., Steiner J. E., 1983, ApJ, 264, L61

Patterson J., Thomas G., 1993, PASP, 105, 50

Penning W. R., 1985, ApJ, 289, 300

Penning W. R., Schmidt G. D., Liebert J., 1986, ApJ, 301, 881

Pietsch W., Pakull M., Tjemkes S., Voges W., Kendziorra E., van Paradijs J., 1984, in Oda M., Giacconi R., eds, X-ray Astronomy '84: International Symposium on X-ray Astronomy, Balogna, Italy. Institute of Space and Astronautical Science, p. 67

Pietsch W., Voges W., Kendziorra E., Pakull M., 1987, Ap&SS, 130, 281

Press W. H., Flannery B. P., Teukolsky S. A., Vetterling W. T., 1989, Numerical Recipies: The Art of Scientific Computing (FORTRAN Edition). Cambridge Univ. Press, Cambridge

Priedhorsky W. C., 1977, ApJ, 212, L117

Pringle J. E., Rees M. J., 1972, A&A, 21, 1

Rappaport S., Verbunt F., Joss P. C., 1983, ApJ, 275, 713

Ritter H., 1990, A&AS, 85, 1179

Robinson E. L., Nather R. E., 1983, ApJ, 273, 255

Rosen S. R., 1992, MNRAS, 254, 493

Rosen S. R., Mason K. O., Córdova F. A., 1988, MNRAS, 231, 549 (RMC)

Rosen S. R., Mason K. O., Mukai K., Williams O. R., 1991, MNRAS, 249, 417

Rosen S. R., Mittaz J. P. D., Hakala P. J., 1993, MNRAS, 264, 171

Sabbadin F., Bianchini A., 1983, A&AS, 54, 393

Sambruna R. M., Chiappetti L., Treves A., Bonnet-Bidaud J. M., Bouchet P., Maraschi L., Motch C., Mouchet M., van Amerongen S., 1992, ApJ, 391, 750

Schrijver A. C., Brinkman A. C., van der Woerd H., 1987, Ap&SS, 130, 261

Schrijver A. C., Brinkman A. C., van der Woerd H., Watson M. G., King A. R., van Paradijs J., van der Klis M., 1985, Space Sci. Rev., 40, 121

Schwartz D. A., Bradt H., Briel U., Doxsey R. E., Fabbiano G., Griffiths R. E., Johnston M. D., Margon B., 1979, AJ, 84, 1560

Sekiguchi K., 1992, Nat, 358, 563

Shafter A. W., Macry J. D., 1987, MNRAS, 228, 193

Shafter A. W., Robinson E. L., Crampton D., Warner B., Prestage R. M., 1990, in Mauche C. W., ed., Accretion-Powered Compact Binaries. Cambridge Univ. Press, Cambridge, p. 237

Shafter A. W., Szkody P., Thorstensen J. R., 1986, ApJ, 308, 765

Siegel N., Reinsch K., Beuermann K., van der Woerd H., Wolff E., 1989, A&A, 225, 97

Singh J., Agrawal P. C., Apparao K. M. V., Vivekananda Rao P., Sarma M. B. K., 1991, ApJ, 380, 208 (S91)

Smale A. P., Mason K. O., White N. E., Gottwald M., 1988, MNRAS, 237, 647

Steiner J. E., Schwartz D. A., Jablonski F. J., Busko I. C., Watson M. G., Pye J. P., McHardy I. M., 1981, ApJ, 249, L21

Stockman H. S., Schmidt G. D., Angel J. R. P., Liebert J., Tapia S., Beaver E. A., 1977, ApJ, 217, 815

Swedlund J. B., Kemp J. C., Wolstencroft R. D., 1974, ApJ, 193, L11

Szkody P., Brownlee D. E., 1977, ApJ, 212, L113

Tapia S., 1977, ApJ, 212, L125

Thorstensen J. R., Ringwald F. A., Wade R. A., Schmidt G. D., Norsworthy J. E., 1991, AJ, 102, 272

Tuohy I. R., Remillard R. A., Brissenden R. J. V., Bradt H. V., 1990, ApJ, 359, 204

van Amerongen S., Augusteijn T., van Paradijs J., 1987, MNRAS, 228, 377

van der Woerd H., de Kool M., van Paradijs J., 1984, A&A, 131, 137

Walker M. E., 1954, PASP, 66, 230

Walker M. E., 1956, ApJ, 123, 68

Walker M. E., 1958, ApJ, 127, 319

Wang Y.-M., 1987, A&A, 183, 257 (W87)

Warner B., 1983, in Livio E., Shaviv G., eds, IAU Colloq. 72, Cataclysmic Variables and Related Objects. Reidel, Dordrecht, p. 155

Warner B., 1985, in Lamb D. Q., Patterson J., eds, Cataclysmic Variables and Low-Mass X-ray Binaries. Reidel, Dordrecht, p. 269

Warner B., 1986, MNRAS, 219, 347

Warner B., 1988, Nat, 336, 129

Warner B., O'Donoghue D., Fairall A. P., 1981, MNRAS, 196, 705

Watson M. G., 1986, in Mason K. O., Watson M. G., White N. E., eds, The Physics of Accretion onto Compact Objects. Springer-Verlag, Berlin, p. 97

Watson M. G., King A. R., Osborne J., 1985, MNRAS, 212, 917

Watts D. J., Greenhill J. G., Hill P. W., Thomas R. M., 1982, MNRAS, 200, 1039

West S. C., Berriman G., Schmidt G. D., 1987, ApJ, 322, L35

White N. E., Peacock A., 1988, Mem. Soc. Astron. Ital., 59, 7

White N. E., Marshall F. E., 1980, IAU Circ. 3514

White N. E., Marshall F. E., 1981, ApJ, 249, L25

Williams R. E., 1980, ApJ, 235, 939

Williams R. E., 1989, AJ, 97, 1752

Wu C.-C., Panek R. J., Holm A. V., Raymond J. C., Hartmann L. W., Swank J. H., 1989, ApJ, 339, 443

Wynn G. A., King A. R., 1992, MNRAS, 255, 83

Zhang E., Robinson E. L., Ramseyer T. F., Shetrone M. D., Stiening R. F., 1991, ApJ, 381, 534

PUBLICATIONS

Publications arising form the work in this thesis:

Hellier C., Garlick M. A., Mason K. O., 1993, MNRAS, 260, 299. 'X-ray orbital modulations in intermediate polars'. (From chapter 2).

Garlick M. A., Rosen S. R. R., Mittaz J. P. D., Mason K. O., De Martino D., 1994, MNRAS, in press. 'Spin-resolved optical CCD spectroscopy and photometry of BG Canis Minoris'. (From chapters 3 and 4).

Garlick M. A., Mittaz J. P. D., Rosen S. R. R., Mason K. O., 1994, MNRAS, submitted. 'Spin-resolved optical CCD spectroscopy of GK Persei'. (From chapter 5).

Other:

Wickramasinghe D. T., Cropper M., Mason K. O., Garlick M., 1991, MNRAS, 250, 692. 'Cyclotron humps in AM Her systems – IV. Variations around the orbit in MR Ser'.

ADDENDUM 1

1. On page 33, line 8 of §1.5.3, after 'strengths', add: 'It was realised that if polars and intermediate polars did indeed possess white dwarfs with comparable field strengths, then the possibility existed that the two systems represent the same object seen from different evolutionary vantage points. This notion is strenghthened by the observation that most polars have orbital periods less than two hours, whilst the intermediate polars generally have orbital periods greater than three hours. The systems therefore bracket the so-called 'period-gap', and it was suggested that perhaps the intermediate polars evolve through this gap to become polars (see, e.g., King, Frank & Ritter 1985. Lamb & Melia 1987, and Hameury et al. 1988). If so, the implication may be that intermediate polars, like polars, do not possess accretion discs.'

2. Figure 1.2 (page 37) is misleading because it appears that the near and far sides of the disc are illuminated simultaneously. Clearly this is not the case. At the orientation of the white dwarf as shown in the diagram, the far side of the disc, which has a greater visible surface area, is illuminated. Maximum optical radiation is therefore seen reprocessed from the disc in this situation. However, when the white dwarf has rotated half a cycle, the nearest part of the disc (smaller visible surface area) is illuminated, and a minimum intensity is seen.

ACKNOWLEDGEMENTS

I am indebted to many, many people for their injections of much-needed help, encouragement and humour during this Ph.D., and for the fact that I still appear to be sane after these four very short years... so my friend Colin the Space-Gerbil tells me. This work has been the most challenging aspect of my life so far, and one which I shall not forget in haste. Well, not unless I am offered some serious money[1].

I wish to thank Prof. Len Culhane (the director of MSSL), Dr. Keith Mason (my supervisor), and Dr. Graziella Branduardi-Raymont, all of whom allowed me this opportunity to study astrophysics at the lab, and Dr. Coel Hellier, for introducing me to South Africa. I am eternally grateful to my other colleagues at the lab, Drs. Jonathan Mittaz, Dave Wonnacott, and Francisco Carrera, for their humanity, without which I would surely have continued on a geodesic leading only to doom, gloom, despair, and no cigar (well, thesis). I express particular gratitude to Jon and Dave for their help on matters of astrophysics, data analysis, proof-reading, and alcohol. Many others are to be thanked for similar reasons (but not the alcohol): Drs. Thomas Augusteijn, Domitilla De Martino, Martine Mouchet, Koji Mukai, Andy Norton, Simon Rosen, and staff at La Palma and at the South African Astronomical Observatory.

A mega-thank-you goes to all my friends and fellow non-persons. The list is long, but witholding the names of the individuals concerned would be the most heinous crime since E.T. phoned home without paying for it. So here it is:

Caz Allen, for being living, breathing proof that I am not the only person this side of the Antares Maelstrom whose speech is so rapid that it suffers a Lorentz

[1]Speaking of which, thank you, SERC.

contraction. Vito Graffagnino, for teaching me that blinding handshake, and for demonstrating that I am not the only student for whom the words 'dress' and 'sense'—in that order—have a meaning. Chris Jomaron, for co-authoring 'The Story', and for having a sense of humour so similar to mine that I am not entirely sure whether it is him or myself writing this at the moment. Gav Ramsay, for the CDs, and for being the only student I could find who was prepared to read various decrepit drafts of my chapters, even though he found it akin to 'wading through mud'. Phil 'PJS1-Unit' Smith, for proving that it is always possible to remain in the same emotional state and refrain from the use of profanity, even under situations of utter stress, and even when surrounded by people for whom that way of 'communicating' is second-nature (no names mentioned, Lee). Lee 'Hammer' Sproats, for having an accent that makes mine sound like a 40s BBC-radio World-Service announcer who has just gargled with lavender-water. Chas Wiles, for listening, for the E-mails, for the dinner parties, and for proving that, yes, I *can* determine whether or not I will find a particular food palatable merely by peering at it—a subject which was until recently one of serious debate. And for their friendship, humour and liveliness, I take my panama off to Julie Cave, Ian Davenport, Alisdair Davey, Mick Edgar, Nick Flowers, Tom and Sheila Foster, Adrian James, 'Mad' Matt Kenworthy, Mike Lancaster, Sri Moorthy, Andy and Simon Phillips, Dolores Rawlings, Sarah Szita, Roger 'Splodge' Woodliffe, the nice ladies in the office, and a partridge in a pear tree.

I also thank my family for their faith in me. And thanks, mum, for not insisting that I visit you *every* weekend—even though nothing would have pleased you more.

Finally, I express my deepest gratitude to two very special people: to my newest and closest friend, Margaret Kate Harrop-Allin, without whose 'companionship' I'd have sunk lower and faster than an osmium anvil in quicksand; and to her husband, Peter Henning, for his understanding, for his tolerance, and for not venturing to discover, after all, what the underside of a moving train looks like.

Thanks, people. I wouldn't have missed it for all the tea in... Tesco's.

Science has 'explained' nothing; the more we know the more fantastic the world becomes and the profounder the surrounding darkness.

Aldous Huxley
Views of Holland (1964)